Isothermal and Homogeneous Detection of Nucleic Acids and Proteins Using the

Cleavage Activities of CRISPR-Cas and DNAzyme

by

Yiren Cao

A thesis submitted in partial fulfillment of the requirements for the degree of

Doctor of Philosophy

in

Analytical and Environmental Toxicology

Department of Laboratory Medicine and Pathology

University of Alberta

Abstract

Nucleic acids and proteins play essential roles in biological systems; and the detection of these molecules can be applied to the diagnoses of diseases. Extensive detection of the severe acute respiratory syndrome coronavirus-2 (SARS-CoV-2) viral RNA has contributed to the containment of the recent coronavirus disease of 2019 (COVID-19) pandemic. The gold standards for the detection of nucleic acids and proteins are the polymerase chain reaction (PCR) and enzyme-linked immunosorbent assay (ELISA), respectively. Although PCR and ELISA are sensitive and accurate, they are not ideal for point-of-care (POC) analysis because PCR requires thermal cycling and ELISA protocols include time-consuming washing steps. Isothermal amplification techniques and homogeneous binding assays are promising alternatives for POC applications. The former can be performed under readily achievable temperature and the latter in a single test tube.

Recently, clustered regularly interspaced short palindromic repeats (CRISPR) and CRISPR-associated (Cas) proteins have been integrated with the isothermal amplification techniques to improve the specificity of the detection of SARS-CoV-2 viral RNA to avoid false positive results. Composed of a guide RNA (gRNA) and a Cas protein, the CRISPR-Cas system can be activated only when the gRNA hybridizes with the specific amplification product of target gene. Most developed assays for SARS-CoV-2 rely on fluorescence detection and/or a lateral flow format, which requires an excitation light source and sophisticated equipment. Colorimetric assays, on the other hand, have not been

fully exploited for sensitive and rapid detection. Described in Chapter 2, a molecular transducer with hairpin structure was used to facilitate the *trans*-cleavage activity of CRISPR-Cas12a, resulting in the aggregation of gold nanoparticles (AuNPs) and color change. A simple centrifugation step for 10 seconds was sufficient to achieve a clear color change within 1 minute. The assay maintained the sensitivity of isothermal amplification and had a detection limit of 225 copies of the nucleocapsid (N) gene of the viral RNA.

The cleavage activity of DNAzyme has also been incorporated with isothermal amplification techniques to construct DNA circuits with enhanced sensitivity or lower background. In a typical circuit, the amplification reaction and cleavage reaction form a positive feedback loop to amplify the target exponentially. However, the detection of different nucleic acid targets requires individually redesigned sequences of the circuit. Taking advantage of the multiple component nucleic acid enzyme (MNAzyme) technique derived from DNAzyme, I designed two subunits to recognize the target and initiate the DNA circuit (Chapter 3). The detection of a different target was readily achieved by changing only the complementary region of the subunits. To minimize background and maintain the cleavage activity of the MNAzyme, I investigated a series of blockers that were critical to the construction of circuit with positive feedback. I achieved a limit of detection at fM levels for two model targets.

MNAzymes have been used for the detection not only of nucleic acids but also of proteins. MNAzymes with different secondary structures have been reported and the split

locations of MNAzymes used for proteins were the same as of MNAzymes used for nucleic acids. So far, there is no systematic study exploring how the secondary structure and split location affect the cleavage activity of MNAzymes in protein analysis. In Chapter 4, I systematically compared 14 split locations and two secondary structures to obtain MNAzymes with high cleavage activity. To achieve homogeneous detection of specific proteins, I combined the selected MNAzyme with binding-induced DNA assembly (BINDA) (Chapter 5). I designed two DNA motifs with short complementary regions. The two motifs assembled together to form the MNAzyme only in the presence of the protein target. For the detection of two protein targets, I achieved a sensitivity of pM level without polymerase-assisted amplification. The assay was performed in a single test tube and required only the mixing of reagents and reading of signals.

I developed a colorimetric assay and a DNA circuit for isothermal detection of nucleic acid targets. I investigated the MNAzyme with the optimal split location and secondary structure for homogeneous detection of protein targets. My thesis research contributes to the development of POC tests of these biomolecules. By altering the recognition component (gRNA, sensor arm, aptamer, and antibody), I can potentially extend the developed assays to the detection of various targets.

Preface

This thesis is an original work by Yiren Cao. A portion of Chapter 1 has been published as Feng, W., Newbigging, A.M., Tao, J., **Cao, Y.**, Peng, H., Le, C., Wu, J., Pang, B., Li, J., Tyrrell, D. L., Zhang, H., and Le, X. C. (2021), 4683-4698. CRISPR technology incorporating amplification strategies: Molecular assays for nucleic acids, proteins, and small molecules. *Chemical Science*. (DOI: 10.1039/D0SC06973F). Feng, W., Newbigging, A.M., Tao, J., Cao, Y., Peng, H., and Le, C. contributed to data curation, formal analysis, visualization, validation, writing original draft, and writing review and editing. Wu, J. and Pang, B. contributed to data curation, formal analysis, and writing a component of the original draft, review and editing. Li, J. and Tyrrell, D. L. contributed to funding acquisition, resources, supervision, and writing review and editing. Zhang, H. and Le, X. C. contributed to conceptualization, data curation, formal analysis, funding acquisition, project administration, resources, supervision, writing original draft, and writing review and editing.

The contents of Chapter 2 have been published as **Cao, Y.**, Wu, J., Pang, B., Zhang, H., and Le, X. C. (2021), 6871-6874. CRISPR/Cas12a-mediated gold nanoparticle aggregation for colorimetric detection of SARS-CoV-2. *Chemical Communications*. (DOI: 10.1039/D1CC02546E). Cao, Y., Wu, J., and Pang, B. contributed to conceptualization, investigation, data curation, formal analysis, visualization, validation, writing, review, and editing. Zhang, H. and Le, X. C. contributed to conceptualization, formal analysis,

Acknowledgements

I would like to thank my supervisor, Dr. X. Chris Le, for his support throughout my Ph.D. program. He has taught me how to present my research project to people in other research areas. He has also trained me to master the skills not only of research study, but also of writing a proposal, reviewing a manuscript, outlining a review paper, and collaborating with other members in a research team. I cannot become a well-round researcher without his guidance.

I would like to thank Dr. X. Chris Le and Dr. Xing-Fang Li for their support during my daily life and social events they organized. Division of analytical and environmental toxicology is another family for me. Thank you for the green vegetables and moon cakes you shared with us.

I would like to thank Dr. Hongquan Zhang for his guidance throughout my program, from developing the new projects to data interpretation. He has also trained me to fully understand the mechanisms of the proposed projects and how to troubleshoot the problems when I could not explain my experimental results.

I appreciate the help from Katerina Carastathis. Without your support to save me time, I could not focus on my Ph.D. program. I also would like to thank you for helping me revise my manuscripts and thesis.

I would like to thank my supervisory committee member, Dr. Robert Ingham, for his support. You provided me with thoughts from another aspect. I appreciate the suggestions and advice from you in my committee meetings.

I also want to thank all the students and postdoctoral fellows in the AET Division. It was a nice time to discuss our research work and enjoy our social events. You are my best colleagues and friends.

Finally, I would like thank my parents for their support and love. I didn't realize how much you have done for me until I came here and lived independently. During the hard times of the pandemic, your weekly phone calls and long talks encouraged me to move forward. I couldn't have done it without you.

Table of Contents

List of Figures

List of Tables

List of Abbreviations

Abbreviation	Full Name
AuNP	gold nanoparticle
BINDA	binding-induced DNA assembly
BSA	bovine serum albumin
Cas	CRISPR-associated
CHA	catalytic hairpin assembly
COVID-19	coronavirus disease of 2019
CRISPR	clustered regularly interspaced short palindromic repeats
crRNA	CRISPR RNA
DETECTR	DNA Endonuclease-Targeted CRISPR Trans Reporter
DNA	deoxyribonucleic acid
dNTP	nucleoside triphosphate
dsDNA	double-stranded DNA
ELISA	enzyme-linked immunosorbent assay
E-SDA	exponential strand displacement amplification
EXPAR	exponential amplification reaction
FIP	forward inner primer
gRNA	guide RNA
HT	hairpin transducer

$k_{obs,m}$	multiple turnover number
$k_{obs,s}$	single turnover number
LAMP	loop-mediated isothermal amplification
MBS	molecular beacon substrate
MNAzyme	multiple-component nucleic acid enzyme
Nt	Nucleotide
PAM	protospacer adjacent motif
PCR	polymerase chain reaction
PDGF-BB	platelet-derived growth factor B-chain
PLA	proximity ligation assay
POC	point-of-care
PSA	prostate-specific antigen
RCA	rolling circle amplification
RNA	ribonucleic acid
RPA	recombinase polymerase amplification
RNP	Ribonucleoprotein
RT	reverse transcription
SARS-CoV-2	severe acute respiratory syndrome coronavirus-2
SDA	strand displacement amplification
sgRNA	single-guide RNA

SHERLOCK	Specific High-sensitivity Enzymatic Reporter UnLOCKing
ssDNA	single-stranded DNA
UV-Vis	ultraviolet–visible

Chapter 1 Introduction

1.1 Nucleic acids and proteins

Nucleic acids are polymers of nucleotides, whose complementary nature ensures the transfer of genetic information described by central dogma. Proteins consist of amino acid residues (polypeptides). The non-covalent bonds and disulfide bridges between residues fold the polypeptide chain into a specific three-dimensional conformation, which determines the activity of protein. The functions of proteins include but are not limited to catalyzing reactions, cell signaling, immune response, mechanical support and transporting other molecules.[1-2]

1.1.1 Need for detection of nucleic acids and proteins

Since nucleic acids and proteins play critical roles in biological systems, mutated DNAs (or RNAs), secreted proteins, and changes in concentrations of these molecules usually indicates the existence and development of diseases.[3] For instance, microRNAs and prostate-specific antigen (PSA) can be used as biomarkers for cancers.[4-13] The detection and monitoring of them contribute to the early diagnosis and treatment of diseases.[14] Therefore, Great efforts have been devoted to the development of simple detection methods for point-of-care (POC) analysis.[3, 15]

Recently, coronavirus disease of 2019 (COVID-19) has raised the need for specific and sensitive detection of nucleic acid and protein. As of April 2021, this global pandemic

has led to more than 140 million reported cases and 3 million deaths. The molecular diagnosis of COVID-19 depends mainly on the detection of different genes of the severe acute respiratory syndrome coronavirus-2 (SARS-CoV-2) viral RNA.[16-17] The detection of immunoglobulin G and M (IgG and IgM) antibody in human serum is also useful for confirming past infection.[18]

1.1.2 Conventional detection methods for nucleic acids and proteins

Polymerase chain reaction (PCR) and enzyme-linked immunosorbent assay (ELISA) are the most popular detection methods for nucleic acids and proteins, respectively.[19-22] Their developments are the milestones of the molecular diagnosis. The capability of PCR for exponential amplification has realized the detection of a few copies of a nucleic acid target. ELISA uses protein enzymes instead of radioactivity as the reporter to replace radioimmunoassays.[21] ELISA has a simple procedure and simultaneous analysis can be achieved without complicated pre-treatment of samples.[23] ELISA can detect levels as low as 100 pg/mL of proteins with good specificity.[24]

As demonstrated in Figure 1.1, PCR amplification of DNA relies on the thermal cycling.[20] Each cycle has three stages: denaturation, annealing, and elongation. A high temperature of 95 °C is used in the denaturation stage to melt the double-stranded DNA (dsDNA). Then, the temperature drops to about 50 °C to anneal the primers with the denatured single-stranded DNA (ssDNA). The temperature of the elongation stage is set at about 72 °C for the optimal activity of the DNA polymerase. The polymerase can extend

the 3'-end of the primer by adding nucleotides complementary to the ssDNA one by one. In each cycle, the amount of the DNA target is doubled.

During the COVID-19 pandemic, reverse transcription (RT)-PCR has been used to detect specific sequences of the viral RNA genome.[25-27] Reverse transcription of the target produces a complementary DNA that can be amplified by the procedure of the thermal cycling. During the amplification, the polymerase with 5'-3' exonuclease activity can break down the fluorescent probes (e.g., TaqMan probes) hybridizing with the amplicons. Thus, the fluorophore and quencher on the two ends of the probe is separated to generate fluorescence signal.

Figure 1.2 illustrates a typical ELISA assay with sandwich format.[23] It comprises five steps: (i) immobilization of capture antibody, (ii) sample incubation, (iii) separation of unbound target, (iv) incubation of enzyme-labeled antibody, and (v) signal generation. After the capture antibodies are immobilized on the plate, multiple washing steps have to be used to remove extra antibodies. Then, the buffer containing BSA (bovine serum albumin) is used for blocking the plate to prevent the non-specific adsorption of enzyme-labeled antibodies and interference proteins in sample matrix. Next, the sample is added to capture the target. The unbound target is also removed by multiple washing steps. The enzyme-labeled antibodies are added to bind to captured targets and form a sandwich structure for signal generation. It is also necessary to wash away extra enzyme-labeled antibodies. As the sandwich ELISA employs two antibodies to recognize one target, it has an excellent specificity for protein detection.
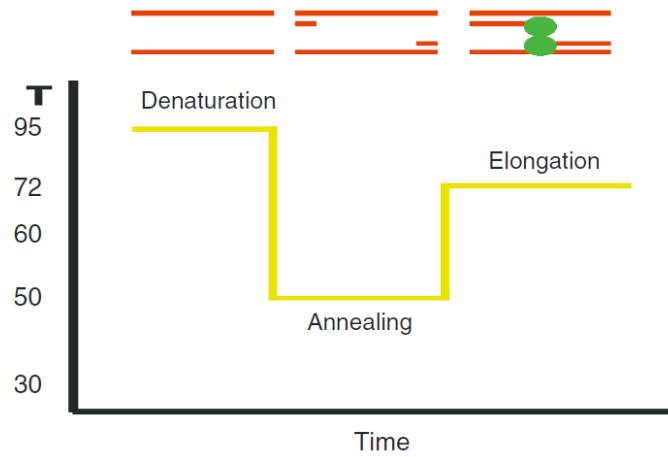
Figure 1.1. Thermal cycling of PCR. The temperature is raised to 95 °C for the denaturation of the dsDNA target. Then, the temperature is decreased to about 50 °C for primer annealing. The polymerase extends the primers at 72 °C. Reprinted with permission.[20] Copyright 2006 Elsevier.
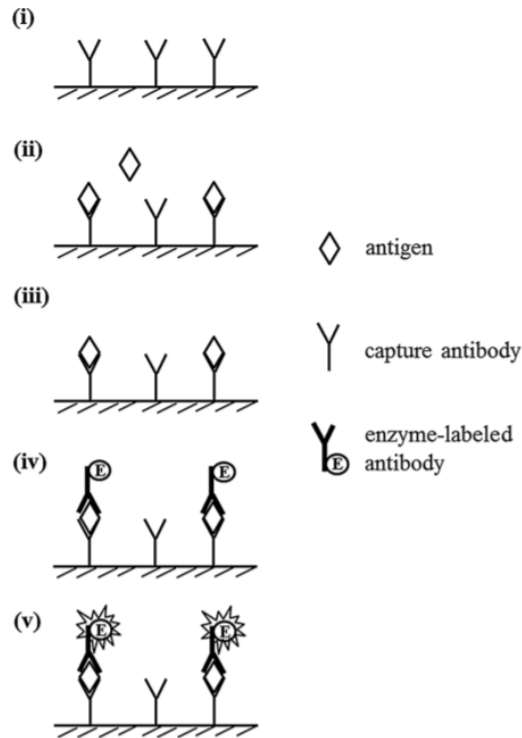
Figure 1.2. Detection of antigen using sandwich ELISA.[23] The procedure includes: (i) immobilization of capture antibody on the solid phase of the plate; (ii) incubation of target antigen; (iii) washing the plate to remove the unbound target; (iv) incubation of enzyme-labeled antibody; (v) signal generation using substrate. Reprinted with permission. Copyright 2018 Springer.

Although PCR and ELISA are the gold standards, they need a thermal cycler or multiple washing steps that are not ideal for simple POC analysis. Isothermal amplification techniques and homogeneous binding assays are promising alternatives for the detection of nucleic acids and proteins, respectively.

1.2 Isothermal amplification of nucleic acids

Despite the extraordinary sensitivity of PCR, the high energy consumption of the thermal cycler limits its application in resource-limited settings and POC analysis.[28] The isothermal amplification technique is a promising alternative to PCR because the amplification is performed at a mild and constant temperature. Only an air or water bath at 37–65 °C is required to conduct the amplification. Instead of using high temperature (95 °C), isothermal amplification techniques can unwind the double-stranded target by using different enzymes, such as ribonuclease H, helicase, recombinase, and polymerase with strand displacement activity.[28]

The first isothermal amplification technique for nucleic acids was established based on ribonuclease H. Known as self-sustained sequence replication, this technique was performed at 37 °C.[29] The RNA template is first reverse transcribed to produce a DNA/RNA hybrid. After ribonuclease H degrades the RNA template in the hybrid, complementary DNA is then released for the next round of amplification. In the helicase-dependent amplification[30] and recombinase polymerase amplification (RPA)[31] techniques, helicase can open the DNA duplex and recombinase can facilitate the strand exchange for primer binding.

The most prominent strategy uses DNA polymerases with intrinsic strand displacement activity. Strand displacement amplification (SDA)[32] and exponential amplification reaction (EXPAR)[33] are two techniques that need both DNA polymerase and

restriction endonuclease. After the polymerase makes a copy of the template, the endonuclease can recognize a specific region of the copy and nick it to generate a new 3'-end. Then, the polymerase extends this new end to produce a second copy, which is nicked and extended repeatedly. On the other hand, rolling circle amplification (RCA)[34-35] and loop-mediated isothermal amplification (LAMP)[36] only need polymerase, but no endonuclease. RCA uses a circular template formed by the ligation of the padlock probe. The polymerase can keep extending the primer and displace the product on the circular template with no need for new 3'-end. The amplified product of LAMP can form new 3'-end by self-folding into a loop-stem structure.

1.2.1 Strand displacement amplification (SDA) technique

Walker et al. developed the first SDA using DNA polymerase and endonuclease at 37 °C (Figure 1.3).[37] The primer strand contains the recognition region (5'-GTTGAC) for restriction endonuclease. Assisted by nucleoside triphosphate (dNTP), the DNA polymerase can extend the 3'-ends of the primers and the target. The extension forms the DNA duplex (GTTGAC/GTCAsAsC), which can be recognized by endonuclease *Hinc* II for nicking. In the recognition region, the nucleotide 'A' is displaced by 'As' (A alpha S), whose phosphate on the 5'-carbon has sulfur instead of oxygen. Consequently, the endonuclease can only nick the strand 5'-GTTGAC. Thus, polymerase can extend the new 3'-end (GTT-3') to generate a new copy of the target and meanwhile displace the old copy of the amplification.
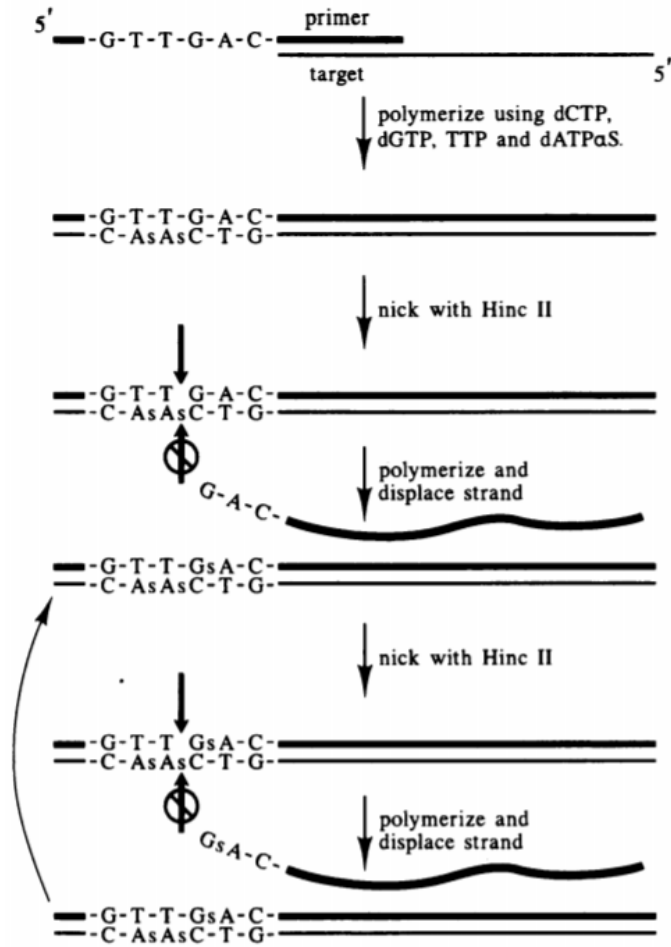
Figure 1.3. Fundamental reaction process of SDA technique.[37] DNA target binds to the SDA primer containing recognition sequence for endonuclease, *Hinc* II. Polymerase extends the primer to produces a double-stranded recognition region that *Hinc* II can nick. Then, polymerase extends the new 3'end at the nick and displace the downstream fragment. Nicking and extension/displacement steps cycle repeatedly to produce single-stranded copies of the target. Reprinted with permission. Copyright 1992 U.S. National Academy of Sciences.

The original SDA used only one primer and amplified the target in a linear manner. Using two primers to amplify dsDNA, the same research group developed the exponential SDA (E-SDA), which was able to generate 10^7 copies of the target in two hours.[32] Despite its high efficiency of amplification at a mild temperature, E-SDA still needs the initial thermal denaturation step at 95 °C to unwind the target.

1.2.2 Loop-mediated isothermal amplification (LAMP) technique

Compared to SDA, LAMP uses only polymerase but requires a higher reaction temperature of 65 °C. Figure 1.4 depicts the LAMP reaction.[38] LAMP employs at least four primers, a forward inner primer (FIP), a backward inner primer (BIP), and two outer primers (F3 and B3), to target different regions of the dsDNA (Figure 1.4.a). The F2 region of FIP first hybridizes with the F2c region of the target, making a copy containing the F1c, F2, F1, B1c, B2c and B3c regions (Figure 1.4.b). Next, the F3 primer binds to F3c of the target. The extension of F3 displaces this copy from FIP. The F1c and F1 regions self-fold to form a loop-stem structure. BIP and B3 primers then do the same process to generate a product with a dumbbell structure. Figure 1.3.c demonstrates the cycling amplification based on the dumbbell structure. The extension starts from either the 3'-end of the stem or the FIP/BIP binding to the loop region. LAMP has a powerful amplification capability of generating 10^9 copies of the target in 1 hour.

In spite of its high amplification efficiency, LAMP has the limitation of nonspecific

amplification.[39] SYBR Green is the dye that is usually used to monitor all dsDNA products of LAMP. Any nonspecific amplicon of LAMP can be also detected by SYBR Green to generate false positive results.
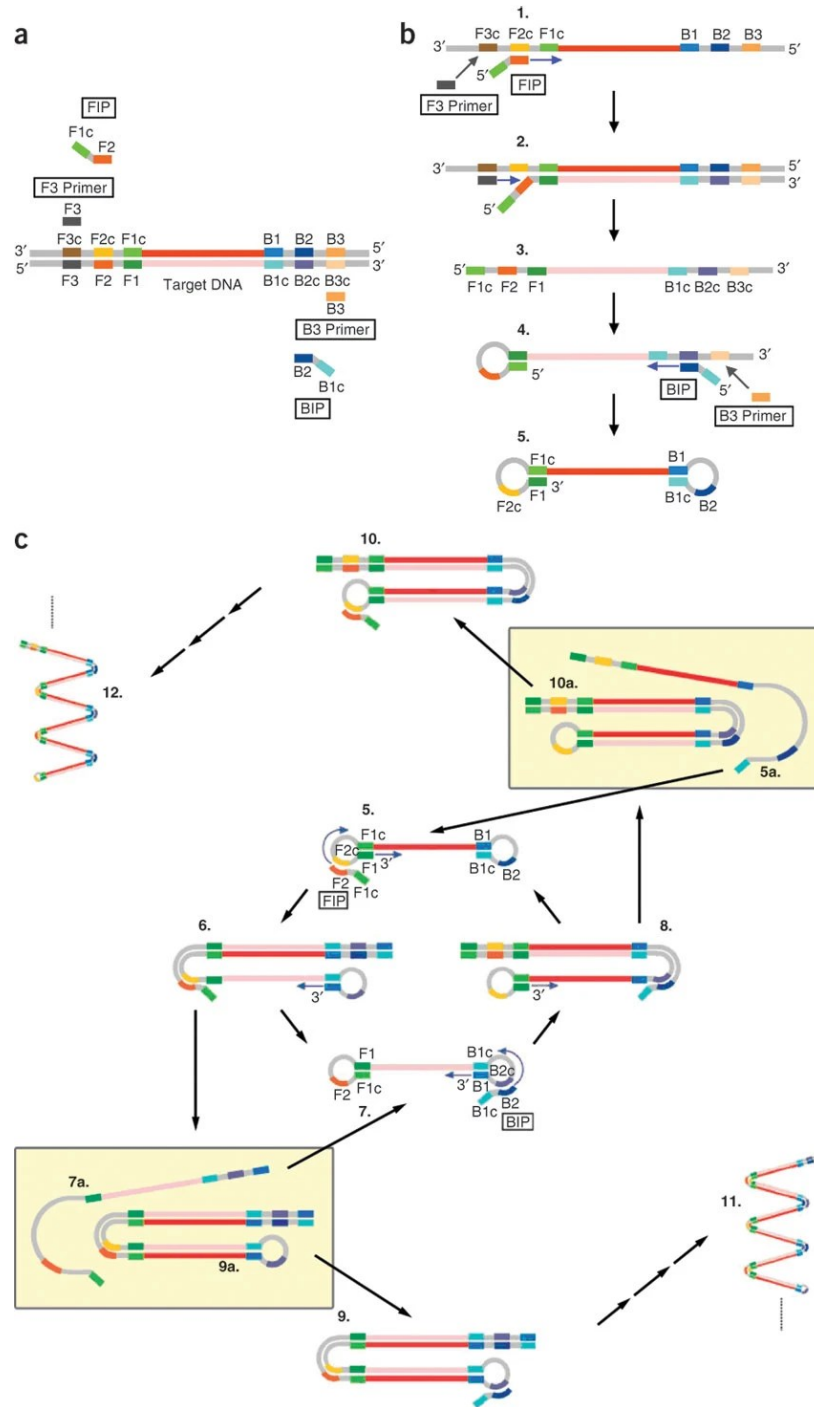
Figure 1.4. Principle of LAMP technique.[38] (a) Design of 4 primers: forward inner primer (FIP), backward inner primer (BIP), and outer primers (F3 and B3). (b) Generation of dumbbell structure. (c) Cycling amplification step. Reprinted with permission. Copyright 2008, Springer Nature.

1.3 Combining *trans*-cleavage activity of CRISPR-Cas12a system with isothermal amplification techniques

In recent years, CRISPR-Cas systems have been combined with isothermal amplification techniques for the detection of nucleic acids without interference by nonspecific amplicons.[40] The CRISPR-Cas system is composed of a CRISPR RNA (crRNA) or a single-guide RNA (sgRNA) and a Cas effector protein.[41-43] In contrast to other nucleic acid binding proteins, Cas protein can target any gene sequence by recruiting a complementary crRNA or sgRNA. The programmable property of this simple two-component system is advantageous for gene editing, regulating, and imaging. Furthermore, several Cas effector proteins have been found to possess *trans*-cleavage activity that can be utilized for nucleic acid detection.[43-45] The binding of CRISPR-Cas to the target is extremely specific and the multiple turnover *trans*-cleavage reaction can improve the sensitivity. Thus, the CRISPR-Cas technique can improve the isothermal amplification to achieve better performance of nucleic acid detection.

1.3.1 CRISPR-Cas12a system and *trans*-cleavage

Four common CRISPR-Cas systems, CRISPR-Cas9,[41] Cas12a,[43] Cas13a[44], and Cas14[45], have been characterized with different targeting properties and cleavage activities. Cas9, Cas12a, and Cas14 can target DNA but Cas13a only binds to RNA. Cas9

has only *cis*-cleavage activity to cleave its target while Cas12a, Cas13a, and Cas14 have both *cis*- and *trans*-cleavage activity. Cas12a and Cas14 can *trans*-cleave nonspecific ssDNA but Cas13a *trans*-cleaves ssRNA. Among these four systems, Cas12a has been most widely investigated for the detection of nucleic acids when it is necessary to use isothermal amplification techniques to amplify the target prior to the *trans*-cleavage. CRISPR-Cas12a can directly recognize the specific dsDNA products of isothermal amplification and has a high activity of *trans*-cleaving 1250 substrates by one enzyme per second. Labelling the ssDNA substrate with functional groups (e.g., fluorophore and quencher pair), researchers took advantage of the *trans*-cleavage activity of Cas12a to develop different detection platforms for nucleic acids.[43, 46-48]

Figure 1.5 shows the *cis*-cleavage of the dsDNA target and *trans*-cleavage of the nonspecific ssDNA substrate by CRISPR-Cas12a.[40] The CRISPR-Cas12a system consists of a crRNA and Cas12a effector protein. The spacer region of the crRNA can guide Cas12a to match the protospacer region in the target strand. When binding to the dsDNA, crRNA needs a protospacer adjacent motif (PAM) downstream from the protospacer. Thus, Cas12a has good specificity toward the dsDNA target. The endonuclease activity of the RuvC domain of Cas12a can *cis*-cleave both the target strand and the non-target strand at staggered sites to produce a 5–7 nt overhang. Cas12a cleaves not only the target dsDNA but also any ssDNA indiscriminately. Such *trans*-cleavage occurs in a multiple turnover manner and thus can be harnessed to amplify the signal of detection of nucleic acids.
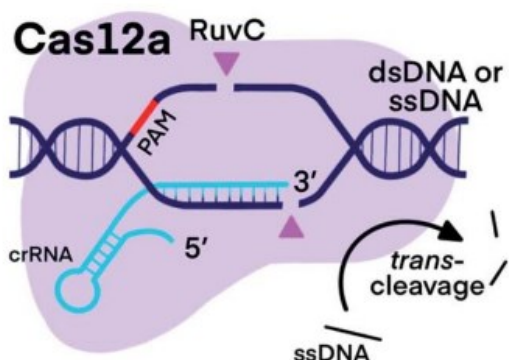
Figure 1.5. Components of CRISPR-Cas12a and its *cis-* and *trans*-cleavage. Upon binding to the dsDNA target, Cas12a can achieve the PAM-dependent cleavage of both target and non-target strands with RuvC domain alone. Cas12a also exhibits the *trans*-cleavage activity, which cleaves the ssDNA indiscriminately. Reprinted with permission.[40] Copyright 2021, Royal Society of Chemistry.

1.3.2 Incorporating the CRISPR-Cas12a system after isothermal amplification

The *trans*-cleavage activity of CRISPR-Cas12a has been incorporated after the isothermal amplification of low abundance nucleic acid targets to achieve specific and sensitive detection on versatile platforms.[43, 46] As mentioned above, Cas12a can specifically recognize the dsDNA so that it can differentiate the specific amplicon from the byproduct of the isothermal amplification. In addition, the multiple turnover cleavage activity can generate an amplified signal readout to improve the sensitivity. Moreover, the

ssDNA substrate of *trans*-cleavage can be labelled with different functional groups to be applied to fluorescent and lateral flow.

After Zhang's group developed SHERLOCK (Specific High-sensitivity Enzymatic Reporter UnLOCKing) strategy by incorporating CRISPR-Cas13 after RPA, Doudna and her coworkers used Cas12a to replace Cas13 to avoid the additional transcription step and established DETECTR (DNA Endonuclease-Targeted CRISPR Trans Reporter) strategy.[43] The DNA amplicons of RPA were directly scanned by Cas12a and only the specific amplicon activated the *trans*-cleavage activity of Cas12a. The indiscriminate cleavage of ssDNA labeled with a fluorophore and a quencher generated a fluorescence signal and a sensitivity of aM was achieved for the nucleic acid detection. DETECTR was further applied to the detection of SARS-CoV-2 viral RNA.[46] The reverse transcription (RT)-LAMP amplicon of the viral RNA can activate CRISPR-Cas12 to *trans*-cleave the ssDNA substrate. As displayed in Figure 1.6, the detection results were visualized by the lateral flow strip. In contrast to the RT-PCR that requires a thermal cycler, this assay uses heating blocks and a constant temperature for amplification. The overall reaction time was less than 40 minutes that is favorable for POC applications. Thanks to the improvement of specificity by CRISPR-Cas system, the method was reported to have a 100% agreement between the CRISPR-Cas test and RT-PCR test of SARS-CoV-2 negative samples.
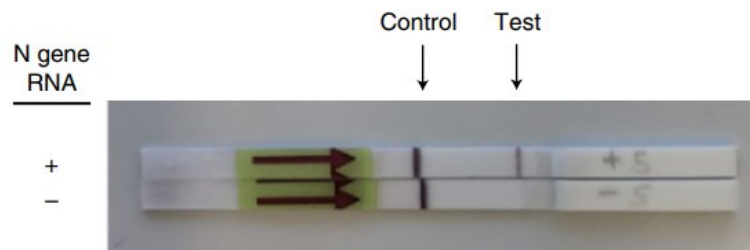
Figure 1.6. Incorporation of CRISPR-Cas12a after RT-LAMP for the detection of SARS-CoV-2.[46] The photograph above shows the minimum equipment required for the method. The photograph below demonstrates the positive and negative readout of the lateral flow test for the N gene of viral RNA. Reprinted with permission. Copyright 2020, Springer Nature.

So far, this strategy is mainly used for fluorescence detection or lateral flow analysis. The fluorescence detection requires an excitation light source and the lateral flow requires the extra equipment of lateral flow dipsticks. However, colorimetric detection that does

not need additional equipment has not been well investigated for the combination of isothermal technique and CRISPR-Cas12a.

1.4 RNA-cleaving DNAzyme for nucleic acid detection

RNA-cleaving DNAzyme is a type of functional nucleic acid that also has cleavage activity.[49] Similar to the CRISPR-Cas technique, the activation of the DNAzyme is programmable and can be applied to the detection of various nucleic acid targets using the multiple-component nucleic acid enzyme (MNAzyme) strategy.[50] This detection strategy is also specific because of the requirement of Watson-Crick base pairing of two recognition units to one target. Compared to the protein enzymes, DNAzyme has several critical advantages, such as high thermal and chemical stability, and ease of modification.[51] The *trans*-cleavage of the ssDNA substrate by CRISPR-Cas12a is indiscriminate while DNAzyme can be designed to cleave specific sites. Therefore, the DNAzyme has also been incorporated with isothermal amplification techniques for the detection of nucleic acids.[52-55]

1.4.1 RNA-cleaving DNAzyme

RNA-cleaving DNAzymes can catalyze the cleavage reaction of their RNA substrates.[56] Figure 1.7 demonstrates the structure of the DNAzyme and the cleavage of the phosphodiester bond of the substrate.[57] Sequence 5'-GGCTAGCTACAACGA in blue is the catalytic core that possesses the activity of catalyzing the cleavage reaction. The

core is flanked by two binding arms, which can bind to the substrate specifically via Watson-Crick base pairing. The sequence of binding arms has little effect on the cleavage activity so that the DNAzyme can be designed to cleave any substrate. The cleavage site is between a paired pyrimidine Y and unpaired purine R. The cleavage reaction generates two cleaved fragments: one has a 2', 3'-cyclic phosphate on the 3'-end of R and the other has a hydroxyl group on the 5'-end of Y. The cleavage reaction is usually assisted by divalent metal ion cofactors (e.g., Mg^{2+}). The activity of the DNAzyme varies greatly under different cofactor conditions so that comparison of different metal ions and optimization of their concentration is necessary for sensitive detection.

Among the different types of RNA-cleaving DNAzymes, the 10-23 DNAzyme exhibits the highest cleavage activity when using Mn^{2+} as a cofactor.[49, 58] The single turnover number ($k_{obs,s}$) was reported to be higher than 10 min^{-1} at optimal Mn^{2+} concentration. The 8-17 DNAzyme and its variants have different $k_{obs,s}$ values ranging from 4 to 10 min^{-1}.[59-64] In contrast, the Mg^{2+}-dependent DNAzyme has a $k_{obs,s}$ of only 0.039 min^{-1}.[65] Thanks to the high activity of 10-23 DNAzyme, its catalytic core has been split to engineer MNAzyme for the specific detection of different nucleic acid targets.[50]
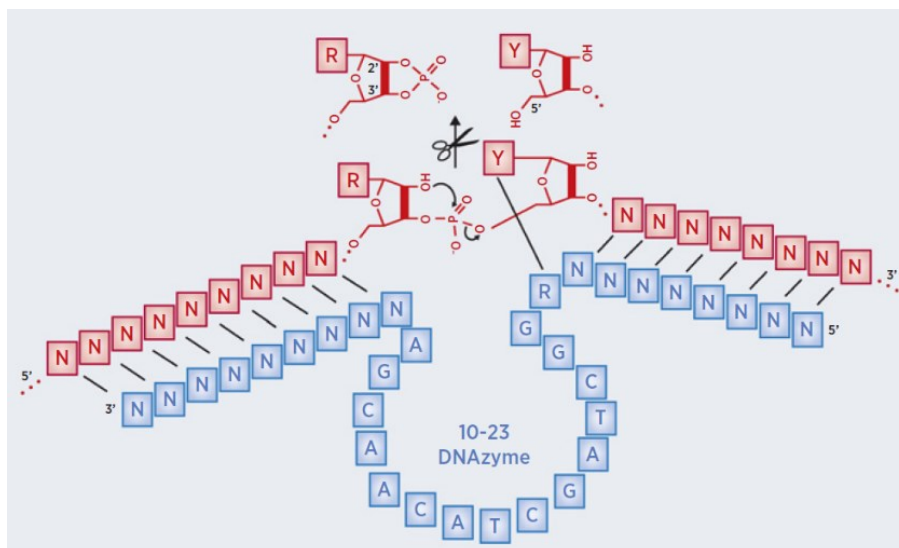
Figure 1.7. Structure of the 10-23 RNA-cleaving DNAzyme and its cleavage of the RNA substrate.[57] The 10-23 DNAzyme hybridizes with the substrate through Watson-Crick base pairing. The cleavage site is between an unpaired purine (R) and a paired pyrimidine (Y). Reprinted with permission. Copyright 2019, American Association for Cancer Research.

1.4.2 MNAzyme for nucleic acid detection

Engineering DNAzymes into MNAzymes is a promising strategy for the detection of nucleic acids because MNAzymes are programmable to recognize any targets. Todd's research group first reported this concept by systematically studying the 10-23 DNAzyme.[50] As demonstrated in Figure 1.8, the DNAzyme is first split into two subunits, also called partial DNAzymes. Each of them contains a substrate arm (binding arm) and a split core. Then, a sensor arm designed to be complementary to the assembly facilitator (nucleic acid target) is added to the subunit. Without the target, neither subunit has

catalytic activity because there is no intact catalytic core. However, the hybridization of two sensor arms with the target can bring them together to form an intact core. Consequently, MNAzyme is activated to cleave its substrate. Since the activation of MNAzyme requires the hybridization of two sensor arms to one target, the detection of nucleic acid targets using this strategy usually has a low background.

The split location of the catalytic core is a key factor in designing the MNAzyme with high cleavage activity. Different split locations of 10-23 DNAzyme have a 1000-fold difference of $k_{obs,s}$, ranging from 0.0017 to 1.2 min^{-1}.
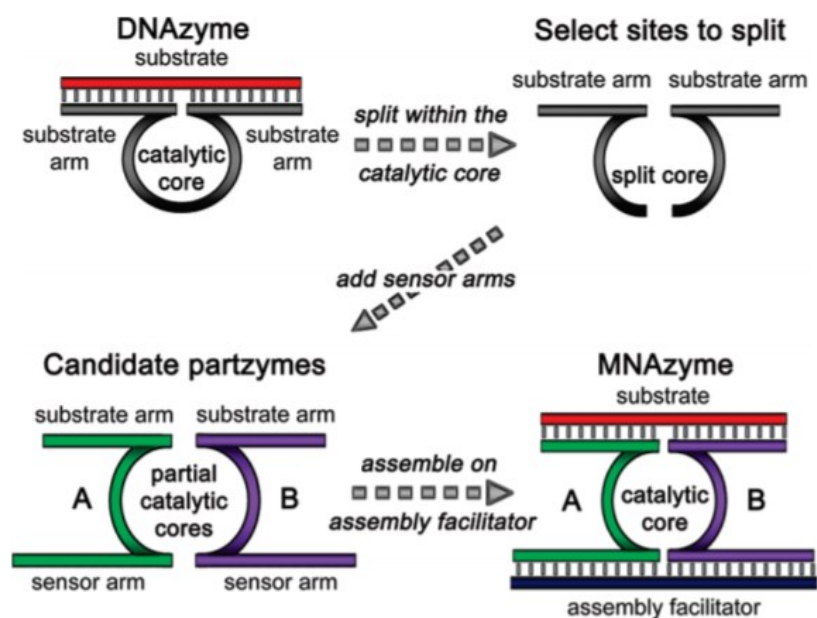
Figure 1.8. Engineering of an MNAzyme from a DNAzyme. The catalytic core of DNAzyme is split into two partial DNAzymes. Sensor arms are added to design two candidate partzymes A and B. Reprinted with permission.[50] Copyright 2010 American Chemical Society.

1.4.3 Incorporating cleavage activity of DNAzyme with isothermal amplification techniques

In contrast to the indiscriminate *trans*-cleavage activity of CRISPR-Cas12a, the activity of DNAzyme can be used for cleaving specific sites. Taking advantage of this property, Meng et al. incorporated DNAzyme with the RCA technique to develop a feedback amplification assay for the sensitive detection of nucleic acids.[53] The existing exponential RCA strategy employing two primers cannot be precisely controlled and may generate high background.[54] The combination of RCA and DNAzyme uses only one primer to achieve exponential amplification so that this strategy can avoid such issues. Figure 1.9 demonstrates the RCA-DNAzyme feedback amplification. Complex I consists of a DNA primer (DP) and circular DNA template (CDT). DP can be regarded as the target and CDT records the complementary sequence of DNAzyme. The amplification extends the DP to generate identical sequence repeats paired to the template $(MgZ)_n$, which consists of thousands of DNAzymes. Complex II also has a primer binding to the CDT. However, this primer, RNA-containing DNA sequence (RDS), is blocked by the cleavage site (red sequence). Therefore, RCA cannot amplify it before cleavage. The DNAzyme product of initial RCA from Complex I is designed to cleave this site to unblock the primer. Cleaved Complex II is then trimmed by the polymerase to act as Complex I and this accelerates the amplification of DNAzyme. As a result, the RCA reaction forms the feedback with the cleavage reaction of Complex II. Without using two primers, the authors achieved

exponential RCA and a sensitivity of aM levels for the detection of the nucleic acid targets.
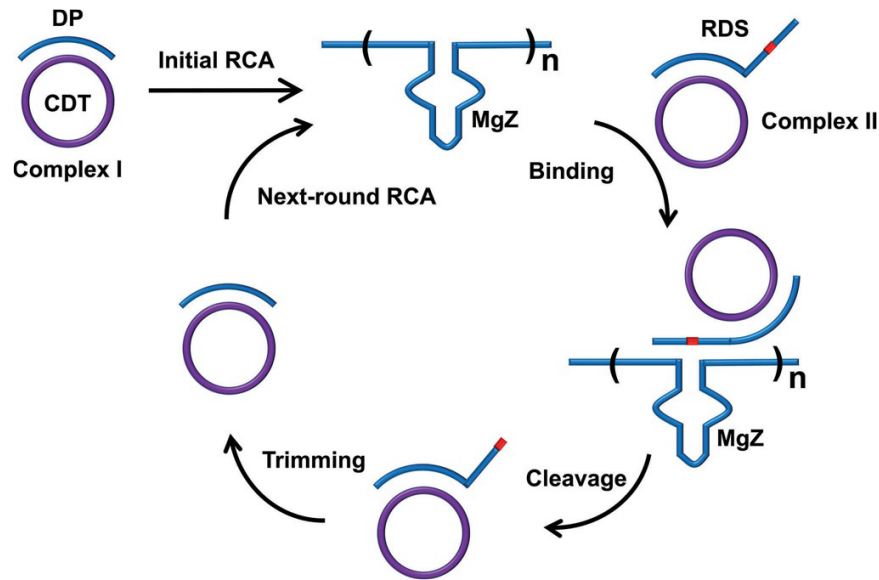
Figure 1.9. Incorporating the cleavage activity of DNAzyme with RCA.[54] DP is a DNA primer that can be regarded as the target. CDT is the circular DNA template of the RCA. MgZ is the DNAzyme amplified by RCA. RDS is an RNA-containing DNA sequence, which serves as the substrate of the DNAzyme. The DNAzyme can specifically cleave the red sequence in RDS, which allowed Complex II to be trimmed by the polymerase. Reprinted with permission. Copyright 2018 John Wiley and Sons.

The cleavage activity of DNAzyme has also been incorporated with the catalytic hairpin assembly (CHA) technique.[52] The product of CHA was designed to be DNAzyme, which could cleave a specific site of the substrate to release more catalytic DNA from

CHA. Thus, the CHA and DNAzyme formed the positive feedback. CHA continuously generated DNAzyme, and meanwhile the cleavage reaction of DNAzyme accelerated CHA by producing catalytic DNA.

The programmable feature of the DNAzyme cleavage has been successfully integrated with the isothermal amplification techniques. However, these methods cannot be easily applied for different targets because the sequences of the template or the hairpin need to be redesigned. The ligation of the circular template of RCA requires overnight preparation and the hairpin of CHA needs to be carefully programmed to avoid nonspecific assembly. It is still necessary to develop a method of detecting different nucleic acid targets without changing the design of the system. Since the MNAzyme technique can be readily used to detect various nucleic acids, it may be an alternative strategy to develop the combined assay of isothermal amplification and DNAzyme for universal targets.

1.5 Homogeneous binding assays for protein detection

In contrast to ELISA, homogeneous binding assays for the detection of protein targets obviate the tedious protocol and false-positive results from non-specific adsorption.[66] The reagents and sample of these assays are mixed in a single test tube. Thus, the overall protocol of the assays has only mixing and reading steps. A homogeneous binding assay is composed of a target recognition probe and a signal transducer. The probe can recognize

the target of interest through affinity ligands, such as aptamers (or antibodies). When the protein target appears, the aptamer can bind with the target by folding into a specific conformation.[67-71] Such conformational change releases the aptamer from its complementary sequence. The aptamer and the complementary sequence are labeled with the fluorophore and the quencher, which work as the signal transducer. Therefore, the change separates two groups and a turn-on fluorescence signal is generated. The combination of different recognition probes and signal transducers realizes the development of versatile homogeneous binding assays.[66]

1.5.1 Proximity ligation assay

The proximity ligation assay (PLA) is a typical example of homogeneous binding assays that uses aptamer as affinity ligand and output DNA as signal transducer.[72-73] Landegren's group used PLA to detect the platelet-derived growth factor B-chain (PDGF-BB). As shown in Figure 1.10, each proximity probe consists of an aptamer (black sequence) and an extension sequence (blue or red sequence). When two aptamers bind to two epitopes of PDGF-BB, the 3'-end of the blue sequence and the 5'-end of the red sequence are brought into close proximity. As a result, the two extension sequences can stably hybridize with the connector (black sequence with bridge structure) and the ligase can join their two ends to form an intact DNA loop, which is the signal transducer that can be amplified by PCR. The sequence in green labeled with the fluorophore group (F) and quencher (Q) is the readout of the PCR product.

In PLA, the detection of input protein is converted to the detection of output nucleic acid. This strategy enhances the sensitivity of protein detection. Though there is no technique that can directly amplify the protein molecules, PCR can amplify the output nucleic acid for the sensitive detection of target. It was reported that the detection limit of PDGF-BB using PLA was as low as zeptomole level (10^{-21} mol).[72] PLA is not limited to the detection of PDGF-BB. By changing the recognition probes to other aptamers and antibodies, the researchers were able to detect a wide range of protein targets.
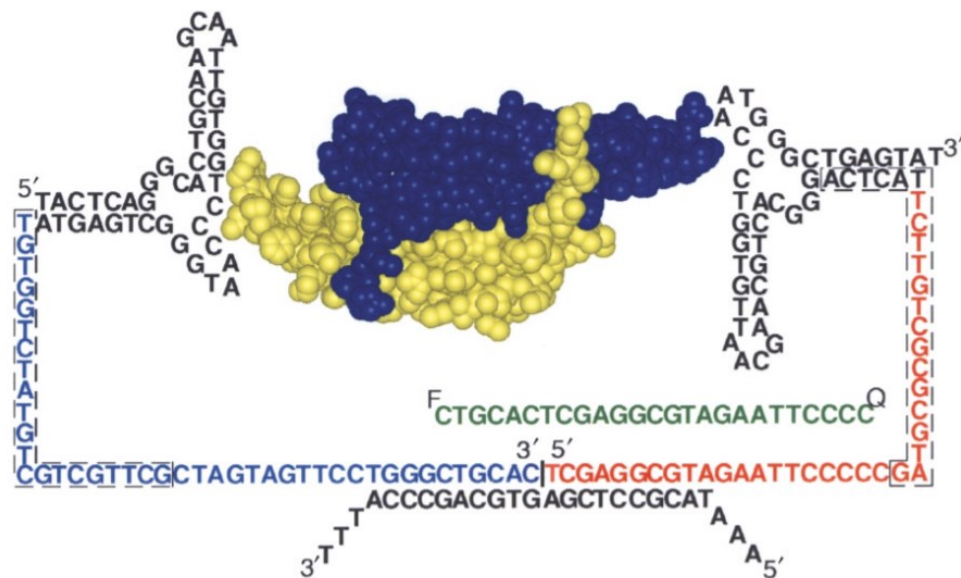
Figure 1.10. Scheme of the PDGF-BB detection using PLA.[72] Two sequences in black are aptamers specific for the PDGF B-chain. The sequences in blue and red are joined by the ligation upon hybridization to the connector DNA. A probe in green is used for the real-time detection of PCR product. Reprinted with permission. Copyright 2002 Nature Publishing Group.

1.5.2 BINDA technique

Inspired by PLA, our group developed another homogeneous binding assay technique, termed binding-induced DNA assembly (BINDA).[74-79] Similar to PLA, BINDA can convert the input protein to the output DNA assembly, which triggers the downstream reaction that can be monitored. Moreover, the output DNA can assemble only when two recognition probes bind to the same target. Thus, BINDA is a sensitive and specific technique for protein detection. BINDA can be performed in a single test tube without any immobilization, separation, and washing steps. It has the potential to be applied to the POC analysis of protein targets relevant to clinical diagnosis.

Figure 1.11 demonstrates the principle of BINDA.[74] Motif-F and Motif-R are two sequences composed of BINDA regions (2 and 5), spacers (1 and 4), and recognition probes (Probe-F and Probe-R). Motif-F also has a hairpin structure (3). Assembly of regions 2 and 5 can occur only when Probe-F and Probe-R recognize the same target. BINDA regions 2 (AGGCTG) and 5 (CAGCCT) are complementary to each other but they have a melting temperature (T_m) less than 10 °C, indicating they cannot hybridize stably at room temperature. After Probe-F and Probe-R bind to the same protein target, the two motifs come to close proximity. Consequently, the T_m of hybridization between BINDA regions 2 and 5 dramatically increases to 50 °C and they can form a stable duplex. Spacers 1 and 4 ensure the flexibility of interaction between the two motifs. Blocker-F

and Blocker-R are capable of blocking the BINDA regions 2 and 5 to prevent them from

forming target-independent assembly.
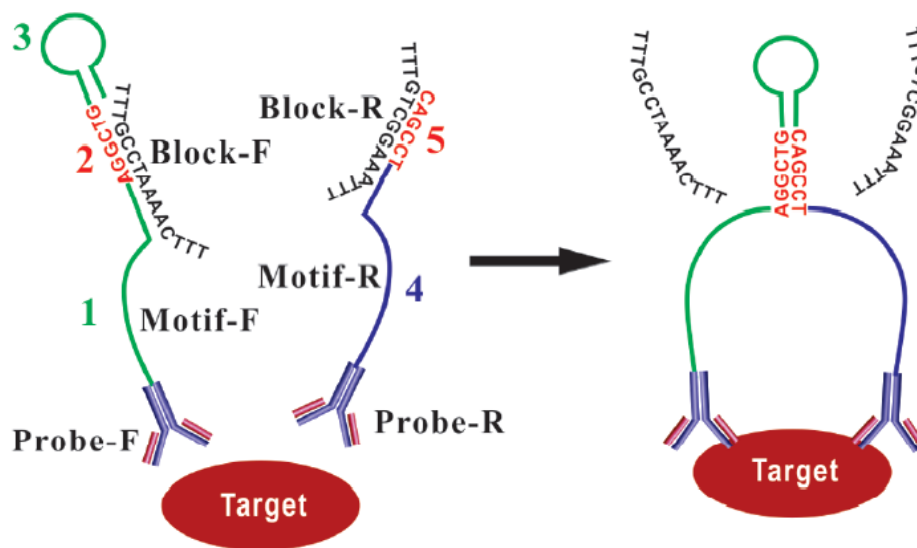
Figure 1.11. Scheme of BINDA. Reprinted with permission.[74] Two DNA motifs contain

short complementary sequences in red, blocker F/R, and affinity probes F/R. Short

complementary sequences cannot form duplex when there is no target. In the presence of

protein target, two probes bind to two epitopes, leading to the displacement of the blocker

and hybridization between short complementary sequences. Copyright 2011 American

Chemical Society.

The increase of T_m is attributed to the higher local concentration of two motifs (Figure

1.12).[77] If a drip of 1.7 fL solution contains two molecules of DNA motifs, their local

concentration is only 1 nM. The binding of two motifs to the target significantly reduces

the distance between them. Since a typical intramolecular distance is approximately 10

nm, the new drip has a diameter of 20 nm and a volume of 4.2 zL. Therefore, the local

concentration of two motifs increases dramatically, about 400000-fold, to 400 µM.
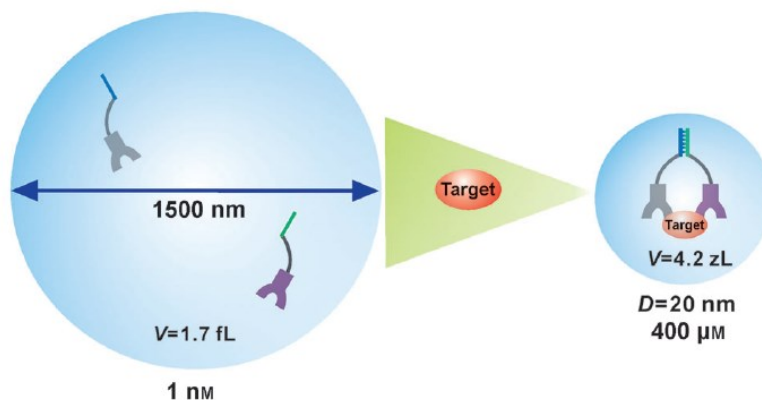
Figure 1.12. After binding to the target, the local concentration of two BINDA motifs

increases from 1 nM to 400 µM (4 x10^5-fold).[77] Reprinted with permission. Copyright

2013 Wiley-VCH.

1.5.3 Combining MNAzyme with BINDA for protein detection

In recent years, the MNAzyme technique has been applied to the detection of protein

targets. Ju and coworkers pioneered the detection of proteins using MNAzyme-based

assays.[80] As shown in Figure 1.13, they designed three subunits to form the MNAzyme

based on the 10-23 DNAzyme. Each subunit contained a DNA sequence labeled with an

antibody. Subunits DNA1 and DNA2 had the sequences of the partial DNAzymes, and

subunit DNA3 was responsible for the assembly of DNA1 and DNA2. Upon binding to

the target, the three subunits formed the MNAzyme with a four-arm structure to cleave the substrate on the gold electrode, leading to the output electrochemical readout. Other research groups used MNAzymes with the three-arm structure based on the Mg^{2+}-dependent DNAzyme.[81-83] Although there are many reported works of protein detection using the MNAzyme technique, there is no systematic research on the investigation of the MNAzyme activity in this scenario. Because the splitting of the DNAzyme greatly affects the MNAzyme activity for nucleic acid detection,[50, 84] it is also necessary to optimize the split location for protein analysis. In addition, comparison of the four-arm and three-arm structure may also improve the activity as both secondary structures have been reported in the literature.
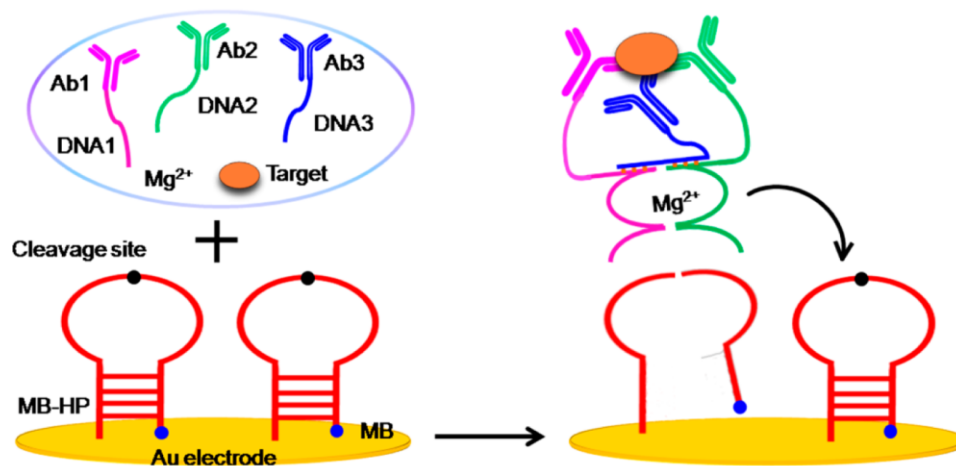
Figure 1.13. MNAzyme for protein detection using three subunits and four-arm structure.[80] DNA1 and DNA2 contain the sequence of MNAzyme subunit. DNA3 serve as the connector of DNA1 and DNA2. Copyright 2015 American Chemical Society.

BINDA is a potential platform for protein detection using the MNAzyme technique because these two techniques share several similarities and advantages. First, both of them need at least two DNA subunits or motifs, which consist of target recognition probes and functional regions.[50, 74] In the BINDA technique, two DNA motifs contain aptamers and a BINDA region. Two subunits of MNAzyme have sensor arms and a partial catalytic core. Second, both techniques result in DNA assembly upon target binding. As a result of aptamers' binding to the protein target, the T_m of short complementary BINDA regions dramatically increases and leads to their stable hybridization. When two sensor arms hybridize to the nucleic acid target, partial DNAzymes are brought together to form an intact catalytic core. Third, the output DNA assembly of the two techniques is amplifiable. BINDA converts the protein target to the assembled DNA sequences that can be amplified by PCR and isothermal amplification techniques.[77] The assembly of MNAzyme results in the cleavage of substrate, which has been used to accelerate RCA and CHA.[52, 54] Fourth, both techniques have good specificity because they have two recognition probes to bind to one target. Two motifs of the BINDA technique have to bind to two different epitopes on the same protein molecule. The activity of the MNAzyme can be restored only when two sensor arms hybridize with the same nucleic acid target. The detection format of the sandwich structure enhances the specificity against the cross-activity of antibodies and mismatch of nucleic acid targets.

1.6 Rationale of the program

Homogeneous and isothermal detection methods for nucleic acids and proteins are promising for POC applications. Conventional techniques, ELISA and PCR, are sensitive and robust in laboratory settings. However, they are not ideal for POC applications because PCR requires a thermal cycler for controlled temperature cycling and ELISA needs multiple washing steps. In contrast, isothermal amplification techniques can be performed without the need for a thermal cycler and the homogeneous binding assays eliminate the washing steps.

During the COVID-19 pandemic, the CRISPR-Cas technology has been incorporated with isothermal amplification techniques to improve the specificity and sensitivity of the detection of SARS-CoV-2 viral RNA. Although RT-LAMP can efficiently amplify the target in a short time, the commonly used detection dyes do not provide specificity, potentially resulting in false-positive results from the nonspecific amplicons. The CRISPR-Cas12a system has been used to recognize the specific amplicons because the guide RNA (gRNA) binds to the dsDNA amplicon and CRISPR-Cas12a has a high *trans*-cleavage activity. Only the amplicons of viral RNA can activate CRISPR-Cas12a to cleave the reporter substrate. So far, the detection formats for the diagnosis of COVID-19 are mainly fluorescence and lateral flow strip, which require additional equipment for the signal readout. A colorimetric detection format using CRISPR-Cas12a, on the other hand, can overcome this issue.

The cleavage activity of DNAzyme has also been integrated with isothermal amplification techniques to improve the sensitivity and minimize the background. RCA was used to amplify multiple DNAzymes, which were designed to cleave a specific RNA site to unblock the RCA template. The positive feedback was built between RCA amplification and the cleavage reaction of DNAzyme to achieve exponential amplification. Compared to the existing exponential RCA method, only one primer is required and the background can be controlled easily. However, the circular template needs overnight preparation. It is difficult to apply the method for the detection of various targets because each template is for one individual target only. Thanks to the programmable target recognition feature of the MNAzyme technique, incorporation of the DNAzyme with isothermal amplification technique can be used for sensitive detection of different nucleic acid targets without changing the sequence design of the positive feedback system.

Recently, MNAzymes have also been applied to the detection of proteins. In the published studies, MNAzymes were used for protein detection without comparing different split locations of the DNAzyme. Nevertheless, the split location can dramatically affect the activity of MNAzymes by 1000-fold when used for nucleic acid detection. On the other hand, both the four-arm structure and the three-arm structure of MNAzymes have been reported to recognize protein targets. A systematic investigation of these two secondary structures may also enhance the catalytic activity of protein-targeting MNAzymes.

Since BINDA is similar to the MNAzyme technique in the aspect of probe design, it is an ideal platform to develop MNAzyme-based homogeneous binding assays for proteins. By changing the sensor arm to aptamers, I can use protein targets to initiate the formation of MNAzyme and monitor the cleavage reaction to achieve the signal readout.

1.7 Objectives

The three major goals of my thesis research are: (i) incorporating the cleavage activity of CRISPR-Cas12a or DNAzyme with isothermal amplification techniques to detect nucleic acid targets; (ii) investigating the split location and secondary structure of MNAzymes for protein detection; and (iii) using BINDA to develop MNAzyme-based homogeneous binding assays.

The specific aims of each chapter are:

Chapter 2: Develop a colorimetric assay based on RT-LAMP and CRISPR-Cas12a for the detection of SARS-CoV-2 viral RNA.

Chapter 3: Combine SDA with DNAzyme to develop a DNA circuit of feedback amplification for the sensitive detection of different nucleic acid targets without the need to change the sequence design of the feedback system.

Chapter 4: Study 14 split locations and two secondary structures to select the MNAzyme of optimal catalytic activity for protein analysis.

Chapter 5: Integrate the MNAzymes with the BINDA technique to design binding-assembled MNAzymes for the detection of two model protein targets.

Chapter 2 CRISPR-Cas12a-mediated gold nanoparticle aggregation for colorimetric detection of SARS-CoV-2

2.1 Introduction

CRISPR-Cas systems have revolutionized our capability for genome editing[41, 85-88] and have also been used to improve isothermal amplification techniques in recent years.[40] Incorporation of CRISPR-Cas systems before the amplification can enrich the nucleic acid targets at low abundance in matrix samples.[89-90] CRISPR-Cas systems can also be incorporated after the amplification to avoid false positive results from nonspecific amplicons, thus enhancing the specificity of detection.[43-44, 91]

During the global pandemic of COVID-19, CRISPR-Cas systems have been applied to the detection of SARS-CoV-2 viral RNA.[39, 46, 92-93] The *trans*-cleavage activity of CRISPR-Cas systems can improve the specificity of the isothermal amplification (e.g., RT-LAMP and RT-RPA) as well as generate different types of detectable signals for various detection platforms. The activation of CRISPR-Cas systems requires the hybridization of specific sequences of amplicons to the spacer region of gRNA. Researchers also took advantage of its *trans*-cleavage activity to cleave the dually labeled substrate and achieve the fluorescence or lateral flow detection of SARS-CoV-2.[94-95]

However, fluorescence methods require the excitation light source and lateral flow platforms require paper strips. A colorimetric assay that does not need extra equipment for visual detection has not been fully exploited for the SARS-CoV-2. The reported assays

either are not sensitive or need a long time to generate the color change.[96-97] In this chapter, I designed a colorimetric assay that incorporated RT-LAMP and CRISPR-Cas12a to facilitate the aggregation of AuNPs for the isothermal, sensitive, specific, and visual detection of SARS-CoV-2. The CRISPR-Cas12a activated by specific RT-LAMP amplicons can cleave the rationally designed hairpin transducer to facilitate the aggregation of AuNPs. With a portable spinner, I achieved a recognizable color change within 1 min.

2.2 Materials and methods

Preparation of SARS-CoV-2 viral RNA

The original SARS-CoV-2 virus strain was obtained from the University of Saskatchewan, Canada (SARS-CoV-2/CANADA/VIDO 01/2020). The virus was generated from the infection of Vero-E6 cells. RT-qPCR was used to detect the N gene and quantify the amount of viral RNA.

Reagents

Other nucleic acids used in this study were synthesized by Integrated DNA Technologies (IDT; Coralville, IA, USA). Reagents for RT-LAMP and *trans*-cleavage reactions, including Bst 2.0 polymerase, WarmStart RTx reverse transcriptase, deoxynucleotide (dNTP), isothermal amplification buffer, NEBuffer 2.1 and EnGen Lba Cas12a, were purchased from New England BioLabs (NEB; Whitby, ON, Canada) except for the RNAse inhibitor (Invitrogen). The 20 nm AuNP (7.0 x10^{11}/mL) were purchased

from Ted Pella (Redding, CA, USA). Tween 80 was from Fisher Scientific (Fair Lawn, NJ, USA).

Swab samples and RNA extraction

All respiratory swab samples used in this study were collected and treated by Alberta Precision Laboratories, Canada. Three extraction platforms, NUCLISENS easyMAG, KingFisher Flex System, and STARlet automated extractor, were from BioMerieux, Thermo Fisher Scientific, and Hamilton, respectively.

RT-LAMP reaction

Table 2.1 summarizes the sequences of RT-LAMP primers and the target regions in the N and E genes of viral RNA. The 25 μL reaction of RT-LAMP contained 1.4 mM dNTP, 1x isothermal amplification buffer, 8 mM $MgSO_4$ (including 2 mM $MgSO_4$ in 1x isothermal buffer), 5 μM outer primers F3 and B3, 40 μM inner primers FIP and BIP, 20 μM loop primers LF and LB, 0.3 U/μL WarmStart RTx reverse transcriptase, 0.32 U/μL Bst 2.0 polymerase, and 0.16 U/μL RNase inhibitor. The test tube was placed in the myBlock Mini Digital Dry Bath (Benchmark Scientific) and the RT-LAMP amplification was performed at 62 °C for 30 min.

Table 2.1. The sequences of the RT-LAMP primers and the N/E gene target regions of SARS-CoV-2. In the N and E gene target regions, sequences in red were amplified and their amplicons were the protospacers that guide RNAs (sequences in Table 2.3) of Cas12a could recognize. For each gene target, we employed 6 primers: F3 (forward outer primer), B3 (backward outer primer), FIP (forward inner primer), BIP (backward inner primer), BL (backward loop primer) and FL (forward loop primer). The underlined sequences of the backward primer can hybridize with the target region with the same labels and colors. Similarly, the forward primer can hybridize with the corresponding region of the complementary region of the target.

Name	Sequence (5' → 3')
N gene target region	AAC ACA AGC TTT CGG CAG ACG TGG TCC AGA ACA AAC CCA AGG AAA TTT TGG GGA C CAG GAA CTA ATC AGA CAA GGA A CTG ATT ACA AAC ATT GGC CGC A AAT TGC ACA ATT TGC CCC CAG CGC TTC AGC GTT CTT CGG AAT GTC G CGC ATT GGC ATG GAA GTC AC ACC TTC GGG AAC GTG GTT GAC CTA CAC AGG TGC CAT CAA A TT GGA TGA CAA AGA TCC AAA TTT C
N-F3	AAC ACA AGC TTT CGG CAG
N-B3	G AAA TTT GGA TCT TTG TCA TCC

Name	Sequence (5' → 3')
N-FIP	**T GCG GCC AAT GTT TGT AAT CAG** CCA AGG AAA TTT TGG GGA C
N-BIP	*CGC ATT GGC ATG GAA GTC AC T TTG ATG GCA CCT GTG TAG*
N-BL	**T TCC T GATTG TCT TAG TTC**
N-FL	*ACC TTC GGG AAC GTG GTT*
E gene target region	CCG ACG ACG ACT ACT AGC GTG CC TTT GTA AGC ACA AGC TGA TG A GTA CGA ACT TAT GTA CTC A TTC GTT TCG GAA GAG ACA GGT ACG TTA ATA GTT AAT AGC GTA CTT CTT TTT CTT GCT TTC GTG GTA TTC TTG CTA GTT ACA *CTA GCC ATC CTT ACT GCG CT TCG ATT GTG TGC GTA CTG C TGC AAT ATT GTT AAC GTG AGT* CTT GTA A *AAC CTT CTT TTT ACG TTT ACT CT*
E-F3	**CCG ACG ACG ACT ACT AGC**
E-B3	*AG AGT AAA CGT AAA AAG AAG GTT*
E-FIP	**ACC TGT CTC TTC CGA AAC GAA** TTT GTA AGC ACA AGC TGA TG
E-BIP	*CTA GCC ATC CTT ACT GCG CT ACT CAC GTT AAC AAT ATT GCA*
E-BL	**T GAG TAC ATA AGT TCG TAC**
E-FL	*TCG ATT GTG TGC GTA CTG C*

Functionalization of AuNPs

The sequences of two thiolated DNAs for AuNP functionalization are listed in Table 2.2. One milliliter of 20 nm AuNP was first incubated with 100 μL 20% Tween 80 (Sigma-Aldrich) for 5 min in a 2-mL micro test tube. Then, 13 μL 100 μM of DNA was added and the solution was incubated for another 5 min, after which 400 μL 5 M NaCl was added for 3 h salt aging. The molar ratio of DNA to AuNP was approximately 1000:1. After salt aging, the mixture was centrifuged at 21,100 g for 11 min to remove the supernatant solution that contained unconjugated DNA. The washing steps consisting of (i) addition of 1 mL washing buffer (10 mM Tris-HCl + 0.05% Tween 20) to the precipitate, (ii) resuspension of the precipitate in the washing buffer, (iii) centrifuging at 21,100 g for 11 min, and (iv) removal of the supernatant solution, were repeated three times. Finally, the functionalized AuNPs were resuspended in 50 μL washing buffer to a final concentration of 20 nM.

Table 2.2. The sequences of hairpin transducers (HT) and DNA conjugated on AuNP. RNA labeled in orange and dark blue are two crosslinker domains that can hybridize with complementary sequences of 'AuNP-DNA1' in bold and 'AuNP-DNA2' in italics, respectively. Underlined sequences of 'AuNP-DNA1' and 'AuNP-DNA2' are the complementary regions of 'HT18-InvdT'. Activated Cas12a can *trans*-cleave the DNA substrate in black. The DNA lock domain of HT in bold and light blue can form a hairpin structure by self-binding to the RNA linker region in dark blue. 'HT-t1' indicates the HT of toehold design has a 1-nt toehold. 'HT20' means the HT of no-toehold design has a crosslinker domain of 20 nt (10+10). 'HT18-InvdT' has the same sequence of 'HT18' except that its 3'-end is modified with the inverted dT. 'AuNP-DNA1' and 'AuNP-DNA2' are functionalized with the thiol group at the 5'-end for AuNP conjugation.

Name	Sequence (5' → 3')
HT-t1	rArUrC rUrCrU rUrCrC rUrArU rArGrU rUrGrU rArArC rCrUrG rUrCrU rCrUrC TTA TTA TTA TTA TTA TTA TTA TTA TTA TTA TTA TTA TTA TTA TTA TTA TT **GAG AGA CAG GTT AC**
HT-t2	rArUrC rUrCrU rUrCrC rUrArU rArGrU rUrGrU rArArC rCrUrG rUrCrU rCrUrC TTA TTA TTA TTA TTA TTA TTA TTA TTA TTA TTA TTA TTA TTA TTA TTA TT **GAG AGA CAG GTT A**

Name	Sequence (5' → 3')
HT-t3	rArUrC rUrCrU rUrCrC rUrArU rArGrU rUrGrU rArArC rCrUrG rUrCrU rCrUrC TTA TTA TTA TTA TTA TTA TTA TTA TTA TTA TTA TTA TTA TTA TTA TTA TT **GAG AGA CAG GTT**
HT-t4	rArUrC rUrCrU rUrCrC rUrArU rArGrU rUrGrU rArArC rCrUrG rUrCrU rCrUrC TTA TTA TTA TTA TTA TTA TTA TTA TTA TTA TTA TTA TTA TTA TTA TTA TT **GAG AGA CAG GT**
HT20	rArUrC rUrCrU rUrCrC rU rUrGrU rArArC rCrUrG rU TTA TTA TTA TTA TTA TTA TTA TTA **A CAG GTT ACA**
HT18	rArUrC rUrCrU rUrCrC rUrGrU rArArC rCrUrG TTA TTA TTA TTA TTA TTA TTA TTA **CAG GTT ACA**
HT16	rArUrC rUrCrU rUrC rUrGrU rArArC rCrU TTA TTA TTA TTA TTA TTA TTA TTA **AG GTT ACA**
HT18-InvdT	rArUrC rUrCrU rUrCrC rUrGrU rArArC rCrUrG TTA TTA TTA TTA TTA TTA TTA TTA **CAG GTT ACA** -InvdT
AuNP-DNA1	HS-TTA TC **ACT ATA** GGA AGA GAT
AuNP-DNA2	HS-TTG CA *GAG AGA CAG GTT ACA*

Cas12a-mediated AuNP aggregation

Table 2.3 lists the sequences of the two gRNAs that recognize the RT-LAMP amplicons of N gene and E gene, respectively. Table 2.2 lists the sequences of HT. HT18-InvdT was used to perform the colorimetric detection of the SARS-CoV-2 viral RNA target and clinical samples.

First, 2 µM Cas12a protein was incubated with 3 µM gRNA in 1x NEBuffer 2.1 to form 2 µM ribonucleoprotein (RNP) complex. The 30 µL reaction solution contained 200 nM RNP, 1 µM linker, 20 nM DNA activator (Table 2.3, or nuclease-free water as negative control) and 1x NEBuffer 2.1. This solution was incubated at room temperature for 10 min for *trans*-cleavage of HT. Afterward, 30 µL AuNP solution containing 2 nM of each AuNP and 1.67 M NaCl was added to initiate the aggregation. The final concentration of AuNP and NaCl were 1 nM and 0.83 M respectively in the 60 µL mixture. After 1 min of incubation, the mixture was centrifuged for 10 s in the spinner at 3000 rpm. A photograph of the test tube was taken using a smartphone camera. Finally, 50 µL of the centrifuged mixture was loaded onto a 96-well plate to record the ultraviolet–visible (UV-Vis) spectrum at 400–700 nm.

Table 2.3. Sequences of Cas12a gRNA and DNA activator. In the two gRNA, the sequences in red are the spacer regions. The N gene activator is dsDNA composed of two strands, 1 and 2. The red sequence of strand 2 is the protospacer region. The blue sequence of strand 1 is the protospacer adjacent motif (PAM) region.

Name	Sequence (5' → 3')
N-gRNA	UAA UUU CUA CUA AGU GUA GAU CCC CCA GCG CUU CAG CGU UC
E-gRNA	UAA UUU CUA CUA AGU GUA GAU GUG GUA UUC UUG CUA GUU AC
N-activator strand 1	GCA AAT GCA ACA A TTT G CCC CCA GCG CTT CAG CGT TC TTC GGA ATG TCG C
N-activator strand 2	G CGA CAT TCC GAA GA ACG CTG AAG CGC TGG GGG C AAA T TGT GCA ATT TGC

2.3 Results and discussion

The principle of CRISPR/Cas12a-mediated AuNP aggregation

As shown in Figure 2.1, I designed the gRNAs that direct Cas12a to bind to the specific RT-LAMP amplicons of N gene or E gene of SARS-CoV-2. Upon binding of the Cas12a-gRNA RNP to the amplicons, the *trans*-cleavage activity of Cas12a is initiated to cleave the ssDNA loop of the HT. HT is composed of three functional domains, a DNA

lock domain, an RNA crosslinker domain, and a DNA loop substrate domain. Cleavage of the loop changes the nature of the hybridization between the lock and crosslinker from intra- to inter-molecular interaction. Therefore, the hybridization is destabilized and the crosslinker is liberated to hybridize to two ssDNA sequences functionalized on two AuNPs, thus leading to the aggregation of AuNPs and the color change from red to purple.

I designed the HT to contain not only the substrate domain of Cas12a-gRNA RNP but also the lock domain to avoid the background in the negative sample. When there is no viral RNA in the sample, the RNP remains inactive and the lock partially hybridizes with the crosslinker and cages it in the hairpin structure. Consequently, the lock prevents the crosslinker from assembling two AuNPs. Since Cas12a only *trans*-cleaves ssDNA but not ssRNA, the crosslinker domain was designed to be RNA and the loop to be DNA. At the 3'-end of the lock domain, I added an *inverted* thymine to inhibit its extension by the polymerase in the RT-LAMP mixture. The extension enables the lock to fully hybridize with the crosslinker so that the cleavage of the loop can no longer separate them.
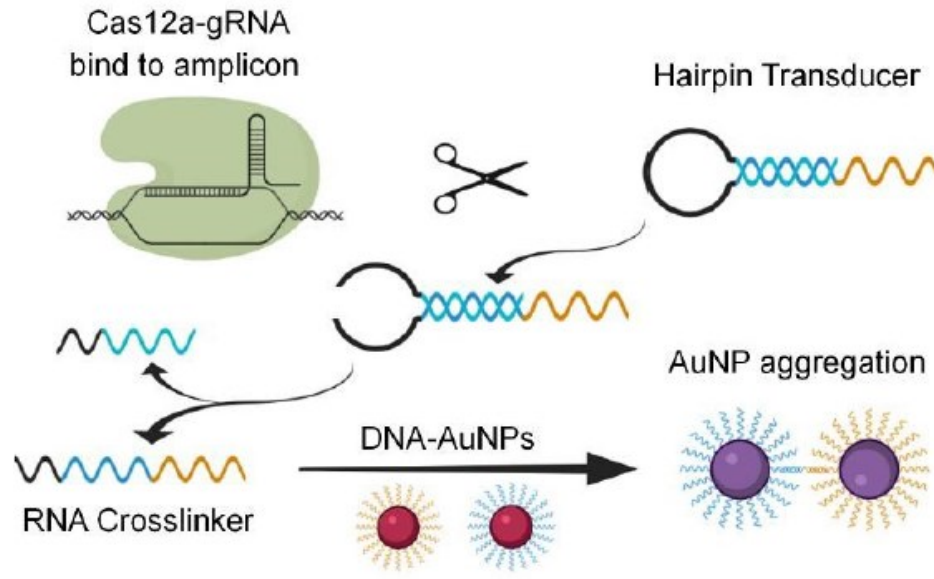
Figure 2.1. The principle of the CRISPR-Cas12a-mediated AuNP aggregation. The Cas12a-gRNA ribonucleoprotein specifically binds to the target sequence of the double-stranded DNA amplicon, which activates the Cas12a-gRNA ribonucleoprotein. This active enzyme trans-cleaves the DNA loop of the hairpin transducer, which destabilizes the hairpin and releases the RNA crosslinker from its hybrid. Hybridization of the RNA crosslinker with the ssDNAs on AuNPs results in the aggregation of AuNPs and the corresponding change in color from red to purple.

The operation of the assay

The operation to detect viral RNA samples is simple, isothermal, and can be done in under 45 min (Figure 2.2). After the extraction of viral RNA from the sample (e.g., nasopharyngeal swab), RT-LAMP is performed to amplify the target for 30 min at 62 °C in the portable heating block. The Cas12a-gRNA RNP and HT are then added to the RT-LAMP solution to initiate the *trans*-cleavage of the ssDNA loop for 10 min at room temperature. Finally, two types of AuNPs were added to initiate the aggregation of AuNPs and the color change. An obvious color change can be shown in 1 min after the centrifugation of the test tubes in a spinner at 3000 rpm for 10 s. The clear precipitation of AuNP aggregates can be observed in the positive sample and the solution of the negative sample remains a red color.
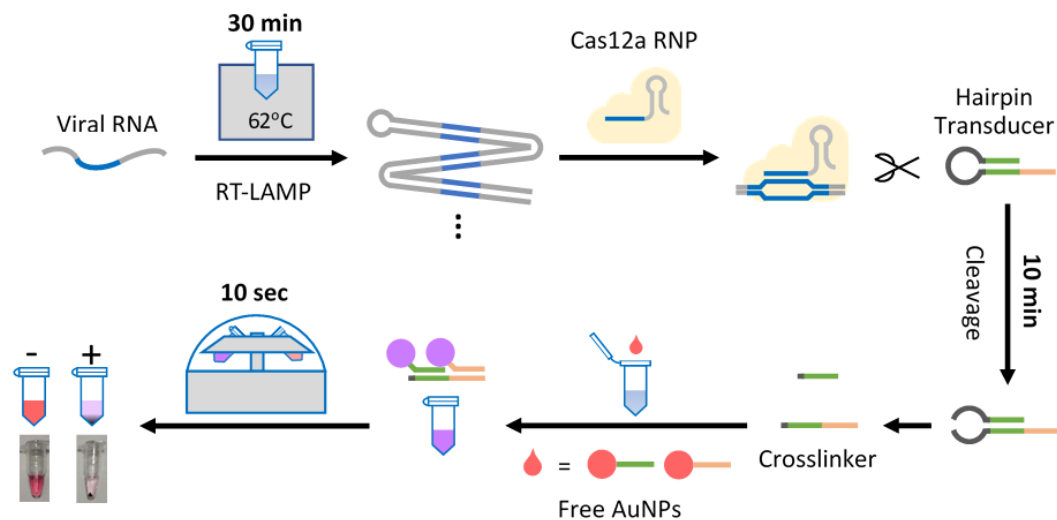
Figure 2.2. Schematic demonstrating the operation of RT-LAMP and CRISPR-Cas12a-mediated aggregation of AuNPs for the colorimetric detection of viral RNA. The viral RNA is first amplified by the RT-LAMP at 62 °C for 30 min. Cas12a-gRNA RNP is added into the RT-LAMP reaction solution for binding to the specific region of amplicons. Cas12a-gRNA RNP is then activated to cleave the DNA loop of the hairpin transducer. The trans-cleavage reaction is performed at room temperature for 10 min. Consequently, the RNA crosslinker in the hairpin transducer is released from the lock. The crosslinker brings AuNPs together, generating AuNP aggregates and causing the color change from red to purple. The solution is centrifuged using a portable spinner to precipitate the aggregates, resulting in a clear color change of the solution.

Two designs of the hairpin transducer

To achieve the rapid response of color change, I had to design the HT to efficiently liberate the crosslinker from the lock upon the *trans*-cleavage of the loop. In addition, the crosslinker must be stably blocked by the lock to ensure low background. Therefore, I proposed and compared two types of HT, the toehold design and the no-toehold design (Figure 2.3), for these two aims. Both HT designs have a DNA loop, a DNA lock, and an RNA crosslinker. The RNA crosslinker has two subdomains, I and II, which can respectively hybridize with the two DNAs (I* and II*) functionalized on the AuNPs (DNA-AuNPs).
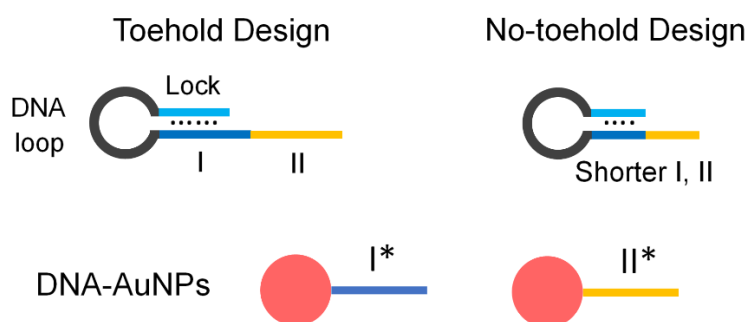
Figure 2.3. Two designs of the hairpin transducer. Hairpin transducers composed of a RNA crosslinker, a DNA loop, and a lock sequence. The RNA crosslinker sequence (subdomains I and II) within the hairpin transducer are complementary to the ssDNA sequences (I* and II*) that are conjugated on two separate AuNPs. In the toehold design, subdomain I is partially blocked by the lock sequence, leaving the unblocked portion to function as the toehold for toehold-mediated strand displacement of the lock.

The subdomain I of the toehold design is only partially blocked by the lock domain, leaving the unblocked portion to work as the toehold. The length of the two subdomains is 15 nt and the lock has a length of 11–14 nt. Using a lock shorter than subdomain 1, I designed the HTs with a toehold of 4–1 nt. I intended to design a long lock to firmly block the crosslinker and achieve low background. The hybridization between the lock and subdomain I is stable at room temperature (T_m > 54.5 °C) even after the cleavage of the loop. Therefore, a toehold is necessary for the fast interaction between the subdomains I and I* functionalized on the AuNP via toehold-mediated strand displacement reaction. Theoretically, a long toehold of 4 nt can result in the rapid displacement of lock, but the risk of leakage of the HT and high background increases. A short toehold of 1 nt is not favorable for the displacement but has low background. Therefore, I compared four HTs of different toehold lengths from 1 to 4 nt.

I also proposed the no-toehold design of the HT to completely eliminate the leakage. The subdomain I is fully blocked by the lock so that there is no toehold. As mentioned above, the lock can form a stable duplex with subdomain I at room temperature when there are more than 11 base pairs. Thus, a shorter subdomain and lock were used for the no-toehold design to allow the spontaneous dissociation of the lock after the *trans*-cleavage reaction. Nevertheless, the lock and crosslinker cannot be too short because the subdomains I and II can hardly hybridize with the subdomains I* and II* on the AuNPs. To achieve efficient AuNP aggregation, I designed and compared five crosslinkers of 6+6 (subdomain I + II), 7+7, 8+8, 9+9, and 10+10 nt (Table 2.4).

Table 2.4. Sequences of crosslinkers used for the study of crosslinker length, NaCl concentration, and effect of centrifugation. Sequences in orange and blue are crosslinker domains that can respectively hybridize with complementary sequences of 'AuNP-DNA1' in bold and 'AuNP-DNA2' in italics (Table 2.3).

Name	Sequence (5' → 3')
L20	ATC TCT TCC T TGT AAC CTG T
L18	ATC TCT TCC TGT AAC CTG
L16	ATC TCT TC TGT AAC CT
L14	ATC TCT T TGT AAC C
L12	ATC TCT TGT AAC

Investigation of the toehold design

I first tested the performance of four HTs of toehold design to compare different lengths of the toehold. A 20 nM DNA activator was used to activate RNP and trigger *trans*-cleavage reaction of the HT. If the HTs can crosslink two types of DNA-AuNPs without the *trans*-cleavage, a background is generated that decreases the sensitivity of detection. As demonstrated in Figure 2.4A, background was observed for all four HTs in the negative samples even though they had high thermal stability. To analyze the effect of the length of the toehold, I measured the UV-Vis absorbance spectra of all samples and

the negative control containing no HT (Figure 2.5). I further calculated the difference of absorbance between the samples and negative control (Figure 2.4B). A larger difference suggests a stronger aggregation of AuNPs and vice versa. The shortening of the toehold length clearly reduced the background from the leakage in the negative samples, indicating that the presence of the toehold led to this leakage regardless of the high thermal stability of HTs. In the positive samples, the HTs with longer toeholds resulted in greater aggregation and the largest difference of absorbance was observed for the HT with the longest toehold of 4 nt. This result confirmed that the toehold can accelerate the displacement of the DNA lock and the hybridization between subdomains I and I* .
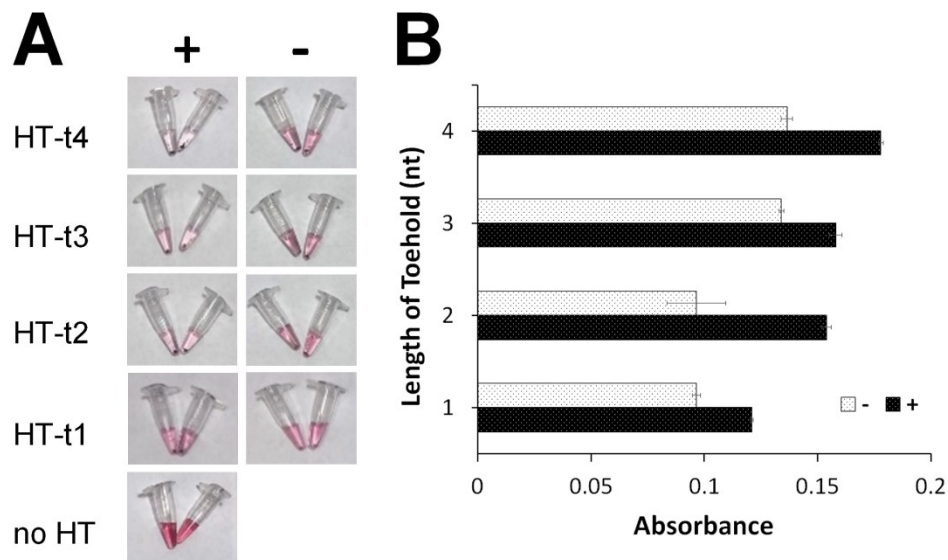
Figure 2.4. Comparison of the HTs with different toehold lengths by colorimetric assay (A) and UV-Vis absorbance (B). '+' indicates samples containing 20 nM model DNA sequence (DNA activator for RNP). '-' indicates samples containing all reagents but no DNA activator. 'no HT' indicates negative control, containing all reagents except hairpin transducer. 'Absorbance' is the difference of UV-Vis absorbance values at 530 nm (Figure 2.5) between the samples and the negative control. The error bars stand for the standard deviations of duplicates. Measurements from multiple independent experiments (n = 2) conducted on different days gave consistent results. Each bar in this figure represents the average of two measurements conducted on the same day.
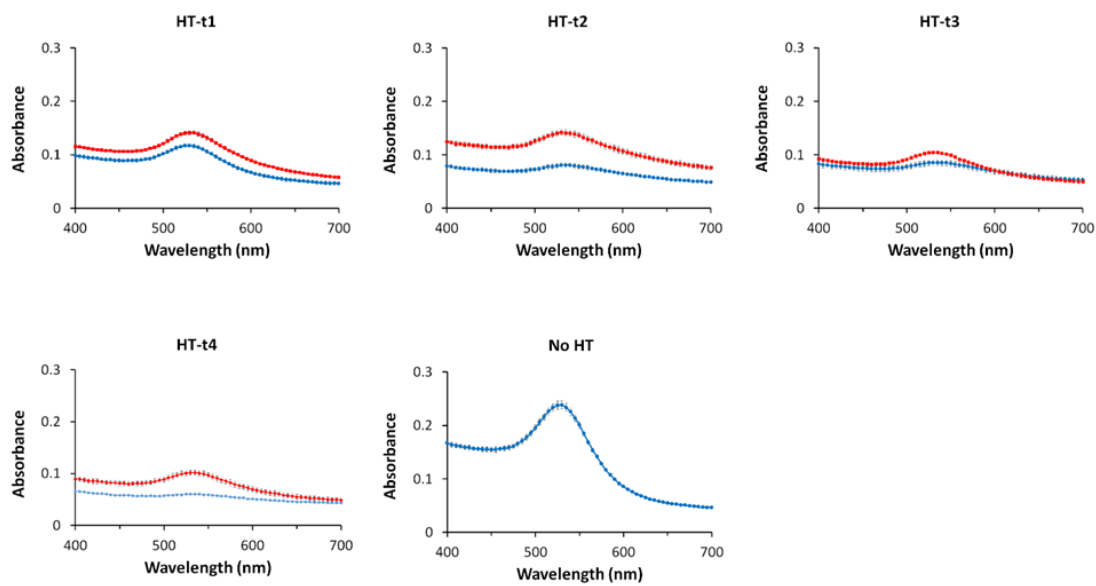
Figure 2.5. UV-Vis absorbance spectra data of Figure 2.4.B. The blue curves result from positive samples containing 20 nM DNA activator and the red curves result from negative samples without the activator. The negative control contained all reagents but no HT. After *trans*-cleavage for 10 min and addition of DNA-functionalized AuNPs, the samples were centrifuged for 10 s using a portable spinner. The supernatants were loaded onto a 96-well plate to record the UV-Vis spectra from 400 to 700 nm. Measurements from multiple independent experiments (n = 2) conducted on different days gave consistent results. Each curve in this figure represents the average of two measurements conducted on the same day.

Investigation of the no-toehold design

Since the leakage of the toehold greatly affected the performance of the CRISPR-Cas12a-mediated colorimetric assay, I further investigated the HT of no-toehold design in

which the DNA lock fully blocks the subdomain I. First, I determined the shortest length

of the crosslinker domain that led to sufficient aggregation of AuNPs (Figure 2.6). I mixed

100 nM of each crosslinker, 6+6 (L12), 7+7 (L14), 8+8 (L16), 9+9 (L18) and 10+10 (L20),

with 1 nM of two DNA-AuNPs. L12 was too short to result in the aggregation of AuNPs.

Although L14 could led to the aggregation, the intensity was lower than that resulting

from L16, L18, and L20. Thus, I used these three crosslinkers to design three HTs without

toehold, HT16, HT18, and HT20.
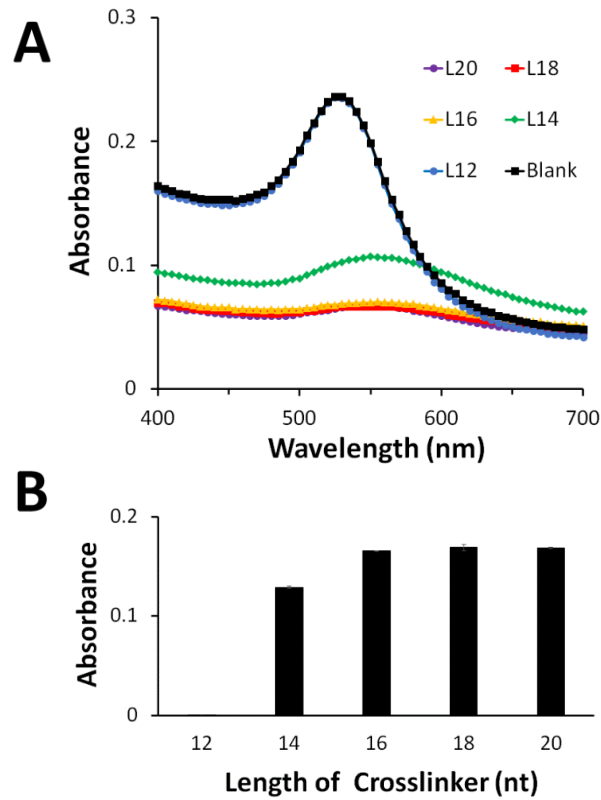
Figure 2.6. Determination of the shortest length of crosslinker for sufficient aggregation of AuNPs. (A) UV-Vis absorption spectra of samples containing 1 nM of each DNA-functionalized AuNP, 100 nM of crosslinker of different lengths, 800 mM NaCl, and 1x NEBuffer 2.1. After addition of the crosslinker, the solutions were centrifuged for 10 s in the spinner. The supernatants were loaded onto a 96-well plate to record the UV-Vis spectra from 400 to 700 nm. (B) The difference of absorbance between the samples and the blank at 530 nm. All samples were prepared in duplicate and each curve is the average of duplicate measurements. The error bars stand for the standard deviations of duplicates.

Figure 2.7 shows the performance of three HT of no-toehold: HT16, HT18, and HT20.

I successfully reduced the background by using these HTs. I observed the largest difference of absorbance between the negative control and positive sample when I used HT18. The removal of the toehold ensured the efficient blocking of the RNA crosslinker, leading to negligible background. An optimal length of 18 nt results in sufficient aggregation of AuNPs after the *trans*-cleavage of the DNA loop.
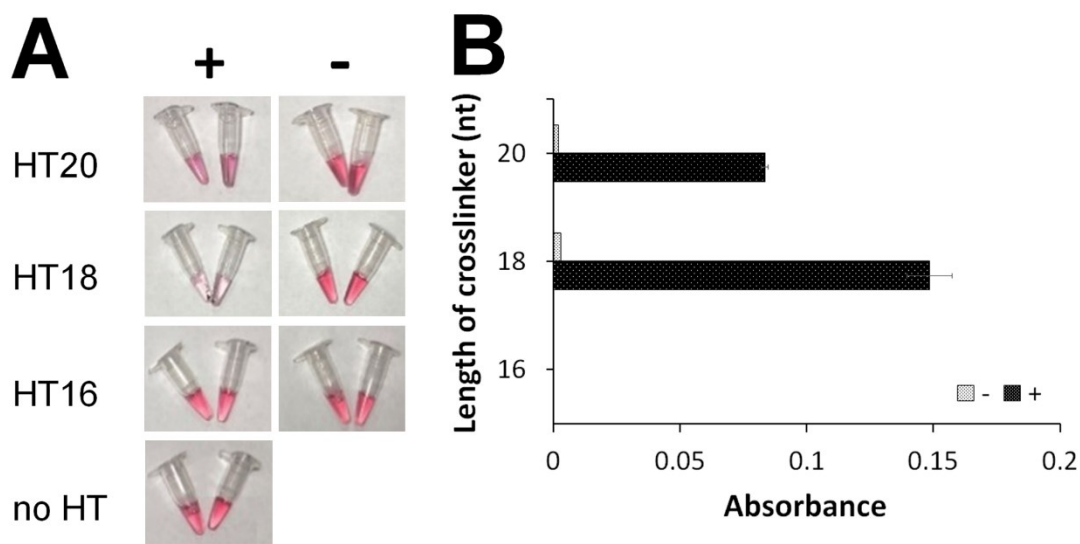
Figure 2.7. Comparison of hairpin transducers of different crosslinker lengths without a toehold by colorimetric assay (A) and UV-Vis absorbance (B). '+' indicates samples containing 20 nM model DNA sequence (DNA activator for Cas12a-gRNA). '-' indicates samples containing all reagents but no DNA activator. 'no HT' indicates negative control, containing all reagents except hairpin transducer. Measurements from multiple independent experiments (n = 2) conducted on different days gave consistent results. Each bar in this figure represents the average of two measurements conducted on the same day.
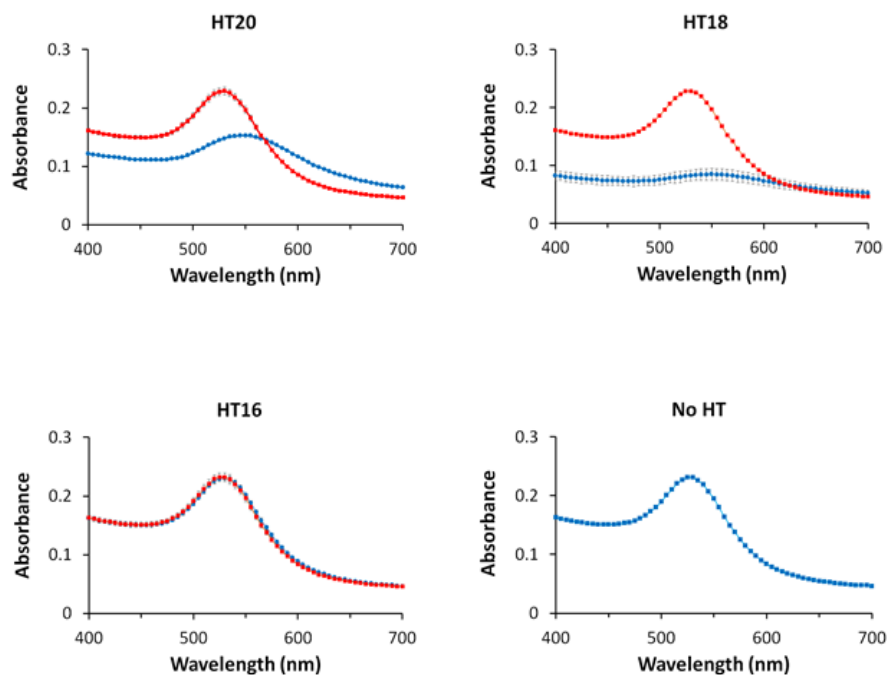
Figure 2.8. UV-Vis absorbance spectra data of Figure 2.7.B. The blue curves result from positive samples containing 20 nM DNA activator and the red curves result from negative samples without the activator. The negative control contained all reagents but no HT. After *trans*-cleavage for 10 min and addition of DNA-functionalized AuNPs, the samples were centrifuged for 10 s using a portable spinner. The supernatants were loaded onto a 96-well plate to record the UV-Vis spectra from 400 to 700 nm. Measurements from multiple independent experiments (n = 2) conducted on different days gave consistent results. Each curve in this figure represents the average of two measurements conducted on the same day.

Optimization of NaCl concentration

To achieve rapid aggregation of AuNPs, I optimized the concentration of Na^+ to

facilitate the assembly of DNA-functionalized AuNPs. As demonstrated in Figure 2.9.A, I prepared a series of solutions each containing 200 nM crosslinker L18, 1 nM of two types of DNA-AuNPs, and 0-1 M NaCl. Obviously, the increase in Na^+ concentration accelerated the aggregation and the color change could be observed in a shorter time. The difference of absorbance was shown as soon as 0.8 M NaCl was added (Figure 2.9.B). Without the crosslinker, the DNA-functionalized AuNP tolerated the high salt concentration and the color remained unchanged in the blank samples even after 20 min.
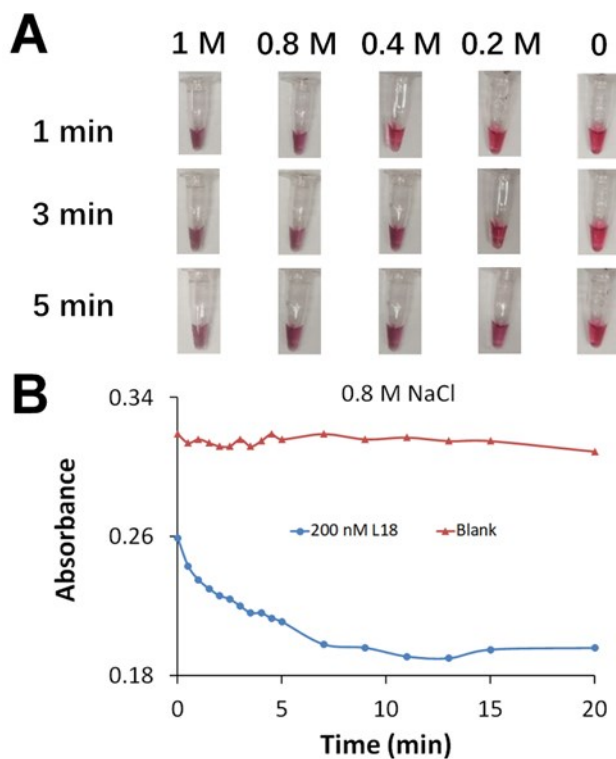
Figure 2.9. (A) Rapid aggregation of DNA-functionalized AuNPs assisted by the crosslinker sequence that was derived from the hairpin transducer. The samples contained 200 nM crosslinker L18, 1 nM each of two DNA-functionalized AuNPs, and different concentrations of NaCl. The photographs were taken at 1, 3, and 5 min after the addition of NaCl. (B) Absorbance measured at 530 nm for 20 min. Time 0 was when 0.8 M NaCl was added to the solution that contained 200 nM crosslinker L18 and 1 nM each of two DNA-functionalized AuNPs. All samples were prepared in duplicate and each curve is the average of duplicate measurements.

Enhancement of visual differentiation using centrifugation

Although I achieved the rapid color change in less than 1 min, the complete

59

aggregation and obvious color change needed about 10 min (Figure 2.9.B). I used a

portable spinner to centrifuge the reaction solutions for 10 s at 3000 rpm. Precipitation of

the AuNP aggregates significantly reduced the color of the solution to almost colorless in

the positive samples. However, the free AuNPs in the negative samples were not affected

by centrifugation and the solution remained as the red color. Figures 2.10A and 2.10B

demonstrate the improvement of the visual differentiation by spinning for 10 s. I observed

the color change only in the sample of 40 nM L18 when no centrifugation was applied.

Centrifugation for 10 s greatly improved the sensitivity of visual detection. The

precipitation of AuNP aggregates was observed for samples containing more than 10 nM

L18. The UV-Vis spectra detected only 20 nM of L18 before centrifugation but was able

to differentiate 2 nM of L18 from the blank after centrifugation (Figures 2.10C and 2.10D).

Note that the changes in absorbance values are much larger than the redshifts in

maximal absorption wavelength (λ_{max}) in response to low concentrations of the target.

Moreover, a 10-s spin of the reaction mixture enables rapid detection of the changes in

absorbance value and color intensity within 1 min. Therefore, detection based on the

reduction of absorbance value provides a lower limit of detection and faster analysis.
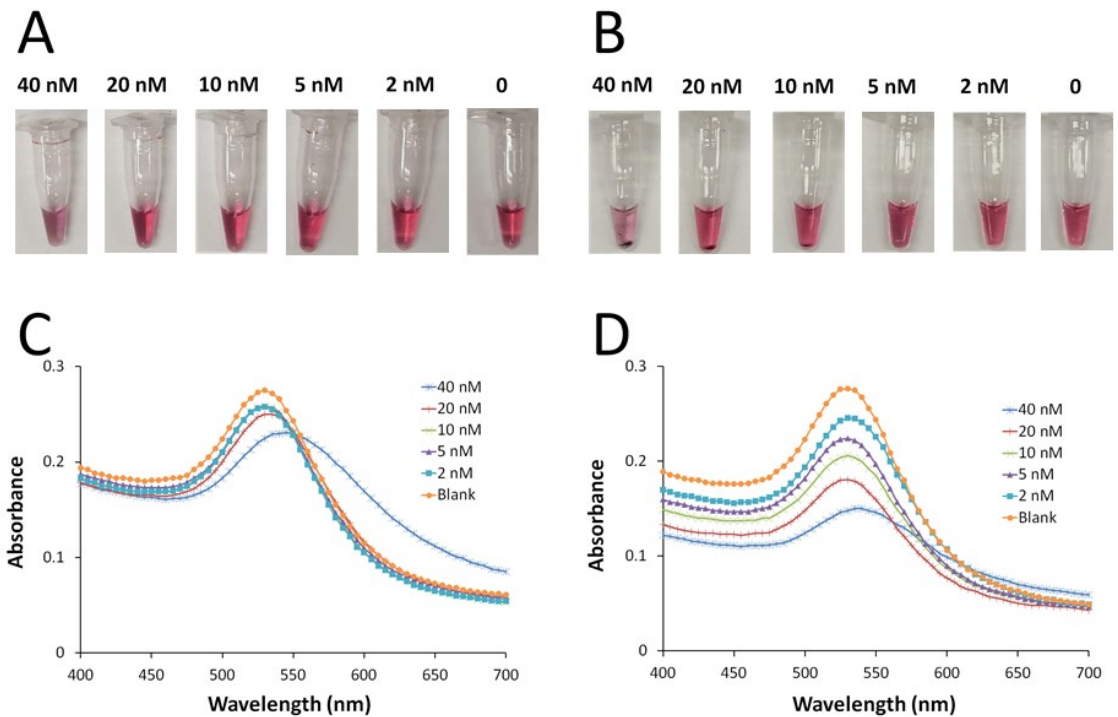
Figure 2.10. Improvement of the sensitivity by spinning AuNP aggregates at 3000 rpm for 10 s. (A) and (C) are the photos and UV-Vis spectra of AuNPs assembled by 0–40 nM L18 before centrifugation. (B) and (D) are the photos and UV-Vis spectra of AuNPs after centrifugation. All samples were prepared in duplicate and each curve is the average of duplicate measurements.

Detection of the viral RNA of the SARS-CoV-2

After the optimization of the colorimetric assay, I detected the N gene and E gene of the viral RNA. The E gene is highly conserved among different coronaviruses, including SARS-CoV, bat SARS-like coronavirus WIV1, and SARS-CoV-2. The N gene can be used to differentiate SARS-CoV-2 from other coronaviruses. I first used RT-LAMP to detect the N gene in varying amounts of the SARS-CoV-2 viral RNA, from 370 to

3,750,000 copies (Figure 2.11). Even the amplification of 370 copies of the target was completed in 30 min. Then, I used the CRISPR-Cas12a-mediated AuNP aggregation to test the RT-LAMP amplification products. As demonstrated in Figure 2.12, the triplicate blank samples that contained all the reagents except viral RNA remained as the red color, while the color of all other positive samples changed to nearly colorless after centrifugation. The pellets of AuNP aggregates were observed at the bottom of the test tube.
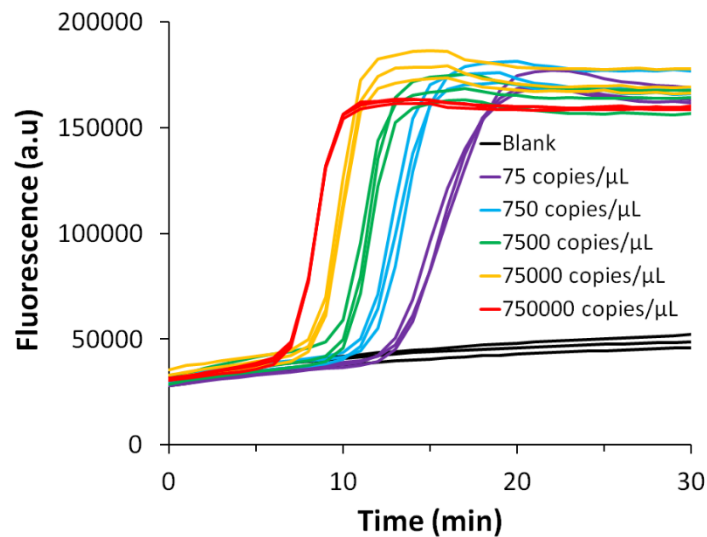
Figure 2.11. Real-time detection of SARS-CoV-2 viral N gene (75–750,000 copies/μL) using RT-LAMP. SYBR Green was used for probing amplification. Five microliters of the viral RNA sample were used for each reaction.
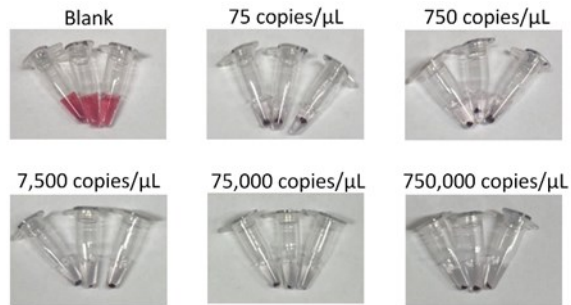
Figure 2.12. Representative images from triplicate analysis of samples containing varying concentrations of the SARS-CoV-2 viral RNA. The N gene was detected. Five microliters of the viral RNA sample were used. The tubes labelled blank contained all reagents but no RNA sample (negative control). Each tube is one of the triplicate samples.

I further determined the sensitivity of the assay by detecting both the N gene and the E gene in low amounts of the viral RNA. For the detection of both genes, I first monitored the RT-LAMP amplification of the viral RNA in real time, and then used CRISPR-Cas12a-mediated AuNP aggregation to generate a visual signal from the amplicons. All triplicate samples of 225, 300, and 375 copies of viral RNA showed positive results from RT-LAMP and the color change when I detected the N gene (Figure 2.13 and Figure 2.14). One of the samples of 75 copies also showed the color change. At 300 copies of the viral RNA, the E gene was reproducibly detected (Figure 2.15 and Figure 2.16), suggesting that the sensitivity of the colorimetric assay is governed by RT-LAMP. The developed assay of CRISPR-Cas12a-mediated AuNP aggregation maintained the sensitivity of RT-LAMP.
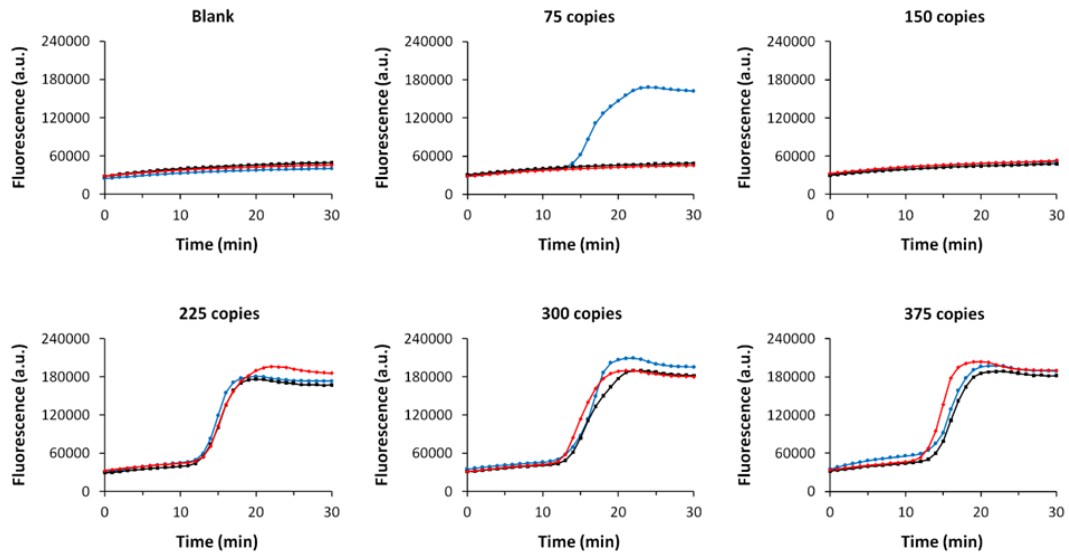
Figure 2.13. Real-time detection of the N gene of viral RNA at low copy numbers using RT-LAMP. Curves labeled in three different colors represent triplicate analysis.

Figure 2.14. Detection of the N gene at low copy numbers using the colorimetric method. Cas12a-gRNA RNP and hairpin transducer were added to the RT-LAMP samples of Figure 2.13 for 10 min *trans*-cleavage reaction. DNA-functionalized AuNPs were then added to induce the color change. Each tube corresponds to each curve in Figure 2.13.
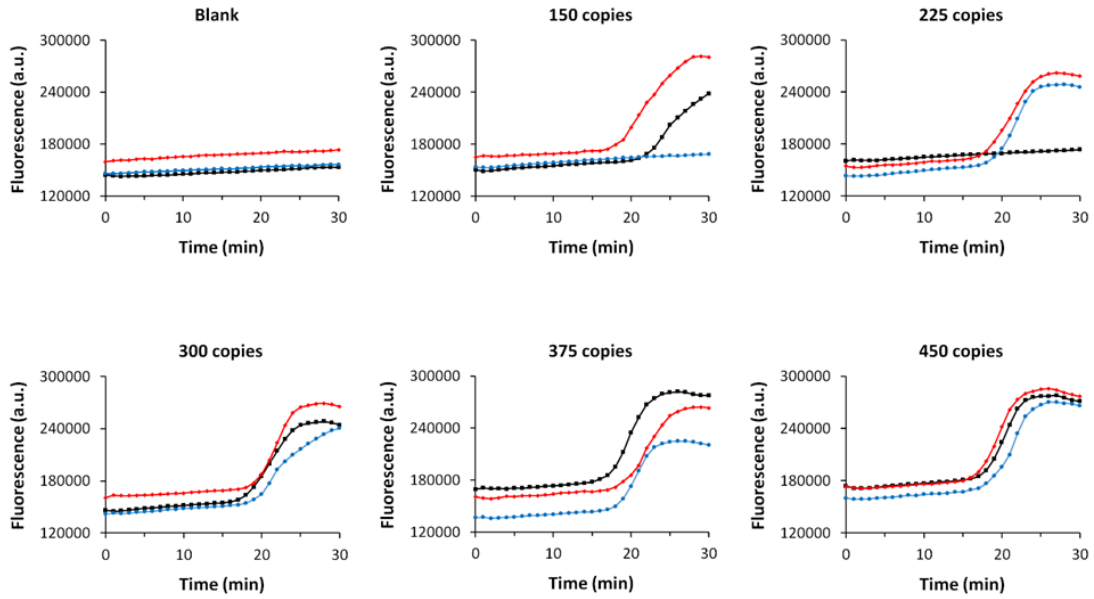
Figure 2.15. Real-time detection of the E gene at low copy numbers using RT-LAMP. Curves labeled in three different colors represent triplicate analysis.

Figure 2.16. Detection of the E gene at low copy numbers using the colorimetric method. Cas12a RNP and hairpin transducer were added to the RT-LAMP samples of Figure 2.15 for 10 min *trans*-cleavage reaction. DNA-functionalized AuNPs were then added to induce the color change. Each tube corresponds to each curve in the Figure 2.15.

Analysis of clinical samples

I used the developed colorimetric assay for the analysis of 54 clinical respiratory swab samples to demonstrate the feasibility of the assay for the diagnosis and screening of COVID-19 (Table 2.6). Twenty-seven of 54 clinical samples were positive as determined by RT-PCR. I successfully detected 25 positive samples but was not able to achieve positive results for two samples that required 35.4 and 37 threshold cycles (Table 2.5). Therefore, my assay had a clinical sensitivity of 92.6%. For all 27 RT-PCR negative samples, I obtained negative results and 100% clinical specificity. I achieved similar results for the detection of the E gene (Table 2.7).

Table 2.5. Summary of the analysis of SARS-CoV-2 N gene in 54 clinical samples.

	Positive samples	Negative samples
Positive results	25/27, 92.6%	0/27, 0%
Negative results	2/27, 7.4%	27/27, 100%

Table 2.6. Analysis of the N gene of SARS-CoV-2 in patient samples. Each set of tests contained a positive control, a negative control, and 4–6 samples. The positive control was 3750 copies of SARS-CoV-2 viral RNA and the negative control was nuclease-free water. Our collaborating public health laboratory also detected all the samples by using RT-PCR targeting the E gene of SARS-CoV-2. The results from RT-PCR are listed in the table.

Set of tests	Sample#	Ct value	Visualized detection
1st	Positive control	N/A	
	Negative control	N/A	
	#57	25.2	
	#59	25.2	
	#1	Negative	
	#2	Negative	
2nd	Positive control	N/A	
	Negative control	N/A	
	#72	20.1	

Set of tests	Sample#	Ct value	Visualized detection
	#90	26.4	
	#3	Negative	
	#12	Negative	
3rd	Positive control	N/A	
	Negative control	N/A	
	#106	23.5	
	#143	23.9	
	#151	Negative	
	#152	Negative	
4th	Positive control	N/A	
	Negative control	N/A	
	#125	31.1	
	#134	30.2	

Set of tests	Sample#	Ct value	Visualized detection
	#137	32.6	
	#159	Negative	
	#160	Negative	
	#161	Negative	
5th	Positive control	N/A	
	Negative control	N/A	
	#123	24.3	
	#144	24.9	
	#148	24.3	
	#162	Negative	
	#163	Negative	
	#164	Negative	
6th	Positive control	N/A	

Set of tests	Sample#	Ct value	Visualized detection
	Negative control	N/A	
	#110	25.8	
	#122	24.9	
	#132	25.7	
	#165	Negative	
	#166	Negative	
	#167	Negative	
7th	Positive control	N/A	
	Negative control	N/A	
	#107	27.6	
	#114	27.4	
	#146	27.6	
	#168	Negative	

Set of tests	Sample#	Ct value	Visualized detection
	#169	Negative	
	#170	Negative	
8th	Positive control	N/A	
	Negative control	N/A	
	#103	26.6	
	#124	26.7	
	#150	26.4	
	#171	Negative	
	#172	Negative	
	#173	Negative	
9th	Positive control	N/A	
	Negative control	N/A	
	#115	32.6	

Set of tests	Sample#	Ct value	Visualized detection
	#127	31.7	
	#129	28.2	
	#174	Negative	
	#175	Negative	
	#176	Negative	
10th	Positive control	N/A	
	Negative control	N/A	
	#126	35.4	
	#130	37.0	
	#145	25.3	
	#177	Negative	
	#178	Negative	
	#179	Negative	

Table 2.7. Analysis of the E gene of SARS-CoV-2 in patient samples. Each set of tests contained a positive control, a negative control, and four samples. The positive and negative controls were the same as noted in Table 2.6.

Set of tests	Sample#	Ct alue	Visualized detection
1st	Positive control	N/A	
	Negative control	N/A	
	#57	25.2	
	#59	25.2	
	#1	Negative	
	#2	Negative	
2nd	Positive control	N/A	
	Negative control	N/A	
	#72	20.1	
2nd	#90	26.4	

Set of tests	Sample#	Ct alue	Visualized detection
	#3	Negative	
	#12	Negative	

2.4 Conclusion

I incorporated the isothermal amplification technique RT-LAMP with the *trans*-cleavage activity of CRISPR-Cas12a to develop a colorimetric assay for the detection of SARS-CoV-2. The designed hairpin transducer can be cleaved by the activated CRISPR-Cas12a and release the RNA crosslinker to induce the aggregation of AuNP. I successfully applied the assay to the visual detection of two genes of SARS-CoV-2 viral RNA. The detection can be completed within 45 min at a single controlled temperature of 62 °C. The naked-eye observation of the detection results eliminates the need for sophisticated equipment, which makes the assay ideal for POC diagnosis of COVID-19. I can use this assay for the detection of other pathogens by adjusting the primers of RT-LAMP and the gRNA of the CRISPR-Cas12a.

Chapter 3 SDA-DNAzyme circuit for the detection of nucleic acids

3.1 Introduction

Similar to CRISPR-Cas systems, RNA-cleaving DNAzymes can catalyze the cleavage reaction and the activation of DNAzymes relies on specific DNA hybridization.[57] Instead of indiscriminately cleaving the substrate, DNAzymes are designed to cleave specific sites. Moreover, DNAzymes have higher stability, lower cost of production, and can be functionalized easily.[51] Taking advantage of these merits and the controllable cleavage activity of DNAzymes, researchers have established different DNA architectures, including DNA logical gates,[98-103] DNA nanomachines,[104-107] and DNAzyme circuits.[52-54]

The DNAzyme circuit is a strategy of using DNAzyme to improve the existing isothermal amplification techniques for the detection of nucleic acids. Generally, the cleavage reaction and the isothermal amplification reaction form the positive feedback circuit so that both reactions are accelerated to enhance the sensitivity. For example, RCA technique was used to amplify the target and generate multiple DNAzymes, which cleaved the blocker on the template of RCA and triggered more RCA reactions.[53] The initiation of new RCA increases the amount of DNAzymes in the circuit, thus accelerating the amplification to form the positive feedback. Another strategy used the CHA technique to amplify the DNAzymes that cleaved the substrates and generated more catalytic DNAs for the CHA amplification.[52] Although the sensitivity of these circuits has been improved

by the DNAzyme, using them to detect different targets requires the alteration of the circular template of RCA or the hairpins of CHA. Since the preparation of the RCA template is time-consuming and the CHA hairpins need to be carefully designed to avoid nonspecific assembly, the reported circuits are not ideal for the detection of various nucleic acids.

Herein, I developed the SDA-DNAzyme circuit to detect different nucleic acid targets without changing the sequence design of the circuit system by using MNAzyme for target recognition. The initiation of the circuit required the specific hybridization of two binding arms of the MNAzyme subunits to the target. The detection of two model targets was performed in a one-pot format at a constant temperature of 37 °C. To detect another target, I need to change only the sequences of the two binding arms but not of the circuit.

3.2 Materials and methods

Reagents

All nucleic acids were synthesized by Integrated DNA Technologies (IDT; Coralville, IA, USA) and diluted by 1x IDTE buffer (10 mM Tris, 0.1 EDTA, pH=8.0). Magnesium chloride ($MgCl_2$) and manganese chloride ($MnCl_2$) were obtained from Sigma (Oakville, ON, Canada). Tris-HCl buffer (pH=7.4) was purchased from Sigma-Aldrich (St. Louis, MO, USA). Other reagents, including Klenow Fragment ($3'{\to}5'$ exo$^-$) polymerase, Nt.AlwI restriction endonuclease, T4 Polynucleotide Kinase, NEBuffer 2, and dNTP were

purchased from New England BioLabs (NEB; Whitby, ON, Canada).

Investigation of different blockers for the template of SDA

Table 3.1 lists the sequences of templates and blockers of different designs. For comparison of the cleavage activity of the blockers, each sample contained 1 μM of different blockers (B_{a-b} or B_c), 100 nM molecular beacon substrate, 0.5 mM $MnCl_2$, and 1x NEBuffer 2. Duplicate samples were loaded onto the 96-well plate and 60-min cleavage reactions of the substrate were monitored by Multi-Mode Microplate Reader FilterMax F5 from Molecular Devices (Sunnyvale, CA, USA). The fluorescence signal generated from the cleavage of substrate was measured and recorded at excitation/emission of 485/535 nm every 3 min.

Table 3.1. The sequences of the blockers (B_{a-b} and B_c), template (T_a), molecular beacon substrate (MBS), and DNAzyme. For B_{a-b}, B_c and DNAzyme, the red sequence is the catalytic core that processes the cleavage activity. The blue and green sequences (a and b) of B_{a-b} are the two arms that can hybridize with the substrate. The yellow sequence of B_c can block the recognition region of the template in the same color. 'InvdT' is the *inverted dT* modification on the 3'-end. For the template, the underlined sequence can be blocked by B_{a-b} and the shaded sequence can be blocked by B_c. The sequence in bold is the primer binding region. The sequences of MBS in italics are complementary to each other. 'FAM' and 'IABkFQ' are the fluorophore and quencher groups that labeled on 5'-end and 3'-end, respectively.

Name		Sequence (5' → 3')
B_{a-b}	B_{4-3}	C AGA GGC TAG CTA CAA CGA GGT /InvdT/
	B_{3-4}	AGA GGC TAG CTA CAA CGA GGT C /InvdT/
	B_{2-5}	GA GGC TAG CTA CAA CGA GGT CC /InvdT/
	B_{2-4}	GA GGC TAG CTA CAA CGA GGT C /InvdT/
	B_{3-3}	AGA GGC TAG CTA CAA CGA GGT /InvdT/
	B_{2-2}	GA GGC TAG CTA CAA CGA GG /InvdT/
B_c	B_{15}	G ATC AAA A CA GTC AGA GGC TAG CTA CAA CGA /InvdT/
	B_{14}	G ATC AAA A CA GTC AGA GGC TAG CTA CAA CG

78

Name		Sequence (5' → 3')
		/InvdT/
	B_{13}	G ATC AAA A CA GTC AGA GGC TAG CTA CAA C /InvdT/
T_a	T_9	GGA CC TCG TTG TAG CTA GCC TCT GAC TG TTT TGA TCC **CGG TCC ATG** /InvdT/
	T_{10}	GGA CC TCG TTG TAG CTA GCC TCT GAC TG TTT TGA TCC **CGG TCC ATG T**/InvdT/
	T_{11}	GGA CC TCG TTG TAG CTA GCC TCT GAC TG TTT TGA TCC **CGG TCC ATG TG**/InvdT/
	T_{12}	GGA CC TCG TTG TAG CTA GCC TCT GAC TG TTT TGA TCC **CGG TCC ATG TGA**/InvdT/
MBS		/FAM/*CCC AAG GG* TTT TTT **TCA CAT GGA CCrG** rUCT GAC TGT TTT TTT T *CCC TTG GG* /IABkFQ/
DNAzyme		GTC AGA GGC TAG CTA CAA CGA GGT CC

For comparison of the blocking efficiency of the blockers, each sample contained 1 nM DNAzyme, 100 nM substrate, 50 nM template-blocker complex (ratio 1:2), 0.5 mM MnCl$_2$, and 1x NEBuffer 2. I prepared the template-blocker complex by annealing the solution containing 1 μM template and 2 μM blocker in the annealing buffer (10 mM Tris-HCl buffer and 10 mM MgCl$_2$). The solution was heated to 80 °C and then cooled down

to 20 °C gradually in 1 h by an MJ Mini Personal Thermal Cycler (Bio-Rad). The cleavage reaction of the substrate was measured and recorded at the same conditions as noted above.

Optimization of the SDA-DNAzyme circuit

I used 50 pM DNAzyme as the target to optimize the conditions of the SDA-DNAzyme circuit, including the length of template and the concentrations of template-blocker complex, MBS, and polymerase. A standard SDA-DNAzyme circuit reaction contained 25 nM T_9B_{13} (Table 3.1) template-blocker complex, 200 nM MBS, 0.04 U/μL Klenow Fragment (3'→5' exo$^-$) polymerase, 0.08 U/μL Nt.AlwI restriction endonuclease, 0.08 U/μL T4 polynucleotide kinase, 100 mM dNTP, 0.05 mM $MnCl_2$, and 1x NEBuffer 2. To optimize each parameter, I changed the corresponding reagent or its concentration. The SDA-DNAzyme circuit reaction was monitored and recorded for 3 h. Other measurement conditions were the same as noted above.

Detection of model targets

Table 3.2 lists the sequences of two model targets, Mal and HBV, and two pairs of subunits. To prepare the MNAzymes, I mixed 2 μM of subunits MzM-L and MzM-R (or MzH-L and MzH-R) with different concentrations of Mal (100 nM, 10 nM, 1 nM, 100 pM, and 10 pM, or HBV at the same concentrations) in the annealing buffer. The mixture was heated to 80 °C and then cooled down to 20 °C gradually in 1 h. Then, all mixtures were diluted 100 times and 5 μL of diluted mixture was added to 95 μL of standard SDA-DNAzyme circuit reaction solution. The SDA-DNAzyme circuit reaction was monitored and recorded for 3 h. Other measurement conditions were the same as mentioned above.

Table 3.2. The sequences of MNAzyme subunits and nucleic acid targets. 'Mal' and 'HBV' are two model targets. 'MzM-L/R' and 'MzH-L/R' are two pairs of subunits that can recognize 'Mal' and 'HBV' respectively. The sequences in red are partial catalytic core of subunits. The sequences of subunits in bold and italics can bind with the target regions with the same labels. The sequences in blue and green are binding arms that can hybridize with the molecular beacon substrate.

Name	Sequence (5' → 3')
MzM-L	AG TCA GA GGC TAG CT **CGT CTG TTA TGA ACA CTT AAT TTT** /InvdT/
MzM-R	*ACA ATG AAC TCA ATC ATG ACT ACC* A CAA CGA GGT CCA /InvdT/
Mal	**AAA ATT AAG TGT TCA TAA CAG ACG** *GGT AGT CAT GAT TGA GTT CAT TGT*
MzH-L	AG TCA GA GGC TAG CT **GGA CTG CGA ATT TTG GC** /InvdT/
MzH-R	*GAG TGA TTG GAG GTT GG* A CAA CGA GGT CCA /InvdT/
HBV	**GCC AAA ATT CGC AGT CC***C CAA CCT CCA ATC ACT C*

3.3 Results and discussion

Principle of SDA-DNAzyme circuit

To detect the nucleic acid targets, I designed two subunits, each containing a sensor arm complementary to the target (Figure 3.1A). Target recognition assembles the two subunits and leads to the formation of MNAzyme with an intact catalytic core. I also designed MBS that has two functions: (1) serving as the substrate of the MNAzyme to report the cleavage reaction, (2) releasing the primer to initiate the SDA-DNAzyme circuit (Figure 3.1B). The MBS was dually labeled with fluorophore and quencher groups on each end. The cleavage of the loop by MNAzymes destabilized the hairpin structure of MBS and separated the two groups, generating the fluorescence signal. One of the cleavage products was designed to be complementary to the template. As a result, the presence of the nucleic acid target results in an observable signal and the liberation of the primer to trigger the circuit.

Figure 3.1C demonstrates the positive feedback amplification of the SDA-DNAzyme circuit. The polymerase extends the primer to generate a copy of the DNAzyme. The endonuclease then nicks the extension product to generate a new 3'-end. The polymerase with strand displacement activity can repeatedly extend the new 3'-end and displace the downstream DNAzyme, which is released to cleave the MSB and produce more primers. More SDA reactions are initiated to accelerate the amplification of the DNAzyme. Thus, the SDA reaction and the DNAzyme cleavage reaction develop a feedback amplification circuit that can sensitively respond to the nucleic acid target.
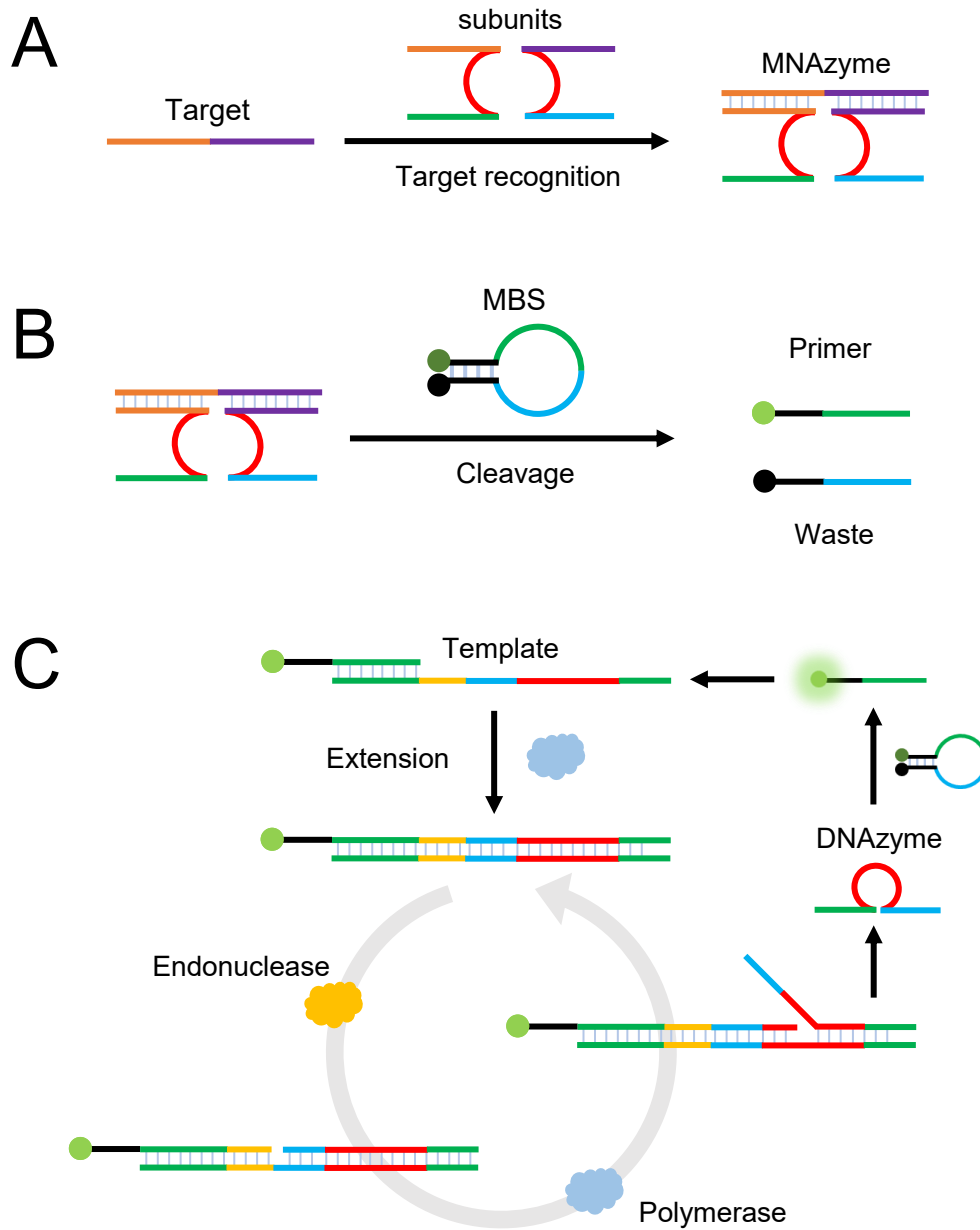
Figure 3.1. The principle of the SDA-DNAzyme circuit. (A) Two subunits hybridize with the target to form the MNAzyme. (B) MNAzyme cleaves MBS to release the primer. (C) Primer initiates the SDA reaction and develops a positive feedback amplification between the SDA and DNAzyme.

Functional domains of each component in the circuit

Figure 3.2A shows five components in the circuit: the nucleic acid target, two subunits, the MBS, the template, and the DNAzyme. The subunit consists of a sensor arm I or II complementary to the target domain I* or II*, a partial catalytic core C_1 or C_2, and a binding arm A or B. Serving as the substrate of MNAzyme, MBS contains two substrate domains A* and B*. After the cleavage of MBS, domain A* is released to hybridize with the primer-binding domain A of the template. The template also contains an endonuclease recognition domain D and the DNAzyme generation domain $(B*+C_2*+C_1*+A*)$. The extension of primer A* generates a copy of the DNAzyme $(A+C_1+C_2+B)$ that can also hybridize with the substrate domains A* and B* of the MBS to catalyze its cleavage.

I analyzed the potential risk of the circuit being interrupted. The domains $A+C_1$ and $B+C_2$ of two subunits prefer to hybridize with the DNAzyme generation domain $(B*+C_2*+C_1*+A*)$ of the template with longer complementary sequences (Figure 3.2B). Therefore, the MNAzymes cannot cleave the MBS and the circuit cannot be initiated. It is necessary to design anther component that blocks the DNAzyme generation domain to prevent the subunits from binding to the template.
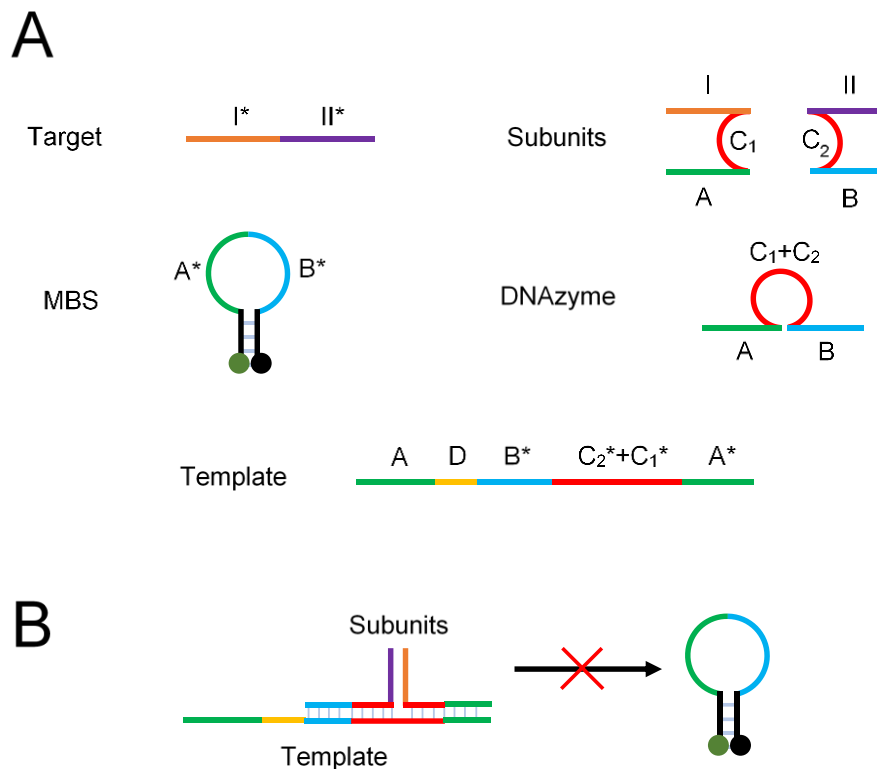
Figure 3.2. Sequence design of the SDA-DNAzyme circuit. (A) Functional domains of each component in the circuit. '*' indicates the complementary sequence. (B) When there is no blocker, the subunits of MNAzyme prefer to bind to the template but not the MBS. The cleavage activity is silenced.

Designs of the blocker

The design of a blocker for the SDA-DNAzyme circuit has two major aims: (i) prevent the subunits from hybridizing with the DNAzyme generation domain of the template; (ii) eliminate the cleavage activity of the blocker to avoid background. Since the blocker is complementary to the DNAzyme generation domain, it has the same sequence as the DNAzyme and may process the cleavage activity. Even low cleavage

activity of the blocker can be amplified by the circuit to generate high background, thus significantly reducing the sensitivity of the system. As demonstrated in Figure 3.3, I proposed and compared two designs of the blocker to fulfill these two goals. I designed blocker $B_{a\text{-}b}$ with different lengths of domains A and B to achieve good blocking efficiency (Table 3.1). I also designed blocker B_c with different lengths of domain C to eliminate the catalytic activity.
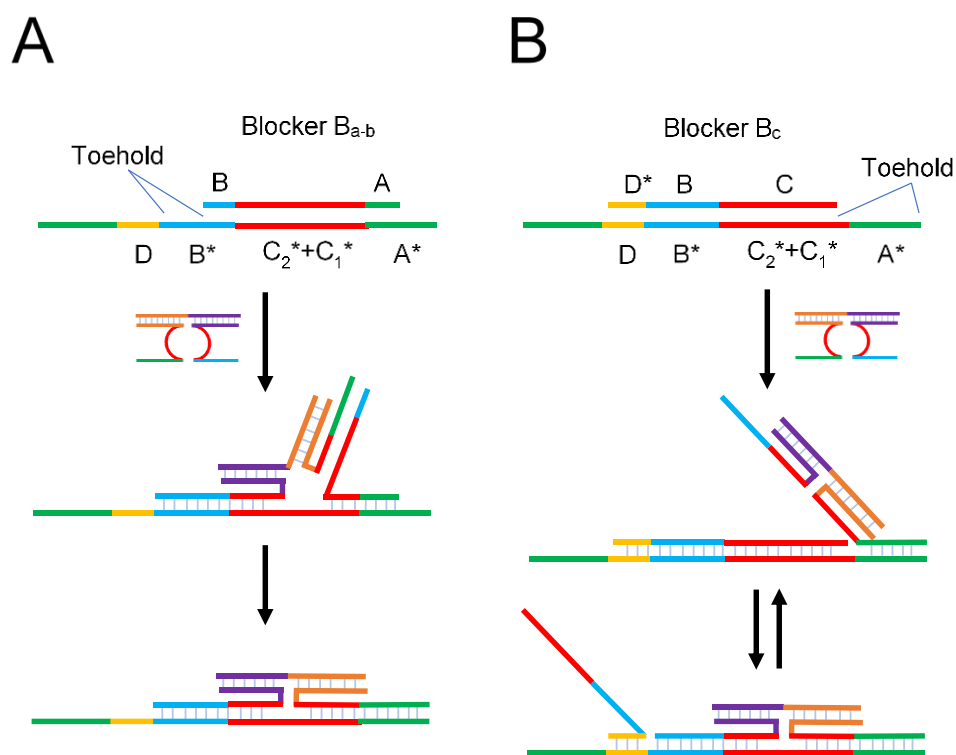
Figure 3.3. Designs of two blockers and their displacement reactions. (A) Blocker B_{a-b} uses the design of the toehold-mediated strand displacement reaction. 'a' and 'b' stand for the lengths of the domains 'A' and 'B'. (B) Blocker B_c uses the design of the toehold-mediated strand exchange reaction. 'c' represents the length of the domain 'C'.

Figure 3.3A shows the first design of blocker B_{a-b}, which is advantageous for blocking the DNAzyme generation domain. B_{a-b} fully blocks the C_1*+C_2* domain and partially blocks the A* and B* domains of the template. B_{a-b} may still have the cleavage activity because it has both binding arms. However, the existence of domain A ensures the short toehold to improve the blocking efficiency. The displacement of the blocker by the MNAzymes is the reaction of toehold-mediated strand displacement. The binding arms A

and B of the MNAzymes can first hybridize with the exposed toehold (B*-B or A*-A). Then, it gradually displaces the blocker and completely hybridizes with the template. The kinetics of the displacement depends on the length of the toehold. As long as the toehold is shorter than 5 nt, the blocker can efficiently block the template due to the slow displacement.

To completely eliminate the cleavage activity of the blocker, I also designed the blocker B_c that has only one binding arm B (Figure 3.3B). Removing domain A can significantly reduce the stability of hybridization between B_c and MBS, thus silencing the cleavage activity of the blocker. In addition, I can use a shorter C domain to deactivate the catalytic core of the blocker. However, this design had a long toehold ($A*+ C_1*+C_2*-C$) > 5 nt for rapid strand displacement. Therefore, it is necessary to block the D domain to design a toehold-mediated strand exchange reaction for blocking the template. After the MNAzymes bind to the toehold and displace B_c, domain D can work as the second toehold and the blocker can displace the MNAzymes. The reversible reaction is able to prevent B_c from being completely displaced. A longer D* of B_c is better for high blocking efficiency. Nevertheless, endonuclease can recognize the duplex of D*D and nick domain D* if they are fully complementary to each other. Thus, I designed domain D* of B_c to be 1 nt shorter than domain D.

Investigation of the blocker B_{a-b}

Since blocker B_{a-b} contains both binding arms, I first tested the cleavage activity of B_{a-b} with different lengths of domains A and B. Figure 3.4A shows the reaction of B_{a-b}

cleaving MBS. Using a high concentration of 1 μM blocker, I was able to monitor the low cleavage activity. Among the five B_{a-b} blockers, B_{4-3}, B_{3-4}, and B_{2-5} showed cleavage activity but B_{2-4} and B_{3-3} had no observable signal within 1 h. These results suggested that B_{a-b} with longer A and B domains can hybridize with MBS more stably to catalyze the cleavage reaction. Therefore, only the B_{a-b} blocker shorter than B_{2-4} and B_{3-3} can be used to construct the SDA-DNAzyme circuit with low background.

I further compared the blocking efficiency of B_{2-4}, B_{3-3}, and B_{2-2} using 1 nM DNAzyme to cleave MBS. The complex of B_{2-2} and template had a long toehold of 6 nt, which might lead to a rapid toehold-mediated strand displacement reaction. As expected, 100 nM B_{2-2} could hardly block 50 nM template (Figure 3.4B) and the 1 nM DNAzyme stopped cleaving MBS to generate the fluorescence signal after 15 min. B_{3-3} and B_{2-4} displayed good blocking efficiency and DNAzyme kept cleaving the MBS within 1 h. Their hybridization with the template formed toeholds shorter than 5 nt so that the displacement of the blockers was relatively slow.

Thus, I tried to construct the SDA-DNAzyme circuit by using the blockers B_{2-4} and B_{3-3}. The samples containing B_{2-4} and B_{3-3} but no DNAzyme or MNAzymes showed the exponential amplification signal (Figure 3.5). Both circuits generated high background even though I did not observe the cleavage activity of 1 μM blocker in 1 h. Without the blockers, the blank sample did not show any increase in fluorescence. The circuit was capable of amplifying the cleavage activity of B_{a-b} that was not detectable in the cleavage reaction. Therefore, it was difficult to apply the B_{a-b} to the circuit because I would have

the issue of either low blocking efficiency from the short B_{a-b} or high background from the long B_{a-b}.
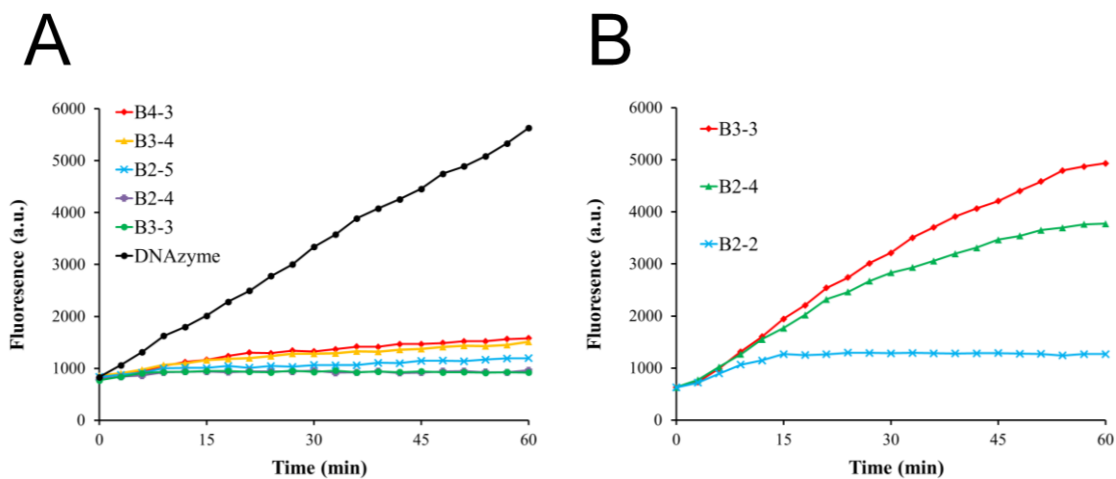
Figure 3.4. Comparison of the blocker B_{a-b} of different lengths. 'a' and 'b' are the lengths of the two binding arms of the blocker that block the domains A* and B* of the template, respectively. All samples were prepared in duplicate and each curve is the average of two measurements. (A) Determination of the cleavage activity of B_{a-b}. In each sample, 1 μM B_{a-b} cleaved 100 nM MBS. The positive control was 1 nM DNAzyme. (B) The blocking efficiency of three blockers that had no observable cleavage activity. In each sample, 1 nM DNAzyme cleaved 100 nM MBS in the solution containing 50 nM template T_{10} and 100 nM blocker. Measurements from multiple independent experiments (n = 2) conducted on different days gave consistent results. Each curve in this figure represents the average of two measurements conducted on the same day.
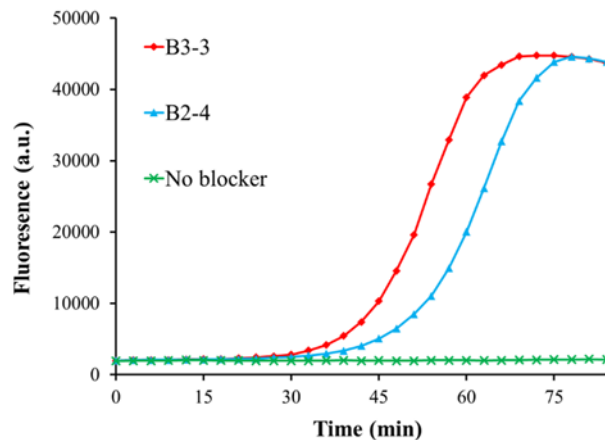
Figure 3.5. Blockers $B_{3\text{-}3}$ and $B_{2\text{-}4}$ generated high background in the SDA-DNAzyme circuit. Each reaction contained 200 nM MBS, 0.04 U/μL Klenow Fragment (3'→5' exo-) polymerase, 0.08 U/μL Nt.AlwI endonuclease, 0.08 U/μL T4 polynucleotide kinase, 100 mM dNTP, 0.5 mM Mn^{2+}, 50 nM template T_{10}, and 100 nM blocker $B_{a\text{-}b}$ in 1x NEBuffer 2. The blank sample contained all reagents except the blocker. Measurements from multiple independent experiments (n = 3) conducted on different days gave consistent results. Each curve in this figure represents the average of two measurements conducted on the same day.

Investigation of the blocker B_c

To eliminate the high background, I aimed to reduce the cleavage activity of the blocker by removing the binding arm domain A. I also deleted 1-2 nt of the catalytic core domain C to further silence the cleavage activity. Figure 3.6A demonstrates the comparison of the cleavage activity of B_{15}, B_{14}, and B_{13} (Table 3.1). The 1 μM B_{15} showed a high cleavage rate even though it only had the binding arm domain B. The removal of

91

the nucleotide in the catalytic core domain significantly decreased the activity of B_c. Compared to B_{15}, B_{14} could only cleave 1/3 of MBS in 1 h. The sample of B_{13} showed no increase in the fluorescence signal, indicating that the deletion of 2 nt led to the silence of its activity. To confirm this result, I also tested B_{13} in the SDA-DNAzyme circuit and could not observe the background in the blank sample with no target DNAzyme (data not shown).

Theoretically, B_{13} could efficiently block the template. After I removed 2 nt from the catalytic core domain, the length of the toehold for MNAzyme is $A^*+(C_2^*+C_1^*)-(C_1+C_2)$ $=5+15-13=7$ nt. The displacement of B_{13} by the MNAzyme forms a new toehold D, which has a longer length of 8 nt. Therefore, the displacement of MNAzymes by B_{13} is more favorable so that B_{13} can remain hybridizing with the template (Figure 3.6B) during the reversible toehold-mediated strand exchange reaction. As shown in Figure 3.6B, DNAzyme could not cleave MBS when there was no B_{13} but only template. In the sample containing 100 nM B_{13} to block 50 nM template, 1 nM DNAzyme continuously cleaved the MBS to generate high fluorescence signal in 1 h. Due to the good blocking efficiency and no cleavage activity, I used B_{13} to construct the SDA-DNAzyme circuit for the detection of the nucleic acid targets.
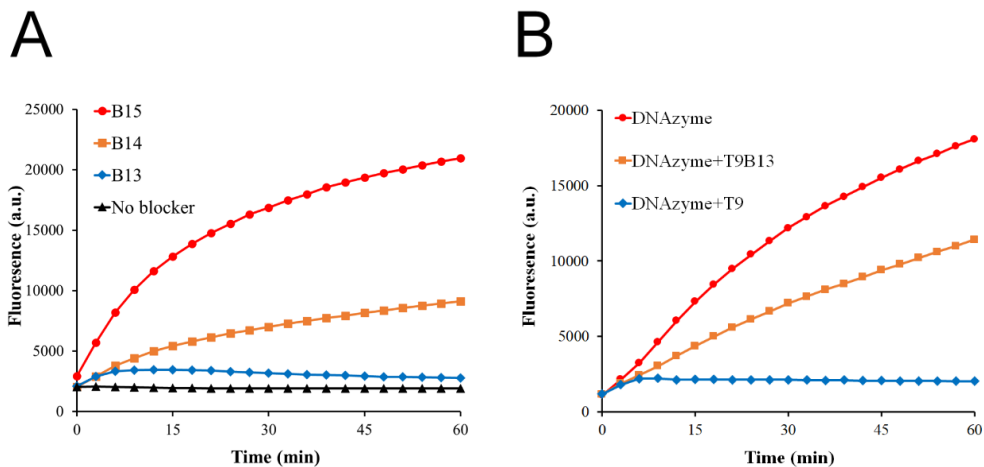
Figure 3.6. Comparison of the blocker B_c of different lengths. 'c' indicates the length of the C domain of the blocker (Figure 3.6.B). All samples were prepared in duplicate and each curve is the average of two measurements. (A) Determination of the cleavage activity of B_c. In each sample, 1 μM B_c cleaved 100 nM MBS in 1 h. (B) Investigation of the blocking efficiency of the B_{13}. All samples contained 1 nM DNAzyme to cleave 100 nM MBS. 'T_9B_{13}' means the sample also had 50 nM template T_9 (Table 3.1) and 100 nM blocker B_{13}. 'T9' indicates the sample contained T_9 but no B_{13}. Each curve represents the average of duplicate analyses.

Comparison of different lengths of primer binding domain of template

The length of the primer binding domain A of the template is critical to the performance of the SDA-DNAzyme circuit (Figure 3.2A). If the primer binding domain is too short, it cannot stably hybridize with the primer to initiate the SDA amplification. However, a long primer binding domain A can hybridize with the A* domain of MBS before the cleavage. At the beginning of the reaction, the nucleic acid target at low

concentration can form only a small amount of MNAzyme, leading to the slow cleavage of MBS. Therefore, the concentration of the primer at fM–pM levels is much lower than that of MBS at nM levels. Since uncleaved MBS is more competitive than the primer released from the cleavage reaction to occupy the primer binding domain, the primer can hardly trigger the circuit to amplify the signal. Thus, I designed four templates, T_9, T_{10}, T_{11}, and T_{12}, to compare different lengths of the primer binding domain varying from 9 to 12 nt (Table 3.1). The melting temperatures (T_m) of the primer hybridizing with the four templates are: 32.8, 38.3, 42.8, and 46.4 °C. T_9 has a T_m lower than the reaction temperature of 37 °C. The high T_m of T_{11} and T_{12} may enable them to bind to the uncleaved MBS.

I used the SDA-DNAzyme circuit to test these four templates (Figure 3.7). As expected, the circuit of T_{11} had a low fluorescence signal. Increasing the length to 12 nt further decreased the signal, while reducing the length to 10 nt dramatically improved the amplification. These results indicated that the hybridization between the long primer binding domain and uncleaved MBS led to the slow amplification. However, a high background was generated in the circuit of T_{10}. I attribute this background to the initiation of the circuit by the impurities in MBS. Although there was no cleavage of MBS in the blank sample, low abundance impurities of digested MBS can still work as a primer to hybridize with T_{10} because of its high T_m. In the circuit of T_9, there was no obvious increase in the background, suggesting that the impurities were not able to bind to the template due to its low T_m. Only the accumulation of the cleaved MBS could increase the

concentration of the primer to trigger the circuit and amplify the signal. Therefore, I selected T_9 as the template for the construction of the SDA-DNAzyme circuit because of its low background and good amplification.
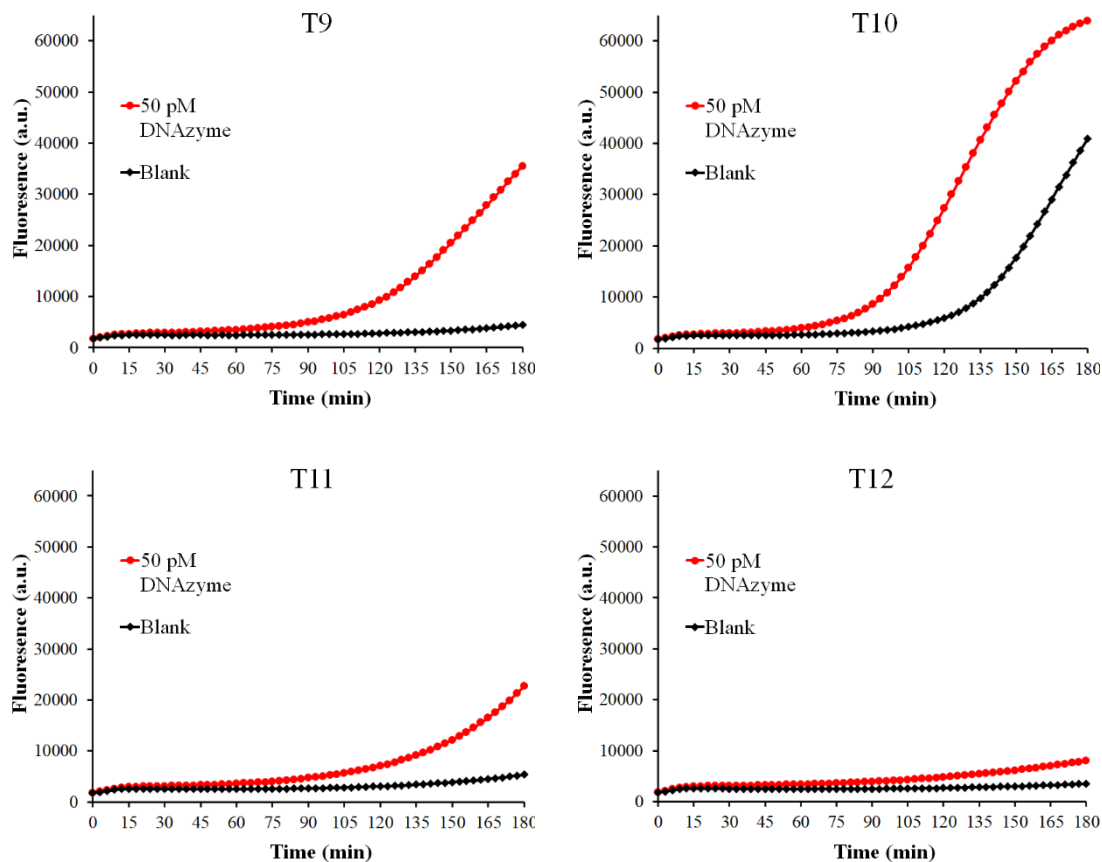
Figure 3.7. Comparison of different lengths of the primer binding domain A of the template using the SDA-DNAzyme circuit. 'T9' indicates the template had a primer binding domain of 9 nt. Each reaction contained 200 nM molecular beacon substrate, 0.04 U/µL Klenow Fragment (3'→5' exo-) polymerase, 0.08 U/µL Nt.AlwI endonuclease, 0.08 U/µL T4 polynucleotide kinase, 100 mM dNTP, 0.5 mM Mn^{2+}, 50 nM of template, and 100 nM blocker B_{13} in 1x NEBuffer 2. The blank sample had all reagents except DNAzyme. Measurements from multiple independent experiments (n = 3) conducted on different days gave consistent results. Each curve in this figure represents the average of two measurements conducted on the same day.

Optimization of concentration of other reagents

To improve the performance of circuit, I optimized the concentrations of template–blocker complex, MBS, and polymerase to achieve high signal as well as low background. The results are demonstrated in Figures 3.8, 3.9, and 3.10, respectively. A high concentration of template–blocker T_9B_{13} greatly inhibited the amplification. Although the blocker was not displaced, the high concentration of the exposed toehold of the template could also compete with MBS to hybridize with the DNAzyme and prevent it from cleaving MBS efficiently. On the other hand, high concentrations of both the MBS and the polymerase increased the background. Larger amounts of MBS brought more impurities into the circuit and the high concentration of polymerase facilitated nonspecific amplification based on these impurities.
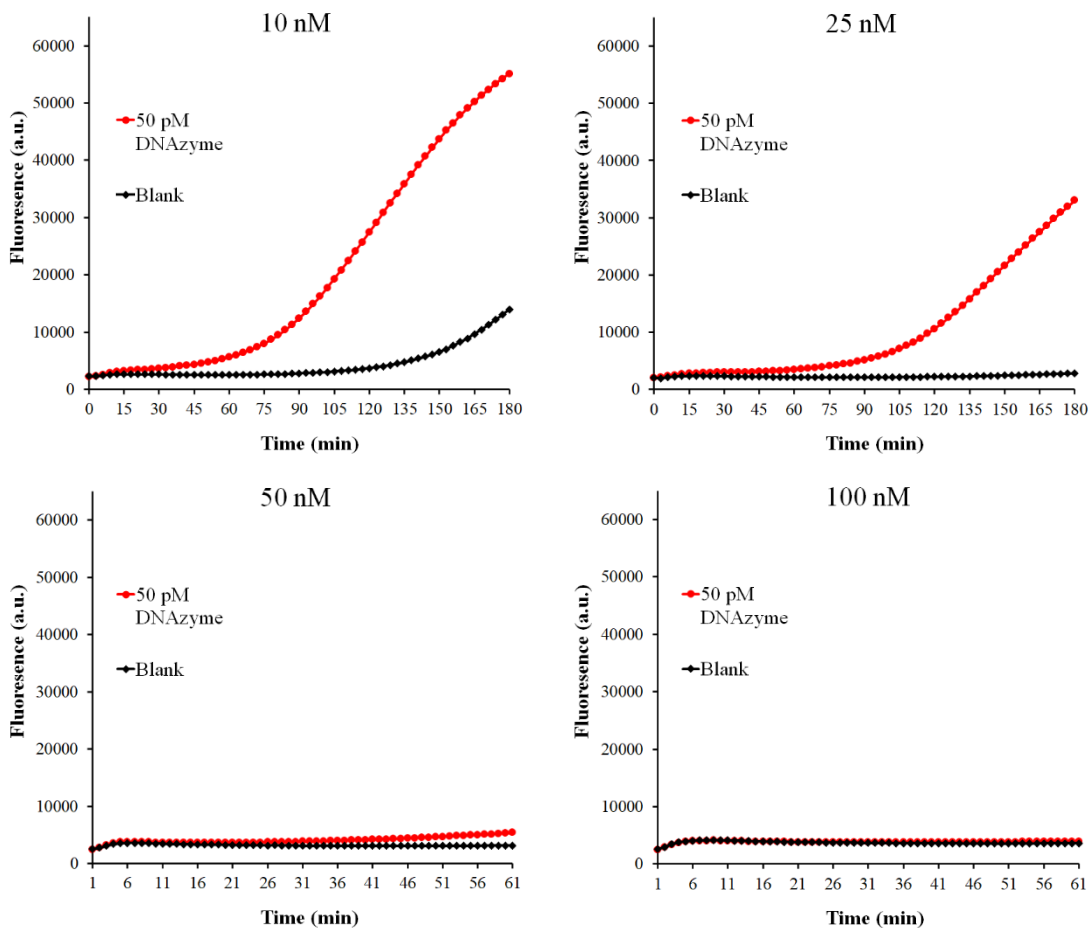
Figure 3.8. Optimization of the concentration of the template–blocker complex T_9B_{13}. Each reaction contained 200 nM MBS, 0.04 U/μL Klenow Fragment (3'→5' exo⁻) polymerase, 0.08 U/μL Nt.AlwI endonuclease, 0.08 U/μL T4 polynucleotide kinase, 100 mM dNTP, 0.5 mM Mn^{2+}, and 10–100 nM of T_9B_{13} complex in 1x NEBuffer 2. The ratio of template to blocker was 1:2. Measurements from multiple independent experiments (n = 3) conducted on different days gave consistent results. Each curve in this figure represents the average of two measurements conducted on the same day.
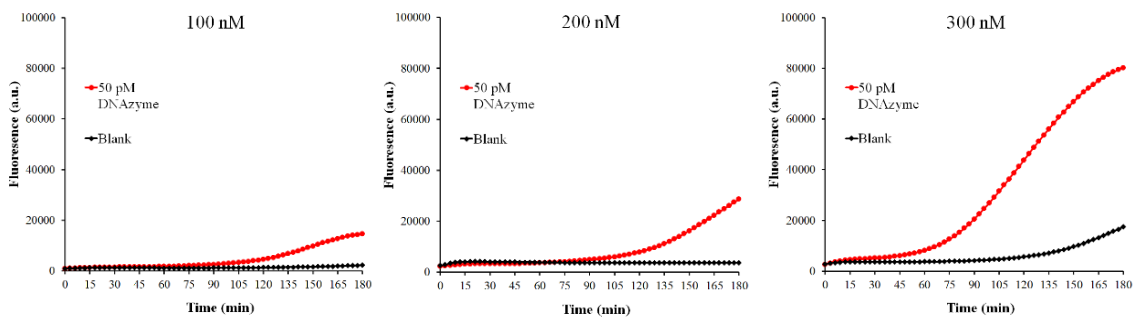
Figure 3.9. Optimization of the concentration of MBS. Each reaction contained 100–300 nM MBS, 0.04 U/μL Klenow Fragment (3'→5' exo⁻) polymerase, 0.08 U/μL Nt.AlwI endonuclease, 0.08 U/μL T4 polynucleotide kinase, 100 mM dNTP, 0.5 mM Mn^{2+}, and 25 nM of T_9B_{13} complex (1:2) in 1x NEBuffer 2. Each curve represents the average of duplicate analyses.
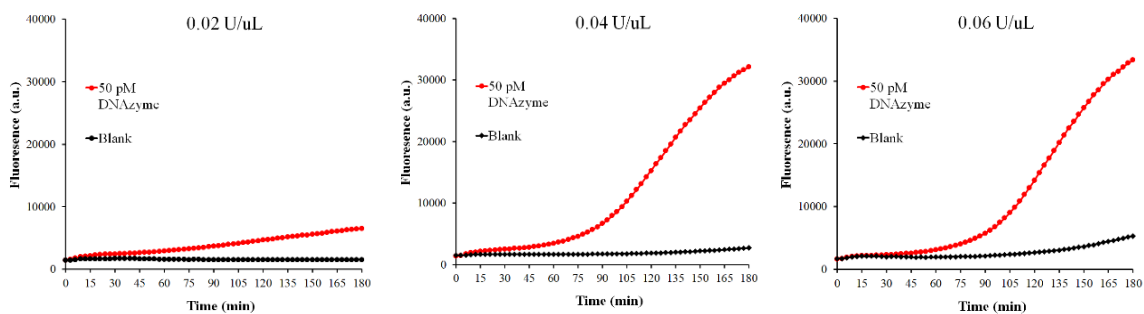
Figure 3.10. Optimization of the concentration of polymerase. Each reaction contained 200 nM MBS, 0.02–0.06 U/μL Klenow Fragment (3'→5' exo⁻) polymerase, 0.08 U/μL Nt.AlwI endonuclease, 0.08 U/μL T4 polynucleotide kinase, 100 mM dNTP, 0.5 mM Mn^{2+}, and 25 nM of T_9B_{13} complex (1:2) in 1x NEBuffer 2. Each curve represents the average of duplicate analyses.

Detection of two model targets

To demonstrate the proof-of-principle, I used the optimized SDA-DNAzyme circuit to detect two nucleic acid targets, the genetic sequences of the malarial parasite *P. falciparum* (Mal)[108] and the Hepatitis B virus (HBV).[109] The assays for the detection of the two targets had only different sensor arms of the subunits but the SDA-DNAzyme circuit remained the same. The lengths of the target domains Mal and HBV were 48 nt and 34 nt, respectively. Each sensor domain of the subunits was designed to target half of the target (24 or 17 nt) to form the MNAzymes. It was difficult to use this method to detect a shorter target, such as microRNA of about 22 nt,[6, 8] because the sensor arm of the subunit is only 11 nt (T_m<32 °C) and cannot form stable MNAzyme at 37 °C. For the detection of both model targets, no background was observed during 3 h of amplification (Figure 3.11). The selection of the blocker with no cleavage activity and the template with a shorter primer binding domain successfully eliminated the background in the circuit. Moreover, the detection of these two targets used the same SDA-DNAzyme circuit except for the sensor domain of the subunits. A higher concentration of target led to faster amplification and the limit of detection for two targets was about 5 fM.
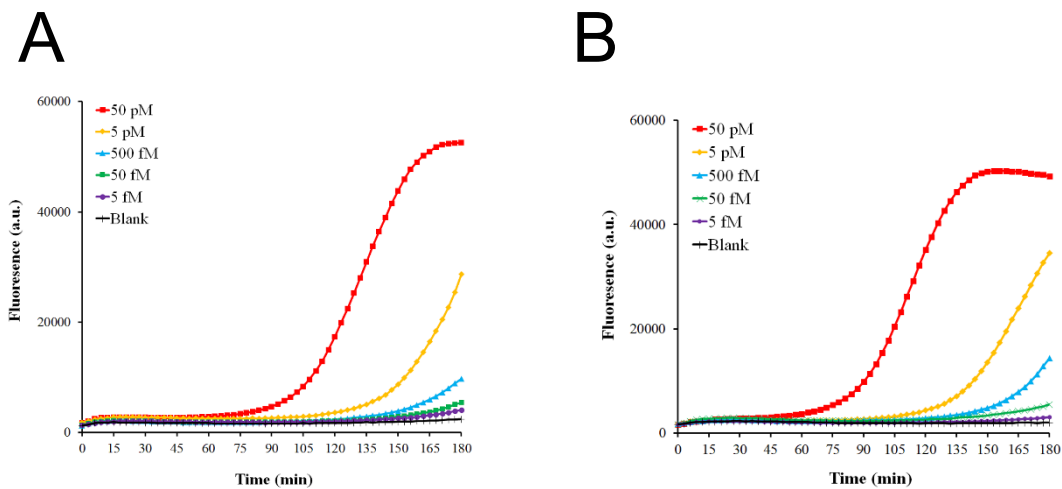
Figure 3.11. Detection of 50 pM–5 fM genetic sequences of (A) malarial parasite *P. falciparum* and (B) Hepatitis B virus using the SDA-DNAzyme circuit. Each reaction contained 1 nM of two subunits, 200 nM MBS, 0.04 U/µL Klenow Fragment ($3' \rightarrow 5'$ exo⁻) polymerase, 0.08 U/µL Nt.AlwI endonuclease, 0.08 U/µL T4 polynucleotide kinase, 100 mM dNTP, 0.5 mM Mn^{2+}, and 25 nM of T_9B_{13} complex (1:2) in 1x NEBuffer 2. Each curve represents the average of duplicate analyses.

3.4 Conclusion

I developed an MNAzyme-initiated SDA-DNAzyme circuit to detect various nucleic acid targets. Thanks to the positive feedback amplification between the SDA reaction and DNAzyme cleavage, the circuit can achieve the detection of two model targets at the fM level. The reaction of the circuit is performed continuously at 37 °C and all reagents were mixed in one test tube. By altering only the sensor arm of the subunits, I can detect any

nucleic acid target with no need oto change the sequence design of the circuit.

Chapter 4 Systematic investigation of the split location and secondary structure of the 10-23 DNAzyme for protein analysis

4.1 Introduction

Recently, MNAzymes have been increasingly adopted to the development of assays for the amplified detection of proteins.[80-83] For example, an MNAzyme-based assay for proteins was constructed using three subunits.[80] The binding of nucleic acid targets can directly and precisely assemble subunits into MNAzymes with a designated secondary structure, which is yet challenging for protein detection settings. Detection of proteins generally requires binding of affinity ligands (e.g. antibodies) that are not able to directly assemble subunits into MNAzymes. Therefore, additional designs are needed to translate the protein binding into the assembly of subunits, which makes MNAzymes constructed for nucleic acid argets not necessarily applicable to protein detection.

So far, there has been no systematic investigation of the split locations and secondary structure of the MNAzymes for protein detection. For the detection of nucleic acids, the single turnover number ($k_{obs.s}$) of MNAzymes with different split locations varied from 10^{-3} to 1.2 min^{-1}, showing a 1200-fold difference.[50] Therefore, a comparison of the split locations can also improve the catalytic activity of MNAzymes targeting proteins. On the other hand, the reported four-arm structure required three subunits to recognize the protein so that the assay was limited to the detection of large proteins.[80] The three-arm structure using only two subunits has been used more widely for the development of MNAzymes

to detect protein targets.

In this chapter, I aim to construct protein binding-assembled MNAzymes with a high catalytic activity, enabling sensitive detection of proteins. I choose to split a DNAzyme within its catalytic core to ensure that each subunit is completely inactive and that the assembled MNAzyme has a high activity. I systematically studied how the split location and secondary structure affect the catalytic activities of MNAzymes. I selected the 10-23 DNAzyme to construct protein binding-assembled MNAzymes because it has a high catalytic activity and small size. I compared all 14 split locations of the catalytical core of the 10-23 DNAzyme.[49,58] I studied the combination of these 14 split locations with two secondary structures. In addition to testing $k_{obs.s}$ of the assembled MNAzymes, I also measured the multiple turnover number ($k_{obs.m}$) to evaluate the overall signal generation process for analytical purposes.

4.2 Materials and methods

Reagents

All nucleic acids used in this chapter were synthesized by Integrated DNA Technologies (IDT; Coralville, IA, USA). Their sequences are listed in Table 4.1. Magnesium chloride ($MgCl_2$) and manganese chloride ($MnCl_2$) were obtained from Sigma (Oakville, ON, Canada). Tris-HCl buffer (pH=7.4) and Tris-EDTA buffer (pH=8.0) were purchased from Sigma-Aldrich (St. Louis, MO, USA) and Fisher Bioreagents (Pittsburgh, PA, USA), respectively. Tris-acetate buffer (pH=8.5) was prepared from the

ultrapure Tris (Invitrogen, Carlsbad, CA, USA) and acetic acid (Fisher Scientific, Fair Lawn, NJ, USA). Gold nanoparticle solution (AuNP, 20 nm, 7.0×10^{11} particles/mL) was obtained from Ted Pella (Redding, CA, USA). Tween 20 was purchased from Fisher Scientific (Fair Lawn, NJ, USA).

Table 4.1. The sequences of 10-23 DNAzyme, substrate, and 28 pairs of the subunits of MNAzymes for comparison of different split locations and structures. 'FAM-1*2*' is the substrate dually labeled with a thiol group and fluorophore on each end. Subunits '1hb' and 'b*2' form the four-arm structure. Subunits '1c' and 'c*2' form the three-arm structure. 'Pair 1' to 'Pair 14' contain 14 different split locations. Sequences in red are the intact or split catalytic core. FAM-1*2* is the RNA substrate labeled with a thiol group on the 5'-end and FAM fluorescence dye on the 3'-end. RNA nucleotides in bold indicate the cleavage site of the substrate. Sequences in green and blue are the binding arms complementary to the sequences of the substrate in the same colors. Sequences in black are the hairpin structure, which is the fourth arm of the four-arm structure. Sequences in purple are the complementary regions for the assembly of the MNAzymes.

DNA name	Sequences (5' to 3')
10-23 DNAzyme	CA GTC AGA GGC TAG CTA CAA CGA GGT CCA TG
FAM-1*2*	HS-TTT TTT TTT TTT CA TGG ACC **rG U** CTG ACT G T-FAM

DNA name		Sequences (5' to 3')
1hb	Pair 1	CAG TCA GA G GTG AG TTTTT CTC AC AGA CGT CAG CTC CA
	Pair 2	CAG TCA GA GG GTG AG TTTTT CTC AC AGA CGT CAG CTC CA
	Pair 3	CAG TCA GA GGC GTG AG TTTTT CTC AC AGA CGT CAG CTC CA
	Pair 4	CAG TCA GA GGC T GTG AG TTTTT CTC AC AGA CGT CAG CTC CA
	Pair 5	CAG TCA GA GGC TA GTG AG TTTTT CTC AC AGA CGT CAG CTC CA
	Pair 6	CAG TCA GA GGC TAG GTG AG TTTTT CTC AC AGA CGT CAG CTC CA
	Pair 7	CAG TCA GA GGC TAG C GTG AG TTTTT CTC AC AGA CGT CAG CTC CA
	Pair 8	CAG TCA GA GGC TAG CT GTG AG TTTTT CTC AC AGA CGT CAG CTC CA
	Pair 9	CAG TCA GA GGC TAG CTA GTG AG TTTTT CTC AC AGA CGT CAG CTC CA
	Pair 10	CAG TCA GA GGC TAG CTA C GTG AG TTTTT CTC AC

DNA name		Sequences (5' to 3')
b*2		AGA CGT CAG CTC CA
	Pair 11	CAG TCA GA GGC TAG CTA CA GTG AG TTTTT CTC AC AGA CGT CAG CTC CA
	Pair 12	CAG TCA GA GGC TAG CTA CAA GTG AG TTTTT CTC AC AGA CGT CAG CTC CA
	Pair 13	CAG TCA GA GGC TAG CTA CAA C GTG AG TTTTT CTC AC AGA CGT CAG CTC CA
	Pair 14	CAG TCA GA GGC TAG CTA CAA CG GTG AG TTTTT CTC AC AGA CGT CAG CTC CA
	Pair 1	TGG AGC TGA CGT CT GC TAG CTA CAA CGA GGT CCA TG
	Pair 2	TGG AGC TGA CGT CT C TAG CTA CAA CGA GGT CCA TG
	Pair 3	TGG AGC TGA CGT CT TAG CTA CAA CGA GGT CCA TG
	Pair 4	TGG AGC TGA CGT CT AG CTA CAA CGA GGT CCA TG
	Pair 5	TGG AGC TGA CGT CT G CTA CAA CGA GGT CCA TG
	Pair 6	TGG AGC TGA CGT CT CTA CAA CGA GGT CCA TG
	Pair 7	TGG AGC TGA CGT CT TA CAA CGA GGT CCA TG
	Pair 8	TGG AGC TGA CGT CT A CAA CGA GGT CCA TG

DNA name		Sequences (5' to 3')
	Pair 9	TGG AGC TGA CGT CT CAA CGA GGT CCA TG
	Pair 10	TGG AGC TGA CGT CT AA CGA GGT CCA TG
	Pair 11	TGG AGC TGA CGT CT A CGA GGT CCA TG
	Pair 12	TGG AGC TGA CGT CT CGA GGT CCA TG
	Pair 13	TGG AGC TGA CGT CT GA GGT CCA TG
	Pair 14	TGG AGC TGA CGT CT A GGT CCA TG
1c	Pair 1	CAG TCA GA G GGT GCA CGT CTC AG
	Pair 2	CAG TCA GA GG GGT GCA CGT CTC AG
	Pair 3	CAG TCA GA GGC GGT GCA CGT CTC AG
	Pair 4	CAG TCA GA GGC T GGT GCA CGT CTC AG
	Pair 5	CAG TCA GA GGC TA GGT GCA CGT CTC AG
	Pair 6	CAG TCA GA GGC TAG GGT GCA CGT CTC AG
	Pair 7	CAG TCA GA GGC TAG C GGT GCA CGT CTC AG
	Pair 8	CAG TCA GA GGC TAG CT GGT GCA CGT CTC AG
	Pair 9	CAG TCA GA GGC TAG CTA GGT GCA CGT CTC AG
	Pair 10	CAG TCA GA GGC TAG CTA C GGT GCA CGT CTC AG
	Pair 11	CAG TCA GA GGC TAG CTA CA GGT GCA CGT CTC AG
	Pair 12	CAG TCA GA GGC TAG CTA CAA GGT GCA CGT CTC AG
	Pair 13	CAG TCA GA GGC TAG CTA CAA C GGT GCA CGT CTC

DNA name		Sequences (5' to 3')
		AG
	Pair 14	CAG TCA GA GGC TAG CTA CAA CG GGT GCA CGT CTC AG
c*2	Pair 1	CTG AGA CGT GCA CC GC TAG CTA CAA CGA GGT CCA TG
	Pair 2	CTG AGA CGT GCA CC C TAG CTA CAA CGA GGT CCA TG
	Pair 3	CTG AGA CGT GCA CC TAG CTA CAA CGA GGT CCA TG
	Pair 4	CTG AGA CGT GCA CC AG CTA CAA CGA GGT CCA TG
	Pair 5	CTG AGA CGT GCA CC G CTA CAA CGA GGT CCA TG
	Pair 6	CTG AGA CGT GCA CC CTA CAA CGA GGT CCA TG
	Pair 7	CTG AGA CGT GCA CC TA CAA CGA GGT CCA TG
	Pair 8	CTG AGA CGT GCA CC A CAA CGA GGT CCA TG
	Pair 9	CTG AGA CGT GCA CC CAA CGA GGT CCA TG
	Pair 10	CTG AGA CGT GCA CC AA CGA GGT CCA TG
	Pair 11	CTG AGA CGT GCA CC A CGA GGT CCA TG
	Pair 12	CTG AGA CGT GCA CC CGA GGT CCA TG
	Pair 13	CTG AGA CGT GCA CC GA GGT CCA TG
	Pair 14	CTG AGA CGT GCA CC A GGT CCA TG

Conjugation of substrate on AuNP

The substrates of MNAzymes (Table 4.1) were conjugated on the AuNPs for quenching using a modified protocol.[106] A mixture containing 1 mL of AuNP, 12 µL of 100 µM substrates and 75 µL of 20% Tween 20 was incubated for 5 min at room temperature. The molar ratio of AuNP to substrate was 1:1000. Next, 750 µL of 5 M NaCl was added to the solution for 1 h salt aging. The mixture was sonicated every 20 min to avoid the aggregation of AuNPs. The mixture was then centrifuged at 2,400 g for 5 min to remove the unconjugated substrates in the supernatant solution. The precipitation was washed by 1 mL washing buffer (10 mM Tris-HCl + 0.05% Tween 20) three times. In each washing step, the solution was centrifuged at 16,200 g for 13 min followed by the removal of the supernatant solution. Finally, the conjugates were resuspended in washing buffer to a final concentration of 2 nM and stored at 4 °C prior to use.

Optimization of cofactor conditions

To optimize the cofactor conditions, I prepared a series of samples containing 200 pM 10-23 DNAzyme, 200 pM substrate-conjugated AuNPs, 200 mM NaCl, 20 mM Tris-acetate, and different concentrations of $MnCl_2$ or $MgCl_2$. Duplicate samples and standard solutions of substrate (0, 10, 20, 40, 60, and 100 nM) were loaded onto a 96-well plate. A Multi-Mode Microplate Reader FilterMax F5 from Molecular Devices (Sunnyvale, CA, USA) was used to monitor the fluorescence signal generated from substrate cleavage. The fluorescence intensity was measured at room temperature and excitation/emission of

485/535 nm. The signal was recorded every 3 min for 1 h to obtain the cleavage curves. The slopes of cleavage curves and the calibration curve of standard solution were cleavage rate (v, min^{-1}) and fluorescence intensity of unit concentration of substrate (F, nM^{-1}), respectively. Depending on these two parameters, I calculated the multiple turnover number $k_{obs.m} = \frac{v}{FC}$ (min^{-1}), indicating how many substrates were cleaved by one DNAzyme every 1 min. C was the concentration of the 10-23 DNAzyme (nM).

Investigation of the split location and secondary structure of MNAzymes using $k_{obs.m}$.

The sample of a typical test to determine $k_{obs.m}$ contained 2 nM annealed MNAzymes, 200 pM substrate-conjugated AuNPs, 0.5 mM MnCl$_2$, 10 mM MgCl$_2$, 200 mM NaCl, and 20 mM Tris-acetate. To anneal MNAzymes, I mixed 10 µL of 10 µM subunits 1hb (or 1c) and 10 µL of 10 µM subunits b*2 (or c*2) in 80 µL annealing buffer (10 mM Tris-HCl, 10 mM MgCl$_2$, 0.05% Tween 20). The mixtures were heated to 80 °C for 10 min and gradually cooled down to 20 °C in 1 h using the MJ Mini Personal Thermal Cycler (Bio-Rad). Duplicate samples of 28 MNAzymes, positive control (200 pM 10-23 DNAzyme), and standard solutions of the substrate were loaded onto the 96-well plate. Fluorescence intensity was measured and recorded under the same conditions as noted above.

Determination of intrinsic activity of the MNAzymes of the highest activity using $k_{obs.s}$

To determine the $k_{obs.s}$ of the selected MNAzymes and 10-23 DNAzyme, I prepared a solution containing 4 µM MNAzymes '1hb pair7+b*2 pair7' (Table 4.1) or 10-23 DNAzyme, 2 µM of 'FAM-1*2*', and 10 mM Tris-EDTA buffer. The solution was

incubated for 10 min at room temperature for the hybridization of MNAzymes (or DNAzyme) to substrate. Then, 2 mM $MnCl_2$ or 10 mM $MgCl_2$ was added to the solution to initiate the cleavage of substrates. Ten microliters of solution were sampled and added to the 10 μL of 50 mM EDTA solution to terminate the cleavage at eight different time points. Eight samples, positive control (substrate+NaOH), and negative control (only substrate) were loaded onto a 14% PAGE (polyacrylamide gel electrophoresis) gel and separated for 60 min under a 100 V electric field. Duplicate samples and controls were prepared in two gels and were run at the same time. The PAGE gels were imaged by the gel imaging system ImageQuant LAS 4000 (GE Healthcare Life Sciences, Pittsburgh, PA, USA) and the fluorescent intensity of the bands was analyzed by Image J 1.47. The percentage of cleaved products was calculated by the band intensity of product and uncleaved substrates. The $k_{obs.s}$ of the selected MNAzymes and 10-23 DNAzyme were obtained by fitting the percentages of cleaved product at eight designated times to the equation $Y\% = Y_\infty\% - Y_\infty\% \cdot exp(-t \cdot k_{obs.s})$. $Y\%$ and $Y_\infty\%$ indicated the percentages of cleaved products at times t and t_∞, respectively.

4.3 Results and discussion

Split locations and design of secondary structures of the MNAzymes

I designed a series of protein binding-assembled MNAzymes with different split locations and secondary structures to obtain the highest catalytic activity for analytical purposes. Figure 4.1A shows the 15 nucleotides of the catalytic core of the 10-23

DNAzyme, indicating 14 possible split locations. I designed protein binding-assembled MNAzymes with two secondary structures, the three-arm and the four-arm structures (Figure 4.1B). Although both structures were designed for detection of proteins in a sandwich format, two structures have different junctions within the assembled catalytic core. The MNAzymes with the three-arm structure were designed by extending two subunits (partial DNAzymes) with a pair of short complementary sequences, each of which was tethered with an affinity ligand through a DNA spacer. To achieve the four-arm structure, we incorporated a hairpin structure into one subunit and then extended the two subunits with a pair of short complementary sequences (Figure 4.1B). The presence of the hairpin structure allows the binding of two affinity ligands to the same protein molecule to induce hybridization of two short complementary sequences, forming a MNAzyme with the four-arm structure. Based on 14 split locations and two secondary structures, I constructed 28 MNAzymes and determined their catalytic activities. The assembly of MNAzymes relies on the binding of affinity ligands to the protein targets. After the MNAyzmes are assembled, the catalytic activities of the MNAyzmes are independent of protein binding. To simplify the determination of the catalytic activity, I extended the short complementary sequences of each MNAzyme to enable two subunits spontaneously assemble together (Table 4.1). I used these MNAzymes to study the effect of the split location and secondary structure on the catalytic activity of MNAyzmes.

A.

5'-G_1 G_2 C_3 T_4 A_5 G_6 C_7 T_8 A_9 C_{10} A_{11} A_{12} C_{13} G_{14} A_{15}

B.

Three-arm structure   Four-arm structure
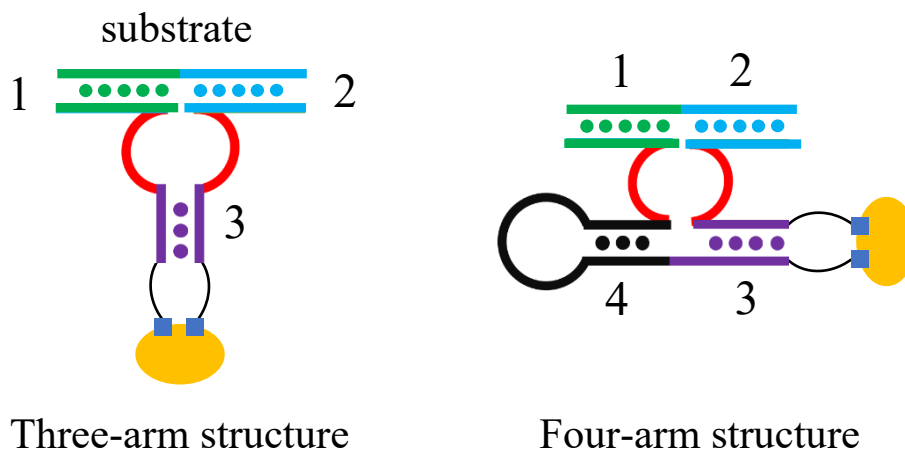
Figure 4.1. Catalytic core of the 10-23 DNAzyme and two secondary structures of the MNAzymes. (A) Fifteen nucleotides of the enzyme region of the 10-23 DNAzyme. (B) The three-arm and four-arm structures of MNAzymes used for protein detection. Duplex 1 in green and duplex 2 in blue are two arms formed by the hybridization between the subunits and substrate. Hybridization of the arm 3 in purple assembles the two subunits. Arm 3 only has 7 base pairs (Tm = 0.5 °C), which cannot form stable duplex in the absence of protein target. The hairpin 4 in black incorporated into one of the subunits makes it possible to form the four-arm structure using only two subunits (not requiring three subunits). Blue squares are affinity ligands binding to the protein molecule (in orange).

Optimization of cofactor conditions for cleavage reaction

Before the investigation of the split location and secondary structure, I optimized the

114

cofactor conditions to achieve the best cleavage conditions. Figure 4.2 shows the cleavage reactions of the substrate by 10-23 DNAzyme in different concentrations of Mn^{2+} or Mg^{2+}. The DNAzyme had good activity when I used 0.1–1 mM Mn^{2+} or 5–50 mM Mg^{2+}. Depending on the slopes of the cleavage curves and the calibration curve of the standard solutions, I calculated the $k_{obs.m}$ for all cofactor conditions (Figure 4.2). The highest $k_{obs.m}$ were 1.27 min^{-1} and 0.98 min^{-1} for 0.5 mM Mn^{2+} and 5 mM Mg^{2+}, respectively. Therefore, I used 0.5 mM Mn 2+ as the cofactor conditions for the following study of the split location and secondary structure. The fluorescence signal decreased significantly in the sample of 5 mM Mn^{2+} after 45 min and dropped to the baseline in the sample of 10 mM Mn^{2+}, suggesting the precipitation of Mn^{2+} at high pH values (Figure 4.2A).
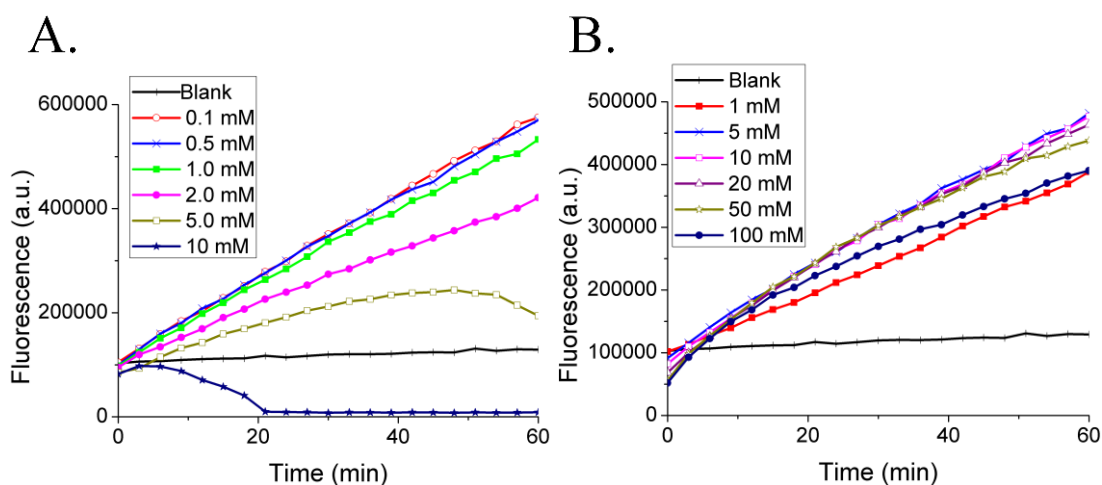
Figure 4.2. Real-time monitoring of substrate cleavage by 10-23 DNAzyme in different concentrations of (A) Mn^{2+} and (B) Mg^{2+}. Each sample contained 200 pM DNAzyme, 200 pM substrate-conjugated AuNPs, 200 mM NaCl, 20 mM Tris-acetate (pH=8.5), and

115

varying concentrations of MnCl$_2$ (0–10 mM) or MgCl$_2$ (0–100 mM). All samples were prepared in duplicate. Each curve is the average of duplicate measurements.

A.   **B.**
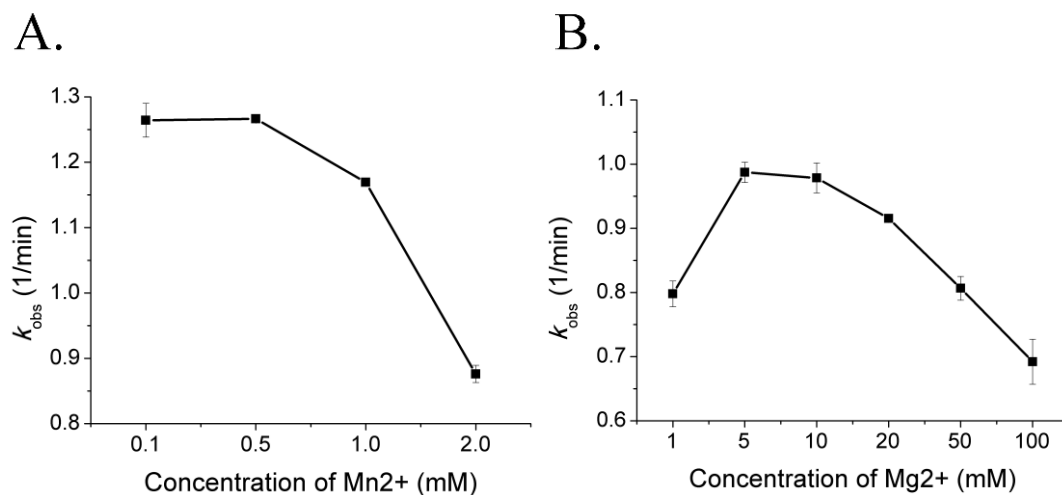
Figure 4.3. $k_{obs.m}$ of cleavage reactions in different concentrations of Mn^{2+} (A) and Mg^{2+} (B). The error bars represent the standard deviations of duplicate measurements.

Determining the $k_{obs.m}$ of 28 MNAzymes with different split locations and secondary structures

Under the optimum cofactor condition, I determined the $k_{obs.m}$ of the intact 10-23 DNAzyme and 28 MNAzymes (Figure 4.4). I created the conditions for multiple turnover cleavage by using 2 nM MNAzymes to cleave 80 nM substrate (0.2 nM substrate-functionalized AuNPs with loading amount of 400 substrates per AuNP). I achieved the highest $k_{obs.m}$ (0.53 min^{-1}) from the MNAzyme of the four-arm structure assembled from the two subunits at the split location of C7/T8 (Figure 4.4A and Table 4.2). MNAzymes

of the four-arm structure assembled from the two subunits of split locations G1/G2, A12/C13, and C13/G14 had kobs.m ranging from $0.2 - 0.43$ min^{-1}. MNAzymes of the three-arm structure assembled from the split locations C7/T8 and T8/A9 had $k_{obs.m}$ of 0.33 and 0.21 min^{-1}, but very low $k_{obs.m}$ ($< 10^{-2}$ min^{-1}) or no detectable activity for other split locations (Figure 4.4B and Table 4.2). MNAzymes of the four-arm structure generally had higher activities, suggesting that the four-arm structure is more favorable for the catalytic activity of protein binding-assembled MNAzymes. Interestingly, the split location (C7/T8) of the four-arm structure MNAzyme with the highest catalytic activity for protein detection is different from that (T8/A9) of the four-arm structure MNAzyme for the nucleic acid detection, reinforcing the importance of studying split locations and secondary structures for protein binding-assembled MNAzymes. There has been no report of systematic studies on the split locations and secondary structures in the formation of protein binding-assembled MNAzymes with high catalytic activities. These results demonstrate that both the split locations and secondary structures are critical for optimum catalytic activities of the assembled MNAzymes.
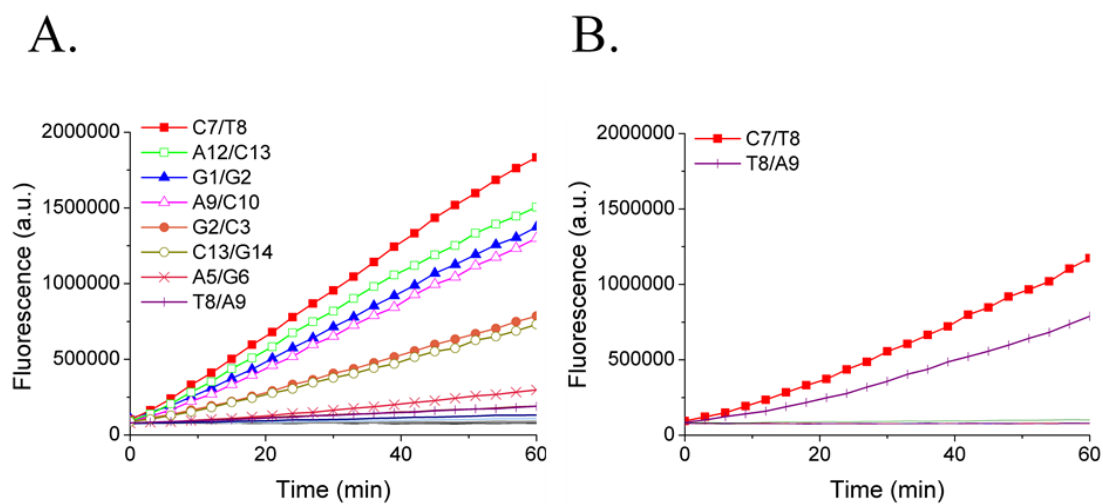
Figure 4.4. Real-time monitoring of the cleavage reaction catalyzed by MNAzymes with four-arm structure (A) and three-arm structure (B). Only the curves showing the obvious increase of fluorescence are labeled with the split location of catalytic core. C7/T8 indicates the catalytic core is split between 7th C and 8th T. Each sample contained 2 nM of MNAzymes, 200 pM substrate-conjugated AuNPs, 200 mM NaCl, 20 mM Tris-acetate (pH=8.5), 0.5 mM $MnCl_2$, and 10 mM $MgCl_2$. Measurements from multiple independent experiments (n = 2) conducted on different days gave consistent results. Each curve in this figure represents the average of two measurements conducted on the same day.

Table 4.2. $k_{obs.m}$ of the 10-23 DNAzyme and 28 MNAzymes designed to contain 14 split locations and 2 secondary structures. The symbol '/' is no detectable fluorescence signal for calculating the $k_{obs.m}$.

	$k_{obs.m}$ (min^{-1})	
10-23 DNAzyme	1.3	
Split location	Four-arm structure	Three-arm structure
G_1/G_2	3.8×10^{-1}	/
G_2/C_3	2.1×10^{-1}	/
C_3/T_4	No	/
T_4/A_5	3.0×10^{-3}	/
A_5/G_6	6.7×10^{-2}	/
G_6/C_7	3.7×10^{-3}	/
C_7/T_8	5.3×10^{-1}	3.3×10^{-1}
T_8/A_9	3.3×10^{-2}	2.1×10^{-1}
A_9/C_{10}	3.7×10^{-1}	6.2×10^{-3}
C_{10}/A_{11}	8.3×10^{-3}	/
A_{11}/A_{12}	1.7×10^{-2}	1.5×10^{-3}
A_{12}/C_{13}	4.3×10^{-1}	1.1×10^{-3}
C_{13}/G_{14}	2.0×10^{-1}	/
G_{14}/A_{15}	3.3×10^{-2}	/

Determining the $k_{obs.s}$ of the 10-23 DNAzyme and MNAzymes of the highest $k_{obs.m}$

To study the intrinsic catalytic activity, I measured the $k_{obs.s}$ of the DNAzyme and MNAzymes with the highest $k_{obs.m}$ under two cofactor conditions. Different from the $k_{obs.m}$ that evaluates the activity of catalyzing the cleavage of multiple substrates, the $k_{obs.s}$ demonstrates the activity of cleaving only one substrate. Therefore, I used a ratio of 2:1 (DNAzyme to substrate) to ensure all substrate can be cleaved in a single step. Figure 4.5 is the gel image of single step cleavage catalyzed by the 10-23 DNAzyme. Lanes 'Sub' and 'Sub + NaOH' are the positive control of only substrate and the negative control of substrate hydrolyzed by NaOH, respectively. Lanes '0.07' to '6 min' are the samples of cleavage reaction terminated by 50 mM EDTA at different time points. I used the buffer containing 1 mM EDTA to prevent the contamination of divalent metal ions that initiates the cleavage before adding the cofactor. The reaction was triggered by 2 mM Mn^{2+} (Figure 4.5.A) or 10 mM Mg^{2+} (Figure 4.5.B). The bands at the top of the gel image were uncleaved substrate of higher molecular weight and the bands at the bottom were cleaved substrate of lower molecular weight. The product bands had a higher intensity if the reaction time was longer. After 0.66 min of cleavage reaction, the band of uncleaved substrate could no longer be observed when using Mn^{2+} as cofactor. However, the cleavage of all substrate required more than 1 min in the gel of Mg^{2+}. These results suggested that Mn^{2+} is also more desirable than Mg^{2+} for a single cleavage step. The test of single step cleavage for the MNAzymes had the same conditions as that for the 10-23

DNAzyme. The cleavage of substrate catalyzed by the MNAzymes was obviously much slower than that catalyzed by the DNAzyme. For the cofactor conditions of Mn^{2+}, the cleavage of all substrate took 1.4 min. When Mg^{2+} was used as the cofactor, the MNAzymes could not cleave all of the substrate even after 4 min.
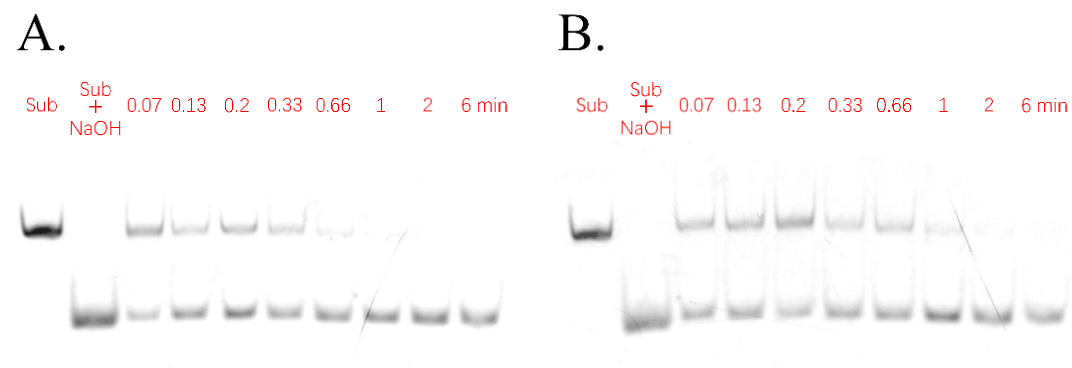
Figure 4.5. Gel images of the single step cleavage catalyzed by the 10-23 DNAzyme. (A) 1 mM Mn^{2+} was used as cofactor. (B) 9 mM Mg^{2+} was used as cofactor. Gel samples were prepared in duplicate and one of the gel images is shown in the figure.
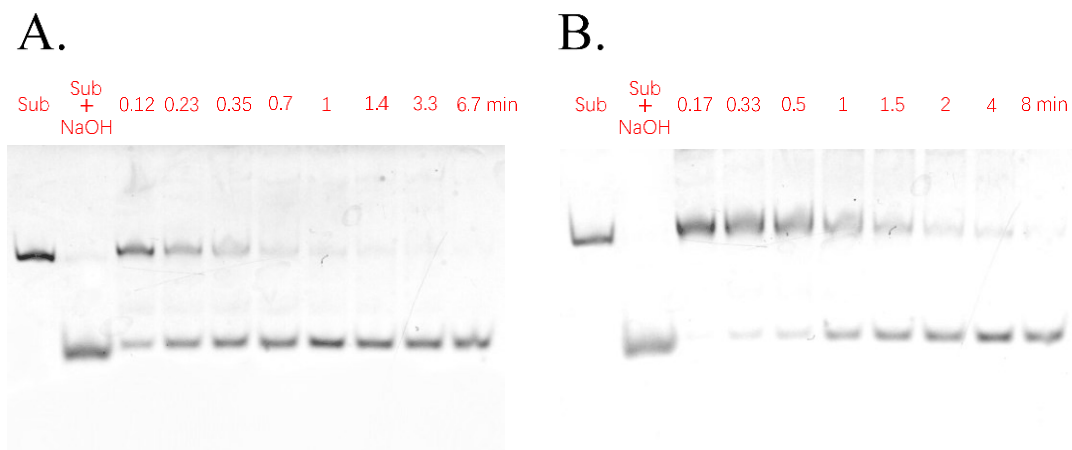
Figure 4.6. Gel images of the single step cleavage catalyzed by the MNAzymes of the highest $k_{obs.m}$. (A) 1 mM Mn^{2+} was used as cofactor and the reaction time was 6.7 min. (B) 9 mM Mg^{2+} was used as cofactor and the reaction time was 8 min. Gel samples were prepared in duplicate and one of the gel images is shown in the figure.

The percentage of cleaved product can be calculated by measuring the band intensity. Figure 4.7. demonstrates the calculated results of the 10-23 DNAzyme and MNAzymes using Mn^{2+} as cofactor. The $k_{obs.s}$ of cleavage reaction catalyzed by the 10-23 DNAzyme and the selected MNAzymes were 5.23 min^{-1} and 2.38 min^{-1}, respectively. The intrinsic activity of the DNAzyme is about two times higher than that of the MNAzymes. I also calculated the $k_{obs.s}$ of the cleavage reaction when using Mg^{2+} (Figure 4.8). Much lower $k_{obs.s}$ of 1.85 min^{-1} and 0.63 min^{-1} were obtained for the 10-23 DNAzyme and MNAzymes.
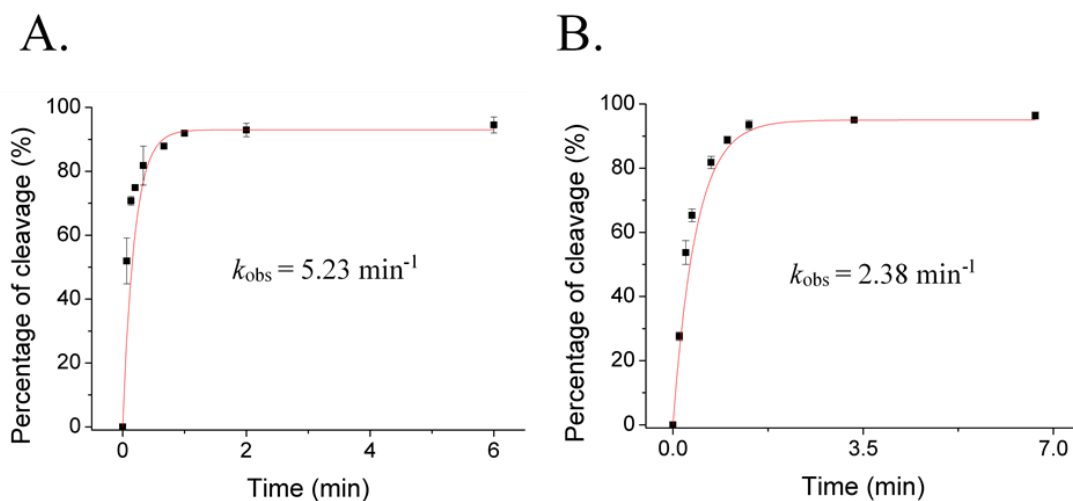
Figure 4.7. Cleavage curves and $k_{obs.s}$ of the 10-23 DNAzyme (A) and the MNAzymes of

the highest $k_{obs.m}$ (B) using Mn^{2+} as cofactor. The $k_{obs.s}$ were obtained by fitting the curve

to the equation Y% = Y_∞% - Y_∞%·exp(-t·$k_{obs.s}$). Y% and Y_∞% are the percentage of

cleaved products at the times t and t_∞. The error bars stand for the standard deviations of

two measurements.
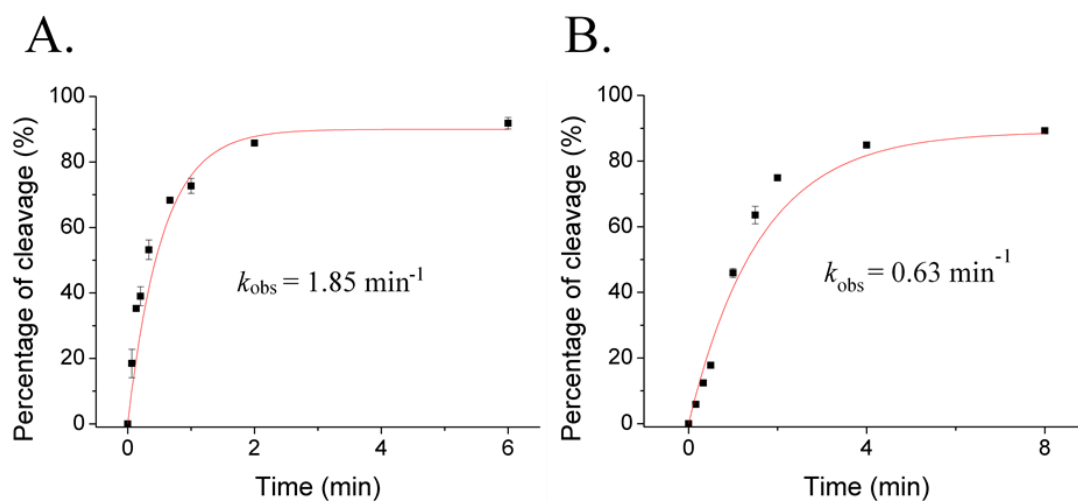
Figure 4.8. Cleavage curves and $k_{obs.s}$ of the 10-23 DNAzyme (A) and the MNAzymes of the highest $k_{obs.m}$ (B) using Mg^{2+} as cofactor. The $k_{obs.s}$ were obtained by fitting the curve to the same equation. The error bars stand for the standard deviations of two measurements.

Kinetics of cleavage reaction

To fully understand the activity of the MNAzymes, I tested both $k_{obs.m}$ and $k_{obs.s}$. The whole cleavage process comprises three steps: (1) hybridization of MNAzymes to the substrate, (2) cleavage of the substrate, and (3) dissociation of MNAzymes from the cleaved substrate. The $k_{obs.m}$ includes all three steps and evaluates the multiple rounds of cleavage. However, $k_{obs.s}$ only assesses step (2) and ignores the interaction between the substrate and binding arms. The comparison between $k_{obs.s}$ and $k_{obs.m}$ can determine the rate-limiting step and help the optimization of the cleavage reaction by enhancing the kinetics of steps (1) and (3). Taking the 10-23 DNAzyme as an example, the $k_{obs.s}$ and

$k_{\text{obs.m}}$ were 5.23 min^{-1} and 1.3 min^{-1} when using Mn^{2+}. The former was four times higher than the latter. This result suggested that the cleavage step (2) was not the only step affecting the rate of multiple cleavage steps. Both the hybridization step (1) and the dissociation step (3) limited the overall cleavage process.

The same conclusion can be derived from analyzing the kinetics of comparison of the two cofactors. Generally, the DNAzyme and MNAzymes had higher activity when the cofactor was Mn^{2+}. The $k_{\text{obs.s}}$ values of the DNAzyme were 5.23 min^{-1} for Mn^{2+} and 1.85 min^{-1} for Mg^{2+}, showing a 3-fold difference. The $k_{\text{obs.m}}$ values for two cofactors, on the other hand, had only a 1.3-fold difference. I attribute the smaller difference to the acceleration of the hybridization step (1) when Mg^{2+} is used as the cofactor. The concentration of Mg^{2+} was 10–20 times higher than that of Mn^{2+}, leading to stronger neutralization of the negative charge in the DNA backbone and faster hybridization step (1). Further evidence is that $k_{\text{obs.m}}$ of the 10-23 DNAzyme in 0.5 mM Mn^{2+} was enhanced from 1.27 min^{-1} (Figure 4.3A) to 1.3 min^{-1} (Table 4.2) when the sample contained extra 10 mM Mg^{2+}. However, this enhancement was not significant. It is necessary to further optimize the concentration of Mg^{2+} to improve the analytical performance for the detection of protein targets.

4.4 Conclusion

In this chapter, I systematically investigated the effect of split location and secondary structure on the activity of MNAzymes for catalyzing multiple cleavage steps. In general,

the MNAzymes with four-arm structure had higher $k_{obs.m}$ than MNAzymes with three-arm structure. The highest $k_{obs.m}$ was achieved when the MNAzyme had four-arm structure and a split location between C7 and T8. Although the split location T8/A9 has been widely used in the literature, the MNAzyme with this split location showed extremely low catalytic activity when using a hairpin structure as the fourth arm. By determining both the $k_{obs.m}$ and the $k_{obs.s}$ of the DNAzyme and MNAzymes in two cofactor conditions, I found that Mg^{2+} also plays an important role in improving the hybridization between DNAzyme (or MNAzymes) and substrate in the overall cleavage process. In the next chapter, I will use the MNAzymes of the highest $k_{obs.m}$ and optimize the Mg^{2+} conditions to detect two model protein targets.

Chapter 5 Binding-assembled MNAzyme for the detection of proteins

5.1 Introduction

Homogeneous binding assays are an ideal alternative to ELISA for protein detection because they can be performed in a single test tube with no need for immobilization and multiple washing steps.[66, 110] BINDA is one of the homogeneous binding assays that can convert the binding events to output DNA assembly.[74] The recognition behavior of BINDA motifs to the protein target is similar to the hybridization of two MNAzyme subunits to the nucleic acid target. Therefore, BINDA can be readily combined with the MNAzyme technique to achieve the homogeneous detection of proteins.

Herein, I used the subunits of MNAzyme with the highest $k_{obs.m}$ selected in Chapter 4 to design two BINDA motifs for protein detection. The hybridization between two motifs was carefully calculated so that they could assemble only in the presence of the target. The binding-assembled MNAzyme had high catalytic activity because of the successful selection of split location and secondary structure. I further optimized the concentration of Mg^{2+} to enhance the overall cleavage performance. Without assistance from isothermal amplification that requires protein enzymes, I used the MNAzyme technique to achieve the detection of two model targets at pM levels.

5.2 Material and Methods

Reagents

All nucleic acids used for the protein detection were obtained from Integrated DNA Technologies (IDT; Coralville, IA, USA). The sequences are listed in Table 5.1. Streptavidin from *Streptomyces avidinii* and bovine serum albumin (BSA) were purchased from Sigma (Oakville, ON, Canada). Human *a*-thrombin was obtained from Haematologic Technologies (Essex Junction, VT, USA). All the other reagents were the same as those used in Chapter 4.

Table 5.1. The sequences of BINDA motifs used for the detection of proteins. 1HB and B*2 are two biotinylated DNA motifs that detect streptavidin. 1HB-15 and B*2 are motifs recognizing thrombin. The sequences in italics are the anti-thrombin aptamers. Underlined sequences are designed to form the double-stranded spacers after hybridization with poly-A spacer.

DNA names	Sequences (5' to 3')
1HB	CAG TCA GA GGC TAG C GTG AG TTTTT CTC AC AGT GTT C AT TTT TTT TTT TTT TTT TTT-Biotin
B*2	Biotin-TTT TTT TTT TTT TTT TTT TA GAA CAC T TAC AAC GA GG TCC ATG
1HB-15	CAG TCA GA GGC TAG C GTG AG TTTTT CTC AC AGT GTT C
29-B*2	*AGT CCG TGG TAG GGC AGG TTG GGG TGA CT* <u>TTT TTT TTT TTT TTT T</u> A GAA CAC T TAC AAC GA GG TCC ATG
Poly-A spacer	AAA AAA AAA AAA AAA A

Detection of streptavidin

For the detection of streptavidin, 100 µL sample mixtures contained 1 nM of both DNA motifs (1HB and B*2), 0–400 pM streptavidin, 200 pM substrate-AuNP conjugates, 10 mM $MgCl_2$, 200 mM NaCl, 0.5 mM $MnCl_2$, and 20 mM Tris-acetate (pH=8.5). The

binding-assembled MNAzymes were prepared by incubating the mixture of 10 mM motifs and streptavidin in 10 mM Tris-HCl + 0.1% BSA (pH=7.4) for 15 min at room temperature. Ten microliters of the mixture were added to the 90 µL of all other reagents in a 96-well plate for sample loading. The fluorescence intensity was measured at room temperature and excitation/emission of 485/535 nm. The signal was recorded every 3 min for 1 h.

Detection of human *a*-thrombin

For the detection of thrombin, 100 µL sample mixture contained 2 nM annealed DNA motifs (1HB=15 and 29=B*2), 0–2 nM thrombin, 200 pM substrate-AuNP conjugates, 10 mM $MgCl_2$, 200 mM NaCl, 0.5 mM $MnCl_2$, and 20 mM Tris-acetate (pH=8.5). DNA motifs of double-stranded spacer were prepared by annealing the 10 µL of 10 µM 1HB-15 (or 29-B*2) and poly-A spacer in 10 mM Tris-HCl (pH=7.4), 10 mM $MgCl_2$, and 0.05% Tween 20. The solution was heated to 80 °C and cooled down to 20 °C in 1 h. For the preparation of binding-assembled MNAzymes, the solution containing 20 nM of two motifs and thrombin was incubated in 10 mM Tris-HCl + 100 mM NaCl + 5 mM KCl for 1 h at room temperature. Ten microliters of incubated solutions and blank samples were mixed with 90 µL of all other reagents in a 96-well plate. Real-time fluorescence increases of duplicate samples and five blank samples were measured and recorded for 2 h under the same conditions as noted above.

5.3 Results and discussion

Design of the binding-assembled MNAzyme

On the basis of the optimal split location and secondary structure for the best catalytic activity, I designed binding-assembled MNAzymes for the detection of proteins (Figure 5.1). In principle, the MNAzymes are assembled from two subunits, 1HB and B*2, only as a result of binding to the protein target. Each of the two subunits has a complementary domain (B and B*, purple sequences), a binding arm (1 and 2, green and blue sequences), the split enzyme region (red sequences), and an affinity ligand (blue squares). To achieve target-dependent assembly of two subunits, I designed the B and B* to have only 7 complementary nucleotides (nt) so that the estimated melting temperature (T_m) of the inter-strand hybridization is only 0.5 °C. In the presence of a protein target, the binding of the affinity ligands to the same protein molecule brings two subunits to close proximity, increasing their local effective concentrations. Consequently, the T_m of the hybridization between B and B* is increased to 45.3 °C. Thus, binding of the protein target to the two affinity ligands results in the formation of binding-assembled MNAzyme. The assembled MNAzyme hybridizes with the substrate 1*2* sequence and cleaves the substrate at its ribonucleotide site.
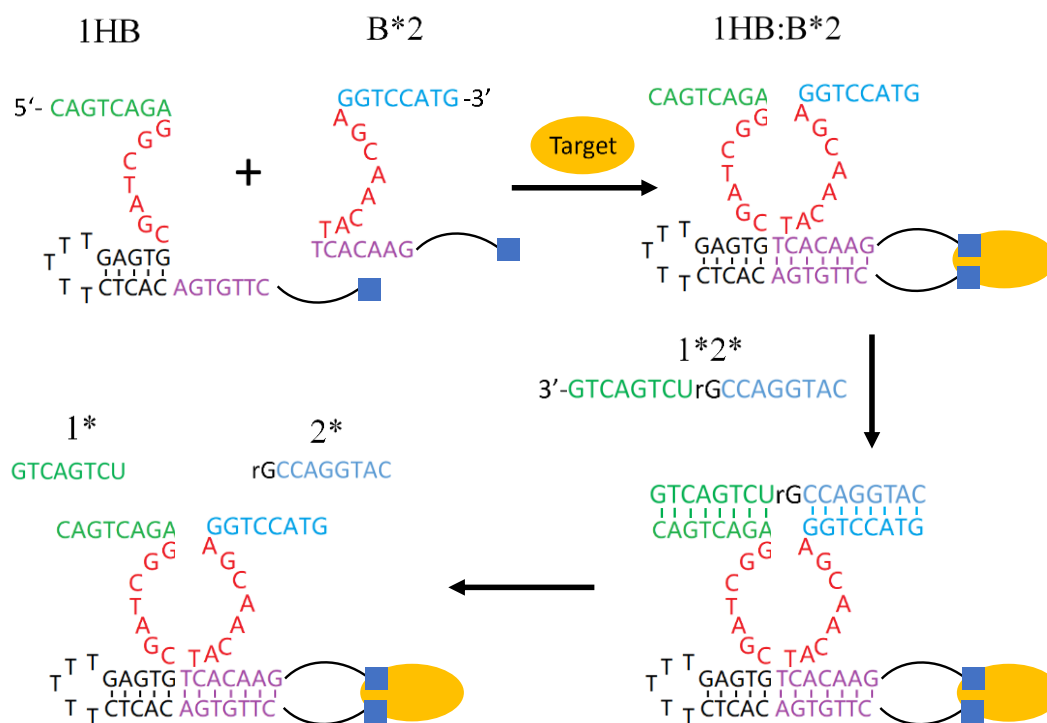
Figure 5.1. Design of two DNA motifs (1HB and B*2) and the formation of the binding-assembled MNAzyme. 1HB and B*2 are two subunits each labeled with an affinity ligand (blue square). Sequences 1 and 2 are two binding arms complementary to the substrate 1*2*. B and B* are complementary (7 nt, Tm = 0.5 °C) to each other but cannot form stable duplex in the absence of protein target. In the presence of target, two affinity ligands bind to it, which brings 1HB and B*2 into close proximity and increases their local effective concentration. The Tm of hybridization between B and B* increases to 45.3 °C so that 1HB and B*2 can form stable MNAzyme. The hairpin structure H serves as the fourth arm in the formation of binding-assembled MNAzymes.

Optimization of DNA motif for two model protein targets

The concentration of two DNA motifs greatly affects the sensitivity of the protein detection. Their high concentration can increase the T_m and lead to target-independent assembly of the MNAzymes. However, their low concentration will decrease the capability of DNA motifs to recognize the target. As demonstrated in Figure5.2, I first optimized the concentration of DNA motifs for the detection of streptavidin. High background was observed when the concentration reached to 10 nM. Thus, I obtained a very low signal-to-background ratio. A low concentration of 0.5 nM was also not favorable for the formation of binding-assembled MNAzymes because the target recognition was not efficient and the cleavage rate was low (thus, low signal). A concentration of 1 nM gave the highest signal as well as low background so that I achieved the high signal-to–background ratio of 37.
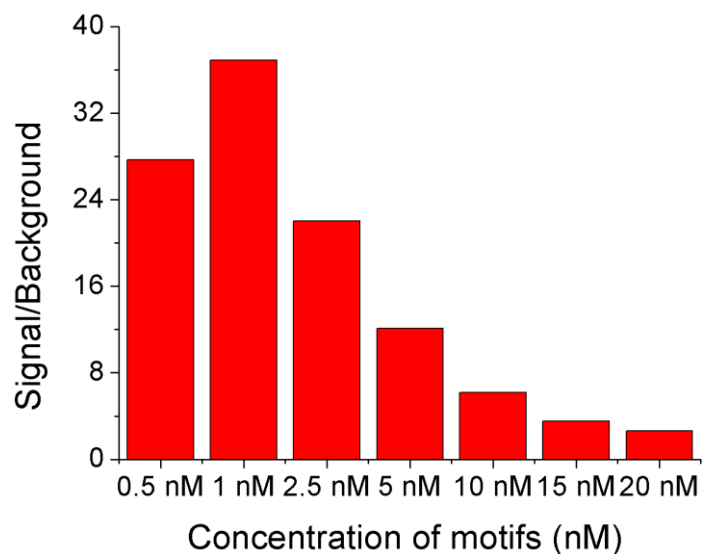
Figure 5.2. Optimization of the concentration of two DNA motifs (1HB and B*2, Table 5.1) for the detection of streptavidin. Each sample matrix contained 200 pM conjugates of substrate-AuNP, 200 mM NaCl, 0.5 mM $MnCl_2$, 20 mM Tris-acetate (pH=8.5), and different concentrations of DNA motifs. Streptavidin (200 pM) was incubated with motifs for 30 min at room temperature before being added to the sample matrix. Fluorescence signals of samples (signal) and blanks (background) at 1 h were used to calculate the ratio of signal to background. The signal to background ratios were obtained from calculating the average of analyses.

For the detection of thrombin, it was necessary to use the double-stranded spacer to prevent the intramolecular interaction of 1HB-15 and 29-B*2. When I used 10 nM of motifs with the single-stranded spacers, no signal and background could be detected (Figure 5.3). The motif 29-B*2 formed a hairpin structure with high T_m of 45 °C, which was not desirable for affinity binding. However, both signal and background were

observed if the motifs had the double-stranded spacers. The low flexibility of the double-stranded spacer opened the hairpin structure of the intramolecular interaction to restore the binding affinity.
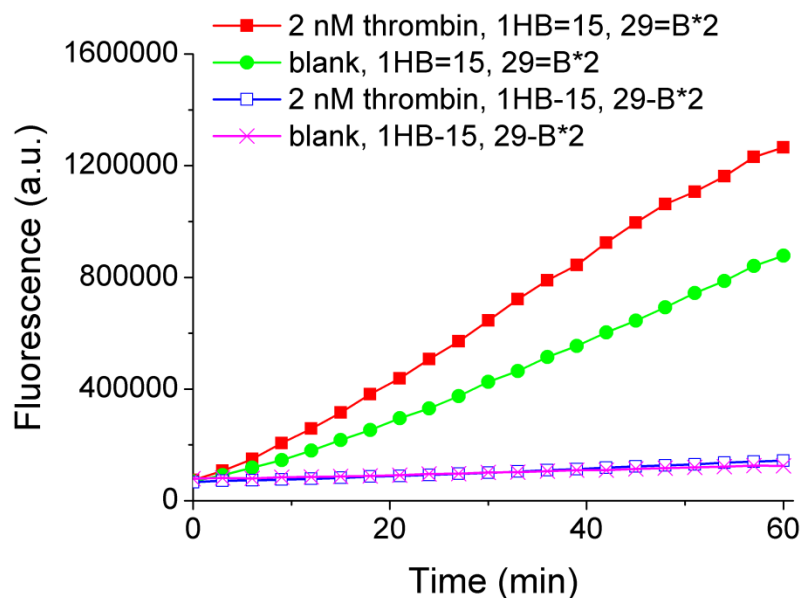
Figure 5.3. Comparison of double-stranded and single-stranded spacer for the design of DNA motif 1HB-15 and 29-B*2. '=' is the double-stranded spacer formed by annealing poly-A and 1HB-15 (or 29-B*2, Table S2). The positive samples contained 10 nM of two double-stranded or single-stranded motifs, 2 nM thrombin, 200 pM conjugates of substrate-AuNP, 200 mM NaCl, 0.5 mM MnCl$_2$, 10 mM Mg^{2+}, and 20 mM Tris-acetate (pH=8.5). Measurements from multiple independent experiments (n = 3) conducted on different days gave consistent results. Each curve in this figure represents the average of two measurements conducted on the same day.

I further optimized the concentration of two motifs 1HB=15 and 29=B*2 for the detection of thrombin. Using 2 nM of thrombin as the model target, I achieved the highest signal-to-background ratio when the concentration of two motifs was 2 nM (Figure 5.4).
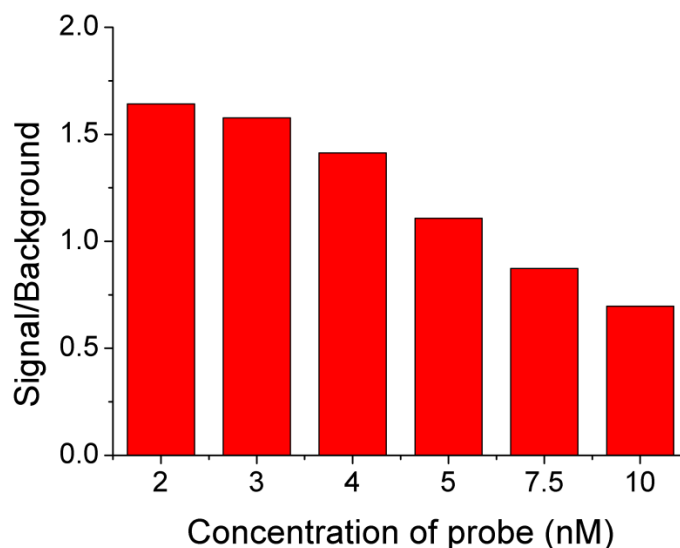
Figure 5.4. Optimization of concentrations of motifs 1HB=15 and 29=B*2 for the detection of thrombin. Each sample contained 200 pM conjugates of substrate-AuNP, 200 mM NaCl, 0.5 mM MnCl$_2$, 10 mM Mg^{2+}, 20 mM Tris-acetate (pH=8.5), and 2 nM of thrombin bound with different concentrations of DNA motifs. Thrombin (2 nM) was incubated with motifs for 30 min at room temperature before being added to the sample matrix. Fluorescence signals of samples and blanks at 2 h were used to calculate the ratio of signal to background. Measurements from multiple independent experiments (n = 2) conducted on different days gave consistent results. Each curve in this figure represents the average of two measurements conducted on the same day.

Optimization of the concentration of Mg^{2+}

As discussed in the last chapter, the concentration of Mg^{2+} needs to be optimized to enhance the hybridization step, thus improving the overall cleavage rate. However, Mg^{2+} can also enhance the stability of hybridization between two motifs (B and B*, Figure 5.1). If its concentration is too high, the two motifs can assemble to form the MNAzymes without target, resulting in high background. Figure 5.5 shows the effect of Mg^{2+} concentration on the signal-to-background ratio of protein detection. For the detection of streptavidin, 10 mM of Mg^{2+} significantly improved the signal and no high background was observed; a signal-to-background ratio of 150 was achieved. A concentration of Mg^{2+} higher than 20 mM increased the background while the signal was not enhanced. The overall cleavage rate was not further improved because the Mg^{2+} also stabilized the hybridization between the MNAzyme and cleaved product and slowed down the dissociation step. Without further enhancing the signal, a concentration of 50–100 mM of Mg^{2+} dramatically decreased the signal-to-background ratio to less than 15. I also optimized the Mg^{2+} concentration for the detection of thrombin (Figure 5.5B). A concentration of 5–30 mM generated high background and the highest signal-to-background ratio was achieved when using 2 mM Mg^{2+}.
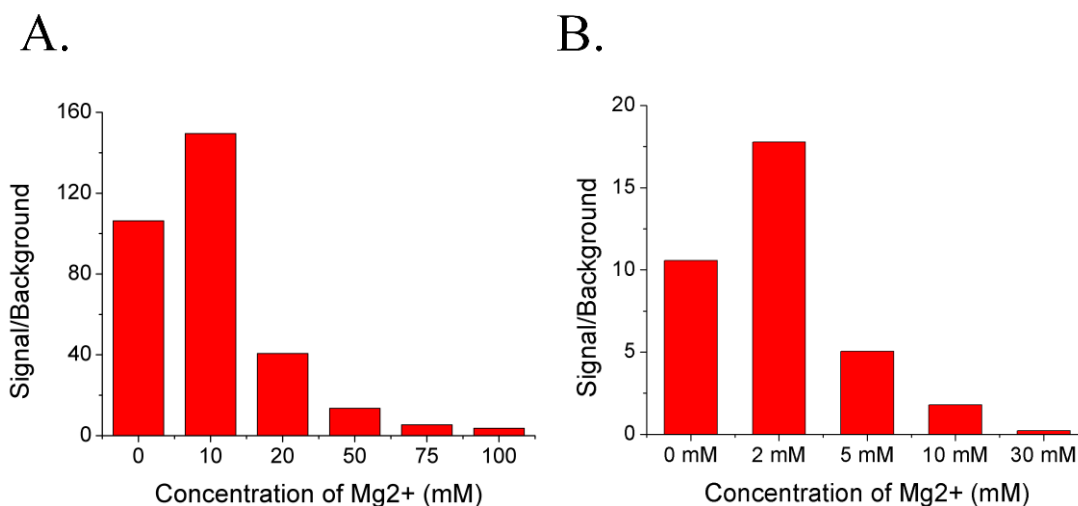
Figure 5.5. Optimization of Mg^{2+} concentration for the detection of 200 pM streptavidin (A) and 2 nM thrombin (B). For streptavidin, each sample contained 200 pM conjugates of substrate-AuNP, 200 mM NaCl, 0.5 mM $MnCl_2$, varying concentration of Mg^{2+} (0-100 mM), 20 mM Tris-acetate (pH=8.5), and 200 pM of streptavidin bound with 1 nM of two DNA motifs. For thrombin, each sample contained 200 pM conjugates of substrate-AuNP, 200 mM NaCl, 0.5 mM $MnCl_2$, varying concentration of Mg^{2+} (0-300 mM), 20 mM Tris-acetate (pH=8.5), and 2 nM of thrombin bound with 2 nM of two DNA motifs. The signal to background ratios were obtained from calculating the average of analyses.

Detection of two model targets

After determining the optimal conditions for the two targets, I detected a series of samples containing 0–400 pM streptavidin or 0–2 nM thrombin. Figure 5.6 displays the assay for the detection of streptavidin. In the absence of the target, the fluorophore group labeled on the substrates was quenched by the AuNPs. When the streptavidin target

appears, two biotins on DNA motifs 1HB and B*2 bind to the target, leading to the

formation of binding-assembled MNAzymes. As a result, the substrates 1*2* are cleaved

continuously and the fluorophore groups are released from the AuNPs.
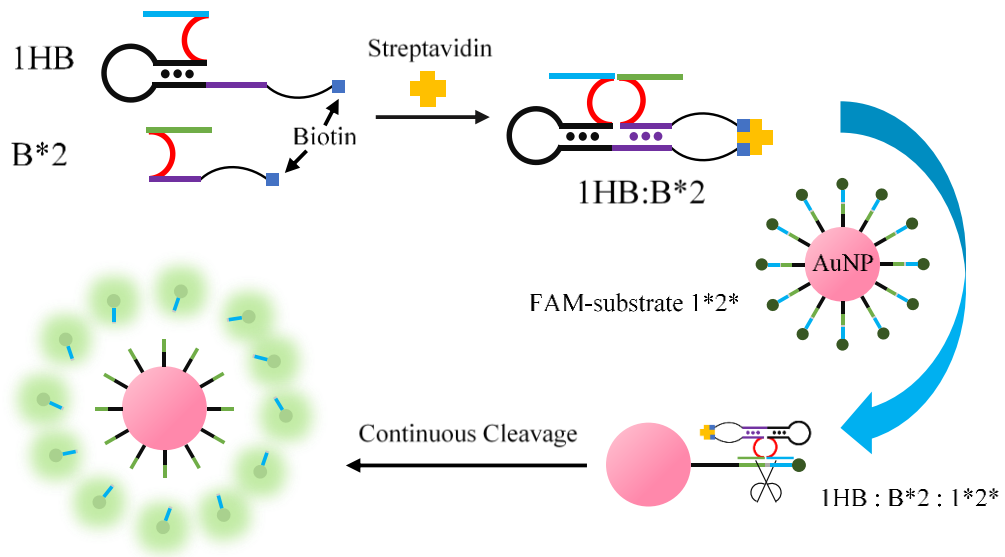
Figure 5.6. Binding-assembled MNAzyme for the detection of streptavidin. Formation of

binding-assembled MNAzymes 1HB:B*2 leads to the continuous cleavage of the FAM-

labeled substrate 1*2* and increase of the fluorescence signal.
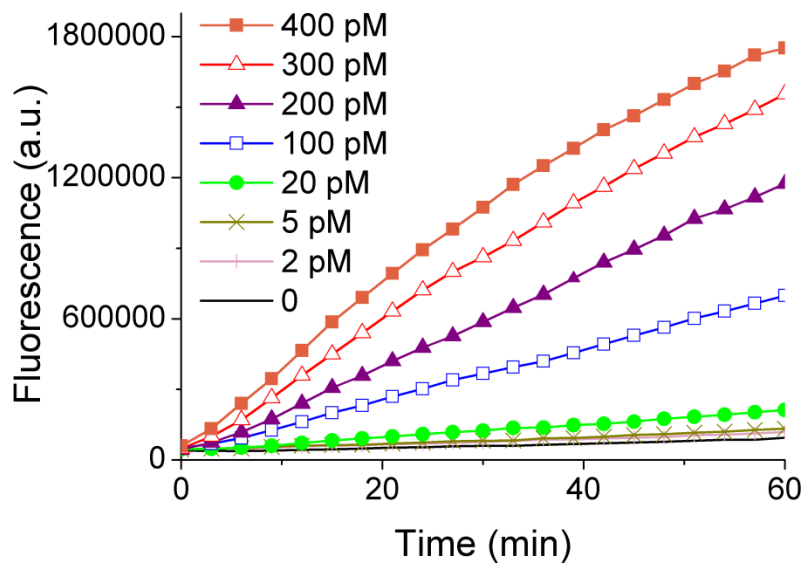
Figure 5.7. Real-time monitoring of the substrate cleavage in samples of different concentrations of streptavidin (0–400 pM). Each curve is the average of two measurements.

Figure 5.7 shows the fluorescence signal of the samples containing streptavidin with concentrations ranging from 0 to 400 pM. Higher concentration of the target formed more binding-assembled MNAzymes and displayed faster cleavage rate. Using the fluorescence values at 60 min of each sample, I obtained a linear relationship between the fluorescence increase and the concentration of the target (Figure 5.8). However, 400 pM of the streptavidin was not in this dynamic range. The cleavage rate decreased after 30 min due to the lower concentration of substrate. A detection limit of 1.3 pM was achieved for streptavidin.
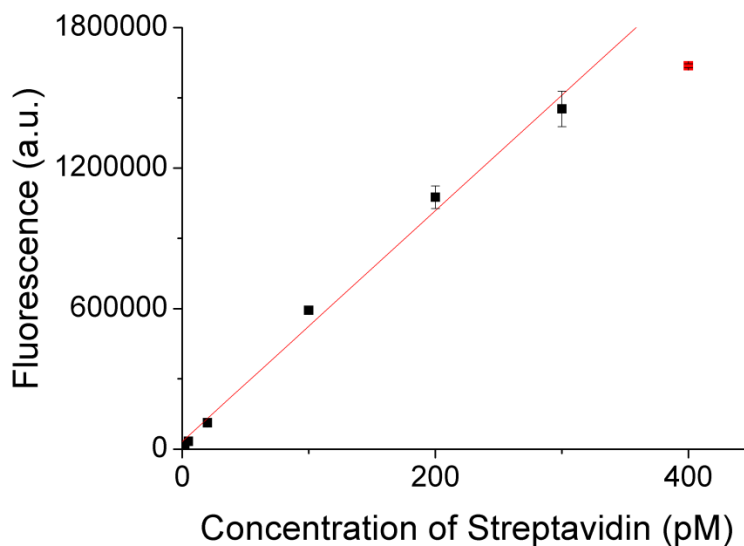
Figure 5.8. Linear relationship between the fluorescence signal at 60 min and concentration of streptavidin (2–300 pM). The error bars are the standard deviations of two detections. The data point in red color is not in this linear relationship.

I further performed the detection of thrombin to demonstrate the versatility of the designed binding-assembled MNAzymes. Two motifs with double-stranded spacers, 1HB=15 and 29=B*2, form the binding-assembled MNAzymes when the aptamers bind to thrombin (Figure 5.9). The cleavage of the substrate by the binding-assembled MNAzymes led to the increase of the fluorescence signal. I measured the fluorescence signal of samples with different concentrations of the target to obtain the dose–response for thrombin detection.
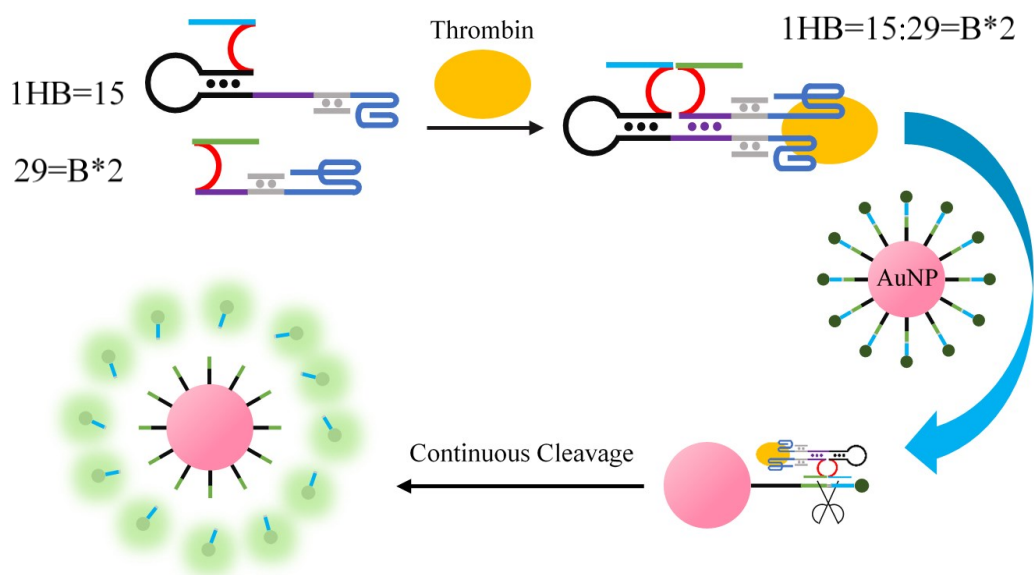
Figure 5.9. Scheme of detection method for thrombin. Two aptamers (15-mer and 29-mer) were used as affinity ligands for two DNA motifs (1HB=15 and 29=B*2). '=' indicates the double-stranded spacer (gray duplex).

For thrombin, I used higher concentrations ranging from 0.075 to 2 nM because the aptamer–thrombin interaction has a much lower binding affinity than that of biotin–streptavidin. As shown in Figure 5.10, the fluorescence increase corresponded to the concentration of thrombin. I obtained the linear relationship between the fluorescence signal and the concentration of the target from 0.075 to 2 nM. A limit of detection of 36 pM was achieved.
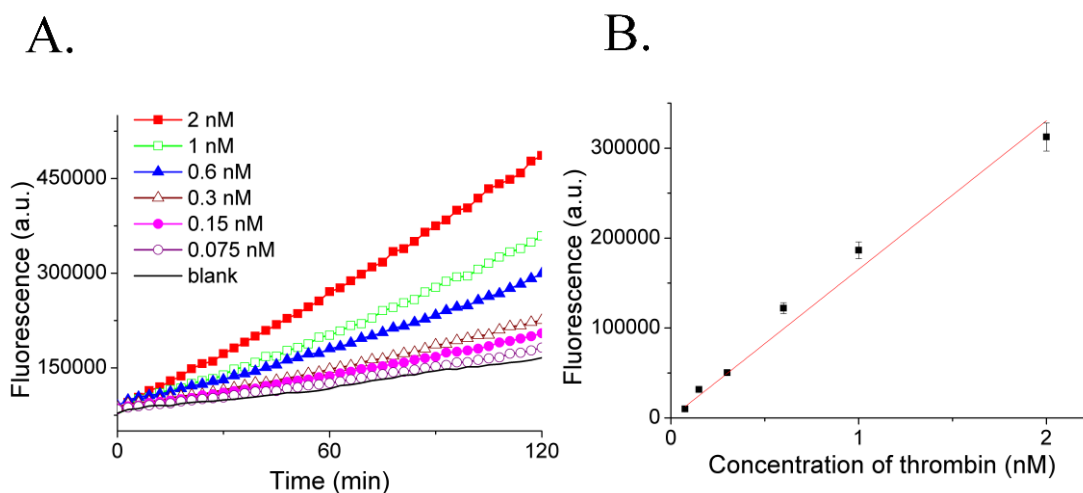
Figure 5.10. Real-time monitoring of cleavage reaction in samples containing different concentrations of thrombin (0.075–2 nM) (A) and linear relationship between the fluorescence signal at 2 h and concentration of the target (B). Each curve is the average of two measurements and the error bars are the standard deviation of two detections.

5.4 Conclusion

I used the MNAzyme selected in Chapter 4 to design the motifs of binding-assembled MNAzymes for two model protein targets. The motifs had short complementary regions that formed binding-assembled MNAzymes only in the presence of the targets. Optimization of the Mg^{2+} concentration significantly improved the performance of protein detection by enhancing the overall cleavage rate. The homogeneous detection of two proteins was performed in a single test tube without any immobilization and washing steps. Developed binding-assembled MNAzymes are ideal for the POC analysis of proteins and

the detection of different targets can be achieved with the alteration of the affinity ligands

on the motifs.

Chapter 6 Summarizing discussion, conclusion and future directions for research

The ultimate goal of this thesis work is to detect protein and nucleic acid molecules for POC testing and supporting diagnosis of diseases. Conventional methods for the determination of these biomolecules have extraordinary sensitivity. Nevertheless, they are not the optimal choices for the POC applications because they require either sophisticated instrument for thermal cycling or time-consuming washing steps. Isothermal and homogeneous assays can be performed at a mild and constant temperature and circumvent the need for washing steps.

Recent advances in incorporating CRISPR-Cas systems with isothermal amplification techniques improve the specificity of the isothermal assays for SARS-CoV-2. The detection formats include fluorescence method and lateral flow test, which use extra equipment for signal generation. Since colorimetric assay generates signal that can be directly observed by naked eye, it is ideal for the POC testes of SARS-CoV-2.

DNAzymes have also been integrated with isothermal amplification techniques to develop DNA circuit for isothermal detection of nucleic acids. The specific cleavage activity of DNAzyme has been utilized to construct positive feedback amplification to improve the sensitivity and reduce the number of primers to achieve lower background. However, reported circuits are designed for each individual targets. The change of target requires to redesign the sequences of the circuits. MNAzyme is an alternative strategy that

can be used to detect various targets by simply altering the sequences of the two sensor arms of the MNAzyme for target recognition.

A MNAzyme technique has been recently applied to the detection of proteins as well. The splitting of DNAzyme can affect greatly the cleavage activity of the assembled MNAzyme. For the nucleic acid detection, MNAzymes with different split locations have been reported to have a difference of activity of 1200-fold. So far, there is no study on the catalytic activity of MNAzymes for the protein analysis. Moreover, there are two types of secondary structures, three-arm and four-arm structures, for engineering the MNAzymes for proteins. The study on the combination of two structures with different split locations can select the MNAzyme with optimal catalytic activity for protein detection.

The integration of MNAzyme with BINDA technique can lead to homogeneous assays for proteins. BINDA is a homogeneous technique that is compatible with MNAzyme. Both methods recruit two probes for the target recognition and DNA assembly. After target binding, the input target is converted to the output DNA. MNAzymes detect nucleic acids to generate cleavage activity and BINDA detect protein to release the output DNA for further amplification. By changing the sensor arms of the MNAzyme to the affinity ligands for protein, I can achieve the homogeneous detection format and the amplification of the signal using cleavage activity.

In chapter 2, I have integrated the *trans*-cleavage activity of CRISPR-Cas with isothermal amplification techniques to develop a colorimetric assay for viral RNA. I designed a hairpin transducer to contain an RNA crosslinker, a DNA lock, and a DNA

loop. The CRISPR-Cas12a can convert the amplicon of viral RNA to the *trans*-cleavage of the DNA loop, which destabilizes the hybridization between the lock and crosslinker. The released crosslinker links AuNPs together and leads to the aggregation of AuNPs and color change of solution from red to purple. The assay is performed under a single-controlled temperature for RT-LAMP and the overall detection time is about 45 min. Taking advantage of centrifugation force of a portable spinner, I achieved a rapid color change within 1 min. The developed assay successfully detected 25 of 27 SARS-CoV-2 positive samples and achieved a clinical sensitivity of 92%. No false positive results were observed from 27 negative samples, indicating the assay has a good specificity.

In chapter 3, I used MNAzyme to initiate an SDA-DNAzyme circuit for the detection of various nucleic acid targets. The assay is performed in a single test tube at 37 °C. In the presence of target, the MNAzyme is activated to cleave the MBS, releasing the primer to hybridize with SDA template. The extension of primer produces more DNAzyme that can accelerate the cleavage rate of MBS to release more primers, thus forming a positive feedback amplification. A high sensitivity was achieved as demonstrated by the detection of the fM level of two model targets. I can detect other nucleic acids using the same circuit by changing the sensor arms of MNAzyme initiator.

In chapter 4, I exploited the effect of split location and secondary structure on the cleavage activity of the MNAzyme for protein analysis. I systematically compared 28 MNAzymes obtained from the combination of 14 split locations and two secondary structures. To engineer the four-arms structure with two subunits, I added a hairpin

structure to one of the subunits. I used $k_{obs.m}$ to evaluate catalytic activities of 28 MNAzymes for analytical purpose. By comparing the $k_{obs.m}$ with $k_{obs.s}$, I found that the cleavage reaction was not the rate-limiting step and association/dissociation steps played important roles in the overall cleavage process.

In chapter 5, I integrated the MNAzyme with BINDA to construct the binding-assembled MNAzyme for the homogeneous detection of proteins. The binding-assembled MNAzyme can detect the protein targets in a single test tube without any washing steps. When there is a protein target, the affinity ligands of two subunits can bind to the same target, resulting in the hybridization between short complementary regions. The formation of intact catalytic core activates the MNAzyme to cleave substrates on gold nanoparticles and generate amplified fluorescence signals. To achieve a good sensitivity, I optimized the concentration of Mg^{2+} to facilitate the association steps and avoid slowing down the dissociation. For two model targets, I achieved the detection limits at the pM level without polymerase-based amplification.

A future direction of this research will be to overcome the limitations of current assays and to expand their applications. The developed colorimetric assay for viral genes requires opening the test tube to add the CRISPR-Cas12a and AuNP reagents, which may lead to contamination of the viral targets. To address this issue, I propose to use the thermal stable Cas effector so that the CRISPR reagents can be mixed with the RT-LAMP solution at the beginning of the assay. The AuNP reagents can be loaded onto the lid of the test tube. After the *trans*-cleavage, the tube can be flicked to mix with the AuNPs.

Theoretically, the SDA-DNAzyme circuit is not limited to the detection of nucleic acid targets. Since I have developed the binding-assembled MNAzymes for the detection of protein targets in Chapter 5, it is possible to use the same strategy to initiate the circuit to achieve exponential amplification responding to proteins. However, the DNA motifs need to be rationally designed to avoid undesirable DNA interactions between the motifs and the sequences of the circuit, which may generate high background or decrease the amplification efficiency.

The investigation of split location and secondary structure of MNAzyme for protein analysis is not limited to the 10-23 DNAzyme. The 8-17 DNAzyme and its variants also have high catalytic activity in terms of $k_{obs.s}$. A similar method can be used to engineer the MNAzyme based on these DNAzymes. If I am able to find the MNAzymes with higher $k_{obs.m}$, I will improve the sensitivity of the developed assay using new binding-assembled MNAzymes.

References

1. Murray, R. K.; Granner, D. K.; Mayes, P. A.; Rodwell, V. W., Illustrated Biochemistry. New York: Mc Graw Hill: 2003.

2. Petsko, G. A.; Ringe, D., *Protein Structure and Function*. New Science Press: 2004.

3. Rusling, J. F.; Kumar, C. V.; Gutkind, J. S.; Patel, V., Measurement of biomarker proteins for point-of-care early detection and monitoring of cancer. *Analyst* **2010,** *135* (10), 2496-2511.

4. Wittmann, J.; Jäck, H.-M., Serum microRNAs as powerful cancer biomarkers. *Biochimica et Biophysica Acta (BBA)-Reviews on Cancer* **2010,** *1806* (2), 200-207.

5. Lilja, H.; Ulmert, D.; Vickers, A. J., Prostate-specific antigen and prostate cancer: prediction, detection and monitoring. *Nature Reviews Cancer* **2008,** *8* (4), 268-278.

6. Lu, J.; Getz, G.; Miska, E. A.; Alvarez-Saavedra, E.; Lamb, J.; Peck, D.; Sweet-Cordero, A.; Ebert, B. L.; Mak, R. H.; Ferrando, A. A., MicroRNA expression profiles classify human cancers. *Nature* **2005,** *435* (7043), 834.

7. Calin, G. A.; Croce, C. M., MicroRNA signatures in human cancers. *Nature Reviews Cancer* **2006,** *6* (11), 857.

8. Esquela-Kerscher, A.; Slack, F. J., Oncomirs—microRNAs with a role in cancer. *Nature Reviews Cancer* **2006,** *6* (4), 259.

9. Cho, W. C., OncomiRs: the discovery and progress of microRNAs in cancers. *Molecular Cancer* **2007,** *6* (1), 60.

10. Jiang, Q.; Wang, Y.; Hao, Y.; Juan, L.; Teng, M.; Zhang, X.; Li, M.; Wang, G.; Liu, Y., miR2Disease: a manually curated database for microRNA deregulation in human disease. *Nucleic Acids Research* **2008,** *37* , 98-104.

11. Croce, C. M., Causes and consequences of microRNA dysregulation in cancer. *Nature Reviews Genetics* **2009,** *10* (10), 704.

12. Kosaka, N.; Iguchi, H.; Ochiya, T., Circulating microRNA in body fluid: a new potential biomarker for cancer diagnosis and prognosis. *Cancer Science* **2010,** *101* (10), 2087-2092.

13. Wang, G.-K.; Zhu, J.-Q.; Zhang, J.-T.; Li, Q.; Li, Y.; He, J.; Qin, Y.-W.; Jing, Q., Circulating microRNA: a novel potential biomarker for early diagnosis of acute myocardial infarction in humans. *European Heart Journal* **2010,** *31* (6), 659-666.

14. Nimse, S. B.; Sonawane, M. D.; Song, K.-S.; Kim, T., Biomarker detection technologies and future directions. *Analyst* **2016,** *141* (3), 740-755.

15. Wang, J., Electrochemical biosensors: towards point-of-care cancer diagnostics. *Biosensors and Bioelectronics* **2006,** *21* (10), 1887-1892.

16. Carter, L. J.; Garner, L. V.; Smoot, J. W.; Li, Y.; Zhou, Q.; Saveson, C. J.; Sasso, J. M.; Gregg, A. C.; Soares, D. J.; Beskid, T. R., Assay techniques and test development for COVID-19 diagnosis. *ACS Central Science* **2020**, *6* (5), 591-605.

17. Udugama, B.; Kadhiresan, P.; Kozlowski, H. N.; Malekjahani, A.; Osborne, M.; Li, V. Y.; Chen, H.; Mubareka, S.; Gubbay, J. B.; Chan, W. C., Diagnosing COVID-19: the disease and tools for detection. *ACS Nano* **2020,** *14* (4), 3822-3835.

18. Feng, W.; Newbigging, A. M.; Le, C.; Pang, B.; Peng, H.; Cao, Y.; Wu, J.; Abbas, G.; Song, J.; Wang, D.-B., Molecular diagnosis of COVID-19: challenges and research needs. *Analytical Chemistry* **2020,** *92* (15), 10196-10209.

19. Bartlett, J. M.; Stirling, D., A short history of the polymerase chain reaction. In *PCR protocols*, Springer: 2003; pp 3-6.

20. Kubista, M.; Andrade, J. M.; Bengtsson, M.; Forootan, A.; Jonák, J.; Lind, K.; Sindelka, R.; Sjöback, R.; Sjögreen, B.; Strömbom, L., The real-time polymerase chain reaction. *Molecular Aspects of Medicine* **2006,** *27* (2-3), 95-125.

21. Engvall, E.; Perlmann, P., Enzyme-linked immunosorbent assay (ELISA) quantitative assay of immunoglobulin G. *Immunochemistry* **1971,** *8* (9), 871-874.

22. Lequin, R. M., Enzyme immunoassay (EIA)/enzyme-linked immunosorbent assay (ELISA). *Clinical Chemistry* **2005,** *51* (12), 2415-2418.

23. Sakamoto, S.; Putalun, W.; Vimolmangkang, S.; Phoolcharoen, W.; Shoyama, Y.; Tanaka, H.; Morimoto, S., Enzyme-linked immunosorbent assay for the quantitative/qualitative analysis of plant secondary metabolites. *Journal of Natural Medicines* **2018,** *72* (1), 32-42.

24. Zhang, S.; Garcia-D'Angeli, A.; Brennan, J. P.; Huo, Q., Predicting detection limits of enzyme-linked immunosorbent assay (ELISA) and bioanalytical techniques in general. *Analyst* **2014,** *139* (2), 439-445.

25. Corman, V. M.; Landt, O.; Kaiser, M.; Molenkamp, R.; Meijer, A.; Chu, D. K.; Bleicker, T.; Brünink, S.; Schneider, J.; Schmidt, M. L., Detection of 2019 novel

coronavirus (2019-nCoV) by real-time RT-PCR. *Eurosurveillance* **2020,** *25* (3), 2000045.

26. Zhou, P.; Yang, X.-L.; Wang, X.-G.; Hu, B.; Zhang, L.; Zhang, W.; Si, H.-R.; Zhu, Y.; Li, B.; Huang, C.-L., A pneumonia outbreak associated with a new coronavirus of probable bat origin. *Nature* **2020,** *579* (7798), 270-273.

27. Chu, D. K.; Pan, Y.; Cheng, S. M.; Hui, K. P.; Krishnan, P.; Liu, Y.; Ng, D. Y.; Wan, C. K.; Yang, P.; Wang, Q., Molecular diagnosis of a novel coronavirus (2019-nCoV) causing an outbreak of pneumonia. *Clinical Chemistry* **2020,** *66* (4), 549-555.

28. Zhao, Y.; Chen, F.; Li, Q.; Wang, L.; Fan, C., Isothermal amplification of nucleic acids. *Chemical Reviews* **2015,** *115* (22), 12491-12545.

29. Compton, J., Nucleic acid sequence-based amplification. *Nature* **1991,** *350*, 91-92.

30. Vincent, M.; Xu, Y.; Kong, H., Helicase-dependent isothermal DNA amplification. *EMBO Reports* **2004,** *5* (8), 795-800.

31. Piepenburg, O.; Williams, C. H.; Stemple, D. L.; Armes, N. A., DNA detection using recombination proteins. *PLoS Biology* **2006,** *4* (7), e204.

32. Walker, G. T.; Fraiser, M. S.; Schram, J. L.; Little, M. C.; Nadeau, J. G.; Malinowski, D. P., Strand displacement amplification—an isothermal, in vitro DNA amplification technique. *Nucleic Acids Research* **1992,** *20* (7), 1691-1696.

33. Van Ness, J.; Van Ness, L. K.; Galas, D. J., Isothermal reactions for the amplification of oligonucleotides. *Proceedings of the National Academy of Sciences* **2003,** *100* (8), 4504-4509.

34. Fire, A.; Xu, S.-Q., Rolling replication of short DNA circles. *Proceedings of the*

National Academy of Sciences **1995,** *92* (10), 4641-4645.

35. Daubendiek, S. L.; Ryan, K.; Kool, E. T., Rolling-circle RNA synthesis: circular oligonucleotides as efficient substrates for T7 RNA polymerase. *Journal of the American Chemical Society* **1995,** *117* (29), 7818-7819.

36. Notomi, T.; Okayama, H.; Masubuchi, H.; Yonekawa, T.; Watanabe, K.; Amino, N.; Hase, T., Loop-mediated isothermal amplification of DNA. *Nucleic Acids Research* **2000,** *28* (12), e63-e63.

37. Guatelli, J. C.; Whitfield, K. M.; Kwoh, D. Y.; Barringer, K. J.; Richman, D. D.; Gingeras, T. R., Isothermal, in vitro amplification of nucleic acids by a multienzyme reaction modeled after retroviral replication. *Proceedings of the National Academy of Sciences* **1990,** *87* (5), 1874-1878.

38. Tomita, N.; Mori, Y.; Kanda, H.; Notomi, T., Loop-mediated isothermal amplification (LAMP) of gene sequences and simple visual detection of products. *Nature Protocols* **2008,** *3* (5), 877-882.

39. Pang, B.; Xu, J.; Liu, Y.; Peng, H.; Feng, W.; Cao, Y.; Wu, J.; Xiao, H.; Pabbaraju, K.; Tipples, G., Isothermal amplification and ambient visualization in a single tube for the detection of SARS-CoV-2 using loop-mediated amplification and CRISPR technology. *Analytical Chemistry* **2020,** *92* (24), 16204-16212.

40. Feng, W.; Newbigging, A. M.; Tao, J.; Cao, Y.; Peng, H.; Le, C.; Wu, J.; Pang, B.; Li, J.; Tyrrell, D. L., CRISPR technology incorporating amplification strategies: molecular assays for nucleic acids, proteins, and small molecules. *Chemical Science* **2021,** *12* (13),

4683-4698.

41. Jinek, M.; Chylinski, K.; Fonfara, I.; Hauer, M.; Doudna, J. A.; Charpentier, E., A programmable dual-RNA–guided DNA endonuclease in adaptive bacterial immunity. *Science* **2012,** *337* (6096), 816-821.

42. Abudayyeh, O. O.; Gootenberg, J. S.; Konermann, S.; Joung, J.; Slaymaker, I. M.; Cox, D. B.; Shmakov, S.; Makarova, K. S.; Semenova, E.; Minakhin, L., C2c2 is a single-component programmable RNA-guided RNA-targeting CRISPR effector. *Science* **2016,** *353* (6299).

43. Chen, J. S.; Ma, E.; Harrington, L. B.; Da Costa, M.; Tian, X.; Palefsky, J. M.; Doudna, J. A., CRISPR-Cas12a target binding unleashes indiscriminate single-stranded DNase activity. *Science* **2018,** *360* (6387), 436-439.

44. Gootenberg, J. S.; Abudayyeh, O. O.; Lee, J. W.; Essletzbichler, P.; Dy, A. J.; Joung, J.; Verdine, V.; Donghia, N.; Daringer, N. M.; Freije, C. A., Nucleic acid detection with CRISPR-Cas13a/C2c2. *Science* **2017,** *356* (6336), 438-442.

45. Karvelis, T.; Bigelyte, G.; Young, J. K.; Hou, Z.; Zedaveinyte, R.; Budre, K.; Paulraj, S.; Djukanovic, V.; Gasior, S.; Silanskas, A., PAM recognition by miniature CRISPR–Cas12f nucleases triggers programmable double-stranded DNA target cleavage. *Nucleic Acids Research* **2020,** *48* (9), 5016-5023.

46. Broughton, J. P.; Deng, X.; Yu, G.; Fasching, C. L.; Servellita, V.; Singh, J.; Miao, X.; Streithorst, J. A.; Granados, A.; Sotomayor-Gonzalez, A., CRISPR–Cas12-based detection of SARS-CoV-2. *Nature Biotechnology* **2020,** *38* (7), 870-874.

47. Dai, Y.; Somoza, R. A.; Wang, L.; Welter, J. F.; Li, Y.; Caplan, A. I.; Liu, C. C., Exploring the Trans-Cleavage Activity of CRISPR-Cas12a (cpf1) for the Development of a Universal Electrochemical Biosensor. *Angewandte Chemie* **2019,** *131* (48), 17560-17566.

48. English, M. A.; Soenksen, L. R.; Gayet, R. V.; de Puig, H.; Angenent-Mari, N. M.; Mao, A. S.; Nguyen, P. Q.; Collins, J. J., Programmable CRISPR-responsive smart materials. *Science* **2019,** *365* (6455), 780-785.

49. Peng, H.; Newbigging, A. M.; Wang, Z.; Tao, J.; Deng, W.; Le, X. C.; Zhang, H., DNAzyme-mediated assays for amplified detection of nucleic acids and proteins. *Analytical Chemistry* **2017,** *90* (1), 190-207.

50. Mokany, E.; Bone, S. M.; Young, P. E.; Doan, T. B.; Todd, A. V., MNAzymes, a versatile new class of nucleic acid enzymes that can function as biosensors and molecular switches. *Journal of the American Chemical Society* **2009,** *132* (3), 1051-1059.

51. Gong, L.; Zhao, Z.; Lv, Y.-F.; Huan, S.-Y.; Fu, T.; Zhang, X.-B.; Shen, G.-L.; Yu, R.-Q., DNAzyme-based biosensors and nanodevices. *Chemical Communications* **2015,** *51* (6), 979-995.

52. Zou, L.; Wu, Q.; Zhou, Y.; Gong, X.; Liu, X.; Wang, F., A DNAzyme-powered cross-catalytic circuit for amplified intracellular imaging. *Chemical Communications* **2019,** *55* (46), 6519-6522.

53. Liu, M.; Zhang, Q.; Chang, D.; Gu, J.; Brennan, J. D.; Li, Y., A DNAzyme feedback amplification strategy for biosensing. *Angewandte Chemie International Edition* **2017,** *56*

(22), 6142-6146.

54. Liu, M.; Yin, Q.; McConnell, E. M.; Chang, Y.; Brennan, J. D.; Li, Y., DNAzyme feedback amplification: relaying molecular recognition to exponential DNA amplification. *Chemistry–A European Journal* **2018,** *24* (18), 4473-4479.

55. Liu, X.; Zou, M.; Li, D.; Yuan, R.; Xiang, Y., Hairpin/DNA ring ternary probes for highly sensitive detection and selective discrimination of microRNA among family members. *Analytica Chimica Acta* **2019,** *1076*, 138-143.

56. Brown, A. K.; Li, J.; Pavot, C. M.-B.; Lu, Y., A lead-dependent DNAzyme with a two-step mechanism. *Biochemistry* **2003,** *42* (23), 7152-7161.

57. Khachigian, L. M., Deoxyribozymes as catalytic nanotherapeutic agents. *Cancer Research* **2019,** *79* (5), 879-888.

58. Santoro, S. W.; Joyce, G. F., Mechanism and utility of an RNA-cleaving DNA enzyme. *Biochemistry* **1998,** *37* (38), 13330-13342.

59. Santoro, S. W.; Joyce, G. F., A general purpose RNA-cleaving DNA enzyme. *Proceedings of the National Academy of Sciences* **1997,** *94* (9), 4262-4266.

60. Li, J.; Zheng, W.; Kwon, A. H.; Lu, Y., In vitro selection and characterization of a highly efficient Zn (II)-dependent RNA-cleaving deoxyribozyme. *Nucleic Acids Research* **2000,** *28* (2), 481-488.

61. Faulhammer, D.; Famulok, M., Characterization and divalent metal-ion dependence of in vitro selected deoxyribozymes which cleave DNA/RNA chimeric oligonucleotides. *Journal of Molecular Biology* **1997,** *269* (2), 188-202.

62. Peracchi, A., Preferential Activation of the 8–17 Deoxyribozyme by Ca 2+ Ions: Evidence for the Identity of 8–17 with the Catalytic Domain of the Mg5 Deoxyribozyme. *Journal of Biological Chemistry* **2000,** *275* (16), 11693-11697.

63. Cruz, R. P.; Withers, J. B.; Li, Y., Dinucleotide junction cleavage versatility of 8-17 deoxyribozyme. *Chemistry & Biology* **2004,** *11* (1), 57-67.

64. Schlosser, K.; Li, Y., Tracing sequence diversity change of RNA-cleaving deoxyribozymes under increasing selection pressure during in vitro selection. *Biochemistry* **2004,** *43* (30), 9695-9707.

65. Breaker, R. R.; Joyce, G. F., A DNA enzyme with Mg2+-dependent RNA phosphoesterase activity. *Chemistry & Biology* **1995,** *2* (10), 655-660.

66. Zhang, H.; Li, F.; Dever, B.; Li, X.-F.; Le, X. C., DNA-mediated homogeneous binding assays for nucleic acids and proteins. *Chemical Reviews* **2012,** *113* (4), 2812-2841.

67. Yamamoto, R.; Kumar, P. K., Molecular beacon aptamer fluoresces in the presence of Tat protein of HIV-1. *Genes to Cells* **2000,** *5* (5), 389-396.

68. Hamaguchi, N.; Ellington, A.; Stanton, M., Aptamer beacons for the direct detection of proteins. *Analytical Biochemistry* **2001,** *294* (2), 126-131.

69. Nutiu, R.; Li, Y., Structure-switching signaling aptamers. *Journal of the American Chemical Society* **2003,** *125* (16), 4771-4778.

70. Nutiu, R.; Li, Y., Structure-switching signaling aptamers: transducing molecular recognition into fluorescence signaling. *Chemistry-A European Journal* **2004,** *10* (8), 1868-1877.

71. He, J.-L.; Wu, Z.-S.; Zhang, S.-B.; Shen, G.-L.; Yu, R.-Q., Fluorescence aptasensor based on competitive-binding for human neutrophil elastase detection. *Talanta* **2010,** *80* (3), 1264-1268.

72. Fredriksson, S.; Gullberg, M.; Jarvius, J.; Olsson, C.; Pietras, K.; Gústafsdóttir, S. M.; Östman, A.; Landegren, U., Protein detection using proximity-dependent DNA ligation assays. *Nature Biotechnology* **2002,** *20* (5), 473.

73. Gullberg, M.; Gústafsdóttir, S. M.; Schallmeiner, E.; Jarvius, J.; Bjarnegård, M.; Betsholtz, C.; Landegren, U.; Fredriksson, S., Cytokine detection by antibody-based proximity ligation. *Proceedings of the National Academy of Sciences* **2004,** *101* (22), 8420-8424.

74. Zhang, H.; Li, X.-F.; Le, X. C., Binding-induced DNA assembly and its application to yoctomole detection of proteins. *Analytical Chemistry* **2011,** *84* (2), 877-884.

75. Li, F.; Zhang, H.; Lai, C.; Li, X. F.; Le, X. C., A Molecular Translator that Acts by Binding-Induced DNA Strand Displacement for a Homogeneous Protein Assay. *Angewandte Chemie International Edition* **2012,** *51* (37), 9317-9320.

76. Li, F.; Zhang, H.; Wang, Z.; Li, X.; Li, X.-F.; Le, X. C., Dynamic DNA assemblies mediated by binding-induced DNA strand displacement. *Journal of the American Chemical Society* **2013,** *135* (7), 2443-2446.

77. Zhang, H.; Li, F.; Dever, B.; Wang, C.; Li, X. F.; Le, X. C., Assembling DNA through affinity binding to achieve ultrasensitive protein detection. *Angewandte Chemie International Edition* **2013,** *52* (41), 10698-10705.

78. Zhang, H.; Lai, M.; Zuehlke, A.; Peng, H.; Li, X. F.; Le, X. C., Binding-induced DNA nanomachines triggered by proteins and nucleic acids. *Angewandte Chemie International Edition* **2015,** *54* (48), 14326-14330.

79. Tang, Y.; Wang, Z.; Yang, X.; Chen, J.; Liu, L.; Zhao, W.; Le, X. C.; Li, F., Constructing real-time, wash-free, and reiterative sensors for cell surface proteins using binding-induced dynamic DNA assembly. *Chemical Science* **2015,** *6* (10), 5729-5733.

80. Ren, K.; Wu, J.; Ju, H.; Yan, F., Target-driven triple-binder assembly of MNAzyme for amplified electrochemical immunosensing of protein biomarker. *Analytical Chemistry* **2015,** *87* (3), 1694-1700.

81. Wei, L.; Wang, X.; Wu, D.; Li, C.; Yin, Y.; Li, G., Proximity ligation-induced assembly of DNAzymes for simple and cost-effective colourimetric detection of proteins with high sensitivity. *Chemical Communications* **2016,** *52* (32), 5633-5636.

82. Zou, M.; Li, D.; Yuan, R.; Xiang, Y., Metal-ion dependent DNAzyme recycling amplification for sensitive and homogeneous immuno-proximity binding assay of α-fetoprotein biomarker. *Biosensors and Bioelectronics* **2017,** *92*, 624-629.

83. Li, J.; Wang, S.; Jiang, B.; Xiang, Y.; Yuan, R., Target-induced structure switching of aptamers facilitates strand displacement for DNAzyme recycling amplification detection of thrombin in human serum. *Analyst* **2019,** *144* (7), 2430-2435.

84. Huang, P.-J. J.; Liu, J., Two Pb 2+-specific dnazymes with opposite trends in split-site-dependent activity. *Chemical Communications* **2014,** *50* (34), 4442-4444.

85. Knott, G. J.; Doudna, J. A., CRISPR-Cas guides the future of genetic engineering.

Science **2018,** *361* (6405), 866-869.

86. Cong, L.; Ran, F. A.; Cox, D.; Lin, S.; Barretto, R.; Habib, N.; Hsu, P. D.; Wu, X.; Jiang, W.; Marraffini, L. A., Multiplex genome engineering using CRISPR/Cas systems. *Science* **2013,** *339* (6121), 819-823.

87. Mali, P.; Yang, L.; Esvelt, K. M.; Aach, J.; Guell, M.; DiCarlo, J. E.; Norville, J. E.; Church, G. M., RNA-guided human genome engineering via Cas9. *Science* **2013,** *339* (6121), 823-826.

88. Adli, M., The CRISPR tool kit for genome editing and beyond. *Nature Communications* **2018,** *9* (1), 1-13.

89. Lee, S. H.; Yu, J.; Hwang, G. H.; Kim, S.; Kim, H.; Ye, S.; Kim, K.; Park, J.; Park, D.; Cho, Y.-K., CUT-PCR: CRISPR-mediated, ultrasensitive detection of target DNA using PCR. *Oncogene* **2017,** *36* (49), 6823-6829.

90. Gu, W.; Crawford, E. D.; O'Donovan, B.; Wilson, M. R.; Chow, E. D.; Retallack, H.; DeRisi, J. L., Depletion of Abundant Sequences by Hybridization (DASH): using Cas9 to remove unwanted high-abundance species in sequencing libraries and molecular counting applications. *Genome Biology* **2016,** *17* (1), 1-13.

91. Myhrvold, C.; Freije, C. A.; Gootenberg, J. S.; Abudayyeh, O. O.; Metsky, H. C.; Durbin, A. F.; Kellner, M. J.; Tan, A. L.; Paul, L. M.; Parham, L. A., Field-deployable viral diagnostics using CRISPR-Cas13. *Science* **2018,** *360* (6387), 444-448.

92. Zhang, F.; Abudayyeh, O. O.; Gootenberg, J. S., A protocol for detection of COVID-19 using CRISPR diagnostics. **2020,** *8*.

93. Kailasa, S. K.; Mehta, V. N.; Koduru, J. R.; Basu, H.; Singhal, R. K.; Murthy, Z.; Park, T.-J., An overview of molecular biology and nanotechnology based analytical methods for the detection of SARS-CoV-2: promising biotools for the rapid diagnosis of COVID-19. *Analyst* **2021,** *146* (5), 1489-1513.

94. Ding, X.; Yin, K.; Li, Z.; Lalla, R. V.; Ballesteros, E.; Sfeir, M. M.; Liu, C., Ultrasensitive and visual detection of SARS-CoV-2 using all-in-one dual CRISPR-Cas12a assay. *Nature Communications* **2020,** *11* (1), 1-10.

95. Patchsung, M.; Jantarug, K.; Pattama, A.; Aphicho, K.; Suraritdechachai, S.; Meesawat, P.; Sappakhaw, K.; Leelahakorn, N.; Ruenkam, T.; Wongsatit, T., Clinical validation of a Cas13-based assay for the detection of SARS-CoV-2 RNA. *Nature Biomedical Engineering* **2020,** *4* (12), 1140-1149.

96. Moitra, P.; Alafeef, M.; Dighe, K.; Frieman, M. B.; Pan, D., Selective naked-eye detection of SARS-CoV-2 mediated by N gene targeted antisense oligonucleotide capped plasmonic nanoparticles. *ACS Nano* **2020,** *14* (6), 7617-7627.

97. Zhang, W. S.; Pan, J.; Li, F.; Zhu, M.; Xu, M.; Zhu, H.; Yu, Y.; Su, G., Reverse Transcription Recombinase Polymerase Amplification Coupled with CRISPR-Cas12a for Facile and Highly Sensitive Colorimetric SARS-CoV-2 Detection. *Analytical Chemistry* **2021,** *93* (8), 4126-4133.

98. Willner, I.; Shlyahovsky, B.; Zayats, M.; Willner, B., DNAzymes for sensing, nanobiotechnology and logic gate applications. *Chemical Society Reviews* **2008,** *37* (6), 1153-1165.

99. Okamoto, A.; Tanaka, K.; Saito, I., DNA logic gates. *Journal of the American Chemical Society* **2004,** *126* (30), 9458-9463.

100.   Seelig, G.; Soloveichik, D.; Zhang, D. Y.; Winfree, E., Enzyme-free nucleic acid logic circuits. *Science* **2006,** *314* (5805), 1585-1588.

101.   Frezza, B. M.; Cockroft, S. L.; Ghadiri, M. R., Modular multi-level circuits from immobilized DNA-based logic gates. *Journal of the American Chemical Society* **2007,** *129* (48), 14875-14879.

102.   Zhang, C.; Yang, J.; Jiang, S.; Liu, Y.; Yan, H., DNAzyme-based logic gate-mediated DNA self-assembly. *Nano Letters* **2015,** *16* (1), 736-741.

103.   Bi, S.; Yan, Y.; Hao, S.; Zhang, S., Colorimetric logic gates based on supramolecular DNAzyme structures. *Angewandte Chemie International Edition* **2010,** *49* (26), 4438-4442.

104.   Wang, F.; Elbaz, J.; Orbach, R.; Magen, N.; Willner, I., Amplified analysis of DNA by the autonomous assembly of polymers consisting of DNAzyme wires. *Journal of the American Chemical Society* **2011,** *133* (43), 17149-17151.

105.   Tian, Y.; He, Y.; Chen, Y.; Yin, P.; Mao, C., A DNAzyme that walks processively and autonomously along a one-dimensional track. *Angewandte Chemie International Edition* **2005,** *44* (28), 4355-4358.

106.   Peng, H.; Li, X.-F.; Zhang, H.; Le, X. C., A microRNA-initiated DNAzyme motor operating in living cells. *Nature Communications* **2017,** *8*, 14378.

107.   Liu, J.; Cui, M.; Zhou, H.; Yang, W., DNAzyme based nanomachine for in situ

detection of microRNA in living cells. *ACS Sensors* **2017,** *2* (12), 1847-1853.

108.   Bharti, A. R.; Patra, K. P.; Chuquiyauri, R.; Kosek, M.; Gilman, R. H.; Llanos-Cuentas, A.; Vinetz, J. M., Polymerase chain reaction detection of Plasmodium vivax and Plasmodium falciparum DNA from stored serum samples: implications for retrospective diagnosis of malaria. *The American Journal of Tropical Medicine and Hygiene* **2007,** *77* (3), 444-446.

109.   Paraskevis, D.; Beloukas, A.; Haida, C.; Katsoulidou, A.; Moschidis, Z.; Hatzitheodorou, H.; Varaklioti, A.; Sypsa, V.; Hatzakis, A., Development of a new ultra sensitive real-time PCR assay (ultra sensitive RTQ-PCR) for the quantification of HBV-DNA. *Virology Journal* **2010,** *7* (1), 1-6.

110. Sassolas, A.; Blum, L. J.; Leca-Bouvier, B. D., Homogeneous assays using aptamers. *Analyst* **2011,** *136* (2), 257-274.